

# **Transcriptional Regulation in Podocytes**

Inaugural-Dissertation

zur

Erlangung des Doktorgrades

der Mathematisch-Naturwissenschaftlichen Fakultät

der Universität zu Köln

vorgelegt von

Mahdieh Rahmatollahi

aus Teheran (Iran)

Köln

2020

Berichtersteller: Prof. Dr. Thomas Benzing  
(Gutachter) Prof. Dr. Andreas Beyer

Tag der mündlichen Prüfung: 13.05.2020

# Table of Contents

Table of Contents .....	iii
Figures directory.....	vi
Table directory .....	viii
Abbreviations and Acronyms .....	ix
1 Abstract .....	1
2 Zusammenfassung.....	3
3 Introduction .....	5
3.1 Chronic kidney disease .....	5
3.2 Transcriptional regulation .....	10
3.3 The podocyte transcription factor repertoire .....	13
3.4 Transcriptomic analysis in kidneys .....	14
4 Aims of thesis .....	16
5 Materials and Methods.....	18
5.1 Materials.....	18
5.1.1 Chemicals.....	18
6 Kits and assays.....	21
6.1.1 Buffers and solutions.....	22
6.1.2 Oligonucleotides.....	26
6.1.3 Antibodies and enzymes .....	28
6.1.4 Equipment .....	29
6.1.5 Software .....	32
6.2 Methods .....	33
6.2.1 Cell culture.....	33
6.2.2 CRISPR/Cas9-mediated genome editing .....	34
6.2.3 Mouse experiments.....	37
6.2.4 Bioinformatics analysis.....	44
7 Results .....	48
7.1 Part one: <i>Wt1</i> .....	48
7.1.1 Haploinsufficiency of <i>Wt1</i> triggers no defect in the kidney development. ....	48

7.1.2	Heterozygous deletion of <i>Wt1</i> leads to development of FSGS.....	50
7.1.3	Distinct analysis modalities offer exquisite information by focusing on “Early FSGS”, “Late FSGS”, “FSGS progression” and “glomerular maturation and aging” . .....	51
7.1.4	Haploinsufficiency of <i>Wt1</i> leads to differential regulation of genes and or pathways in podocytes.....	54
7.1.5	Differential binding of <i>Wt1</i> on the regulatory regions suggests transcriptional reprogramming at early disease stage. ....	58
7.1.6	Integrative analysis of binding and expression .....	61
7.1.7	Collagen biology is disturbed as FSGS develops.....	64
7.1.8	Ephrin signaling pathway is progressively impaired in the course of FSGS. ....	67
7.2	Part two: <i>Tead1</i> .....	73
7.2.1	In wildtype mouse glomeruli, <i>Tead1</i> is the effector of Hippo signaling pathway. ....	73
7.2.2	Chromatin immunoprecipitation of <i>Tead1</i> in isolated mouse glomeruli introduced technical hurdles.....	74
7.2.3	Quality check for <i>Tead1</i> ChIPseq verifies robustness of the dataset.....	77
7.2.4	In podocytes, <i>Tead1</i> predominantly regulates genes involved in cell-adhesion and actin cytoskeleton regulatory pathways.....	79
7.2.5	Cooperation of <i>Tead1</i> and <i>Wt1</i> in gene regulation by co-binding at key podocyte target genes. ....	81
7.3	Part three: Single-cell RNA sequencing of isolated mouse glomeruli.....	84
7.3.1	Single-cell RNA-sequencing identifies the relevant cell populations in purified glomeruli .....	84
7.3.2	Single-cell transcriptomics reveal novel molecular markers specific to glomerular cell types. ....	87
7.3.3	Sub-clustering reveals the presence of endothelial subpopulations.....	89
7.3.4	Sub-clustering reveals a limited heterogeneity of podocytes. ....	92
8	Discussion.....	96
8.1	<i>Wt1</i> reprograms podocytes in the face of damage. ....	96
8.2	Collagen Biology is one of the main functional targets of <i>Wt1</i> during the development of FSGS.....	97
8.3	Ephrin Signaling pathway is a novel target of <i>Wt1</i> during podocyte damage.....	98
8.4	<i>Tead1</i> exerts the Hippo pathway-mediated gene regulation in podocytes. ....	99
8.5	The puzzle of gene regulation in podocytes.....	100



8.6	Concluding remarks .....	101
9	Bibliography .....	103
10	Publications .....	113
10.1	Publication in academic journals.....	113
10.2	Publication in international academic conferences .....	113
11	Acknowledgment .....	114
12	Erklärung .....	116
	Teilpublikationen: .....	116
13	Curriculum Vitae.....	117

## Figures directory

Figure 3.1: Electron microscopy image of normal rat glomerular capillaries.....	5
Figure 3.2: Transmission electron microscopy of human filtration barrier.....	6
Figure 3.3: Histology images of the kidney sections showing normal vs. sclerosed glomeruli.	7
Figure 3.4: Controlling chromatin accessibility and transcription is governed by several factors. .....	10
Figure 3.5: Overview of <i>cis</i> - and <i>trans</i> -regulatory elements.....	11
Figure 3.6: Human disease phenotypes caused by TF dysregulation.....	12
Figure 3.7: Wt1-dependent transcriptional network in podocyte.....	13
Figure 7.1: Heterozygous deletion of Wt1 does not impose any developmental defect in mouse kidneys.....	49
Figure 7.2: <i>Wt1</i> <sup>het del</sup> mice develops proteinuria and FSGS.....	51
Figure 7.3: RNAseq analysis of the isolated mouse glomeruli from <i>Wt1</i> <sup>het del</sup> and wildtype mice at age 4 and 12 weeks.....	53
Figure 7.4: Principal component analysis (PCA) and differential expression (DE) analysis of RNAseq data.....	55
Figure 7.5: Functional annotation of DEGs at early and late FSGS.....	56
Figure 7.6: Results of the Signaling Pathway Impact Analysis (SPIA) of DEGs at early and late FSGS using KEGG and REACTOME databases.....	57
Figure 7.7: Wt1ChIPseq at non-sclerotic stage of FSGS (4 weeks) compared to the wildtype mice.....	59
Figure 7.8: Differential binding analysis if Wt1-bound loci in <i>Wt1</i> <sup>het del</sup> and control mice at 4 weeks.....	60
Figure 7.9: Volcano plot representing the targets of Wt1 differential binding (orange) and Wt1 binding in control condition (dark green) at early and late FSGS.....	61
Figure 7.10: LFC-density plot of differentially bound genes for early and late FSGS.....	62
Figure 7.11: Integration of RNAseq and ChIPseq highlights key GO annotations contributing to the early and late FSGS.....	63
Figure 7.12: Heatmap depicts the expression values of collagen subtypes in <i>Wt1</i> <sup>het del</sup> and control mice at 4 and 12 weeks.....	64
Figure 7.13: Chord plot for Collagen Biology.....	65
Figure 7.14: Immunofluorescence staining of GBM components and evaluation of GBM thickness.....	66

Figure 7.15: DEGs contributing to Ephrin Signaling and podocyte-specific expression values of the Ephs and Ephrins.....	68
Figure 7.16: Assessment of EphrinB1 and EphB1 protein expression in late FSGS. ....	70
Figure 7.17: EphrinB1 progressively reduces in the course of FSGS.....	72
Figure 7.18: RNA and protein expression of TEAD family members in podocytes.....	73
Figure 7.19: Recombination target locus in the exon 2 of the mouse Tead1.....	74
Figure 7.20: T7 endonuclease assay shows successful recombination of the sequence of interest. ....	75
Figure 7.21: Alignment of the sequence reads from the founder FLAG-Tead1 mouse with the designed recombinant Tead1.....	75
Figure 7.22: Addition of the bridging antibody significantly increases the Tead1 chromatin immunoprecipitation. ....	76
Figure 7.23: Three replicates of Tead1ChIP-seq show decent quality.....	77
Figure 7.24: Tead1ChIPseq quality evaluation. ....	78
Figure 7.25: Enhancer-based regulation of actin cytoskeleton and cell adhesion in podocytes by Tead1. ....	80
Figure 7.26: Tead1 and Wt1 co-binding assessment. ....	81
Figure 7.27: Genome browser plots showing Tead1 and Wt1 ChIPseq signals and exon/intron structure of target genes.....	82
Figure 7.28: Functional annotation analysis of Tead1 and Wt1 co-binding on gene regulatory regions.....	83
Figure 7.29: Single-cell RNA sequencing of isolated mouse glomeruli.....	84
Figure 7.30: Single-cell RNA-sequencing of the purified mouse glomeruli identifies five known cell populations. ....	86
Figure 7.31: Comparison of single cell RNAseq data with bulk mRNAseq.....	87
Figure 7.32: Identification of novel markers for three main glomerular cell types.....	88
Figure 7.33: Subclustering of glomerular endothelium. ....	90
Figure 7.34: Endothelial subclusters are responsible for various cellular functions. ....	91
Figure 7.35: Subclustering of glomerular podocytes. ....	93
Figure 7.36: Laser scanning confocal microscopy of Lars2 staining in double-fluorescent reporter mice. ....	94
Figure 7.37: Laser scanning confocal microscopy of Cald1 staining in double-fluorescent reporter mice. ....	95

## Table directory

Table 3-1: Genetic causes of FSGS and/or nephrotic syndrome.....	8
Table 5-1: List of chemicals, reagents and solutions .....	18
Table 6-1: List of kits and assays .....	21
Table 6-2: List of buffers and solutions .....	22
Table 6-3: List of oligonucleotide sequences .....	26
Table 6-4: List of antibodies and enzymes .....	28
Table 6-5: List of equipment .....	29
Table 6-6: List of software .....	32
Table 6-7: List of cell lines .....	33
Table 6-8: List of designed guide RNA.....	34
Table 6-9: Hybridization reaction reagents and cycling conditions .....	35
Table 6-10: PCR reaction reagents and cycling conditions .....	35
Table 6-11: List of designed ssODN .....	36
Table 6-12: Genotyping PCR reaction reagents .....	37
Table 6-13: List of PCR cycling conditions and the product sizes .....	39

## Abbreviations and Acronyms

5hmC	5-hydroxymethylcytosine
ACR	Albumin to creatinine ratio
bp	base pairs
BP	Biological process
BSA	Bovine serum albumin
Cas9	CRISPR associated protein 9
CC	Cellular component
Cdc42	Cell division control protein 42 homolog
ChIPseq	Chromatin immunoprecipitation
CRE	<i>Cis</i> -regulatory elements
CRISPR	Clustered regularly interspaced short palindromic repeats
DAPI	4',6-diamidino-2-phenylindole
DB	Differentially bound
DBD	DNA binding domain
ddH <sub>2</sub> O	Double distilled water
DEG	Differentially expressed gene
DGE	Digital gene expression
DMEM	Dulbecco's modified eagle's medium
DNA	Deoxyribonucleic acid
dNTP	Deoxyribonucleotide triphosphate
DTT	Dithiothreitol
EC	Endothelial cell
EDTA	Ethylenediaminetetraacetic acid
EM	Electron microscopy

eQTL	Expression quantitative trait loci
FBS	Fetal bovine serum
FDR	False discovery rate
fp	Forward primer
FSGS	Focal segmental glomerulosclerosis
GBM	Glomerular basement membrane
GBP	Genome browser plot
GFP	Green fluorescent protein
GFR	Glomerular filtration rate
GO	Gene ontology
GWAS	Genome-wide association study
h	Hours
H <sub>2</sub> O	Water
HBSS	Hank's buffered salt solution
HDAC	Histone deacetylase
HDR	Homology directed repair
Het del	Heterozygous deletion
IDR	Irreproducible discovery rate
IF	Immunofluorescent staining
JNK	c-Jun N-terminal kinase
l	Liter
LANUV NRW	Landesamt für Natur, Umwelt und Verbraucherschutz Nordrhein-Westfalen
LFC	Logarithmic fold change
MF	Molecular function
mg	Milligram

mIMCD3	Mouse inner medullary collecting duct cell line
min	Minutes
ml	Milliliter
mM	Millimolar
NaCl	Sodium chloride
NDS	Normal donkey serum
NLS	nuclear localization signal or sequence
nM	Nanomolar
<i>p</i> Value	Probability
PAM	Protospacer adjacent motif
PAS	Periodic acidic Schiff
PBS	Phosphate-buffered saline
PCA	Principal component analysis
PCR	Polymerase chain reaction
PFA	Paraformaldehyde
pM	Picomolar
Rac1	Ras-related C3 botulinum toxin substrate 1
RhoA	Ras homolog family member A
RIN	RNA Integrity number
RNA	Ribonucleic acid
RNA Pol II	RNA Polymerase II
rp	Reverse primer
s	Seconds
scRNAseq	Single cell RNA sequencing
SDS	Sodium dodecyl sulfate

sgRNA	Small guide RNA
ssODN	Single-stranded oligonucleotide donor
STED	Stimulated emission depletion
TF	Transcriptional factor
tg	Transgenic
Tm	Melting temperature
TPM	Transcripts per kilobase million
Tris	Tris(hydroxymethyl)aminomethane
tSNE	t-distributed stochastic neighbor embedding
TSS	Transcription start site
UMI	Unique molecular identifier
Wt1	Wilm's tumor suppressor 1 protein
$\mu$ l	Microliter
$\mu$ M	Micromolar



# 1 Abstract

Prolonged and progressive podocyte injury leads to extensive proteinuria, scarred glomeruli and a decline in renal function. When left untreated, it develops chronic kidney disease (CKD) which often has poor prognosis. Disturbed gene regulation serves as both cause and/or consequence in the context of podocyte injury. Unravelling the gene regulatory circuits within podocytes is therefore a key step to introduce new curative and or palliative strategies for chronic kidney disease.

Wt1 is a master transcription factor (TF) in podocytes and previous work has determined Wt1-dependent gene regulatory networks in healthy adult podocytes. In this thesis, analysis of Wt1-directed gene regulation in a genetic mouse model of podocyte damage demonstrated that Wt1 executes a differential binding tactic on genomic elements during early phases of podocyte damage. This differential binding on the genome is reflected as differential pathway regulation in the course of podocyte injury. Key podocyte pathways such as collagen biosynthesis, collagen metabolism as well as Eph/Ephrin signaling are markedly compromised. Perturbation of these critical functions entails glomerular basement membrane thickening, collapse of foot processes and podocyte detachment from the basement membrane.

Next, a genome-wide analysis of Tead1, another master transcription factor in podocytes, indicated the cooperative function of Wt1 and Tead1 on gene regulatory elements. Both Wt1 and Tead1 are members of the podocyte-specific transcription factor network which regulates homeostasis and cell survival in podocytes. Interestingly, analysis of Tead1-dependent functions showed that Tead1 mainly regulates actin cytoskeleton dynamics and cell adhesion in podocytes. Tead1-dependent functions are chiefly directed via distal regulatory elements. Previously, enhancer-based gene regulation by Wt1 has been shown in podocytes. In line with this, examining the peak distribution of both Wt1 and Tead1 across the genome accentuates the high-impact role of enhancers in gene regulation in podocytes. Next, *De novo* motif enrichment analysis and motif conservation scores around the Tead1 peaks revealed enrichment not only for Tead1 motif but also for Wt1 and other partners of podocyte-specific TF network. Co-binding analysis of the Tead1 ChIPseq with our previous Wt1 ChIPseq dataset suggested that some of the Tead1-dependent functions are co-directed by Wt1 and vice versa.

Finally, another set of complementary analysis was done in this thesis which unveils a different aspect of gene regulation in podocytes. Here, a highly parallel transcriptional profiling of more than 13,000 cells obtained from isolated mouse glomeruli was performed which identified the three main glomerular cell types *i.e.* podocytes, endothelial cells and mesangial cells. The comprehensive gene expression profile of all identified cell types is gathered in an interactive online atlas which can be queried based on gene names. In addition, novel markers for podocytes, endothelial cells and mesangial cells were introduced and validated by cross-referencing with glomerular expression of such markers in Human Protein Atlas. Furthermore, cell heterogeneity assessment for podocytes and endothelial cells was done. Endothelial cells

showed four subpopulations relevant to different phases of their activation and proliferation. Podocytes, however, exhibited a more subtle trace for cellular heterogeneity. Thus, a new immunofluorescent staining approach was adopted to address the identified podocyte subpopulations. The results validated identification of subpopulations within podocytes based on the differential immunofluorescence signal for subpopulation markers observed in different podocytes within a glomerulus.

Altogether, the novel findings throughout this thesis casts some light on tens of thousands of questions surrounding gene regulation in podocytes.

## 2 Zusammenfassung

Anhaltende und progressive Podozytenschäden können zu einer ausgedehnten Proteinurie, vernarbten Glomeruli sowie einer Abnahme der Nierenfunktion führen. Unbehandelt kann dies zu einer chronischen Nierenerkrankung (CKD) führen, welche sich oft durch eine schlechte Prognose auszeichnet. Eine gestörte Genregulation ist sowohl Ursache wie auch gleichzeitig Folge einer Podozytenschädigung. Die Entschlüsselung der Genregulationskreisläufe innerhalb der Podozyten ist daher ein wichtiger Schritt, um neue heilende oder zumindest lindernde Strategien für chronische Nierenerkrankungen zu entwickeln.

Wt1 ist ein Master-Transkriptionsfaktor (TF) in Podozyten und in früheren Arbeiten konnten bereits Wt1-abhängige genregulatorische Netzwerke in gesunden adulten Podozyten nachgewiesen werden. In dieser Arbeit konnte durch die Analyse der Wt1-gesteuerten Genregulation in einem genetischen Mausmodell der Podozytenschädigung gezeigt werden, dass WT1 eine unterschiedliche Bindungstaktik an genomischen Elementen in frühen Phasen der Podozytenschäden aufweist. Diese differenzielle Bindung am Genom spiegelt sich als differentielle Regulierung des Signalweges im Laufe der Podozytenschädigung wider. Wichtige podozytäre Signalwege wie die Biosynthese von Kollagen, der Metabolismus von Kollagen sowie die Eph/Ephrin-Signalgebung sind merklich beeinträchtigt. Die Störung dieser kritischen Funktionen führt zu einer Verdickung der glomerulären Basalmembran, dem Kollaps der Fußfortsätze sowie dem Ablösen der Podozyten von der Basalmembran.

Außerdem zeigte eine genomweite Analyse von Tead1, einem weiteren Master-Transkriptionsfaktor innerhalb von Podozyten, die zusammenwirkende Funktion zwischen Wt1 und Tead1 auf genregulatorischen Elementen. Sowohl Wt1 als auch Tead1 sind Mitglieder des podozytenspezifischen Transkriptionsfaktor-Netzwerkes, welches die Homöostase und das Zellüberleben in Podozyten reguliert. Interessanterweise zeigte die Analyse der Tead1-abhängigen zellulären Funktionen, dass Tead1 hauptsächlich die Dynamik des Aktinzytoskelettes sowie die Zelladhäsion in Podozyten reguliert. Die Tead1-abhängigen Funktionen werden hauptsächlich über distale regulatorische Elemente gesteuert. Bisher konnte eine Enhancer-basierte Genregulation von Wt1 in Podozyten gezeigt werden. In diesem Zusammenhang unterstreicht die Untersuchung der peak distribution von Wt1 und Tead1 im Genom die essentielle Rolle von Enhancern in der Genregulation in von Podozyten. Zusätzlich zeigte die De novo-motif enrichment analysis sowie der motif conservation scores um die Tead1-Peaks herum eine Anreicherung für nicht nur das Tead1-Motiv, sondern auch für Wt1 und andere Partner des podozytspezifischen TF-Netzwerkes. Die Co-Bindungs-Analyse von Tead1 ChIPseq mit unserem vorherigen Wt1 ChIPseq-Datensatz deutete darauf hin, dass einige der Tead1-abhängigen Funktionen von Wt1 mitgesteuert werden und umgekehrt.

Schließlich wurde in dieser Arbeit eine Reihe von komplementären Analysen durchgeführt, welche einen anderen Aspekt der Genregulation in Podozyten enthüllten. Dafür wurde eine hochparallele Transkriptionsprofilierung von mehr als 13.000 Zellen aus isolierten Maus-Glomeruli durchgeführt, welche die drei wichtigsten glomerulären Zelltypen, d.h. Podozyten,

Endothelzellen und Mesangialzellen, identifizierte. Das umfangreiche Genexpressionsprofil von allen identifizierten Zelltypen wurde in einem interaktiven Online-Atlas zusammengestellt, in welchem nach einzelnen Gennamen gesucht werden kann. Zusätzlich wurden neue Marker für Podozyten, Endothelzellen und Mesangialzellen eingeführt und durch Querverweise mit der glomerulären Expression solcher Marker im humanen Protein-Atlas validiert. Außerdem wurde die Zellheterogenität von Podozyten und Endothelzellen untersucht. Endothelzellen zeigten dabei vier Subpopulationen, welche für unterschiedliche Phasen ihrer Aktivierung und Proliferationen relevant sind.

Demgegenüber wiesen Podozyten lediglich eine schwache Ausprägung für zelluläre Heterogenität auf. Aus diesem Grund wurde eine neue Immunfluoreszenzfärbung entwickelt, um die identifizierten Subpopulationen der Podozyten zu markieren. Die dadurch gewonnenen Ergebnisse validierten die Identifizierung von Subpopulationen innerhalb von Podozyten auf der Basis des unterschiedlichen Immunfluoreszenzsignals für Subpopulationsmarker, welche in verschiedenen Podozyten innerhalb eines Glomerulus beobachtet wurden.

Zusammengefasst können die neuen Erkenntnisse, die in dieser Arbeit erzielt wurden, dazu beitragen, bei der Beantwortung einer Vielzahl von Fragestellungen rund um die Genregulation in Podozyten zu helfen.

## 3 Introduction

### 3.1 Chronic kidney disease

More than 10% of the world's population are suffering from CKD. (Levin et al., 2017) With an estimated prevalence of 13.4% in 2016, CKD imposes a significant burden to healthcare systems worldwide. (Hill et al., 2016) Among the etiologies for CKD, 90% stems from glomerular diseases in which podocytes are damaged and lost. (Wiggins, 2007)

Podocytes are terminally differentiated visceral epithelial cells which are the key components of establishing the selective permeability in the glomerulus. They consist of a cell body and cytoplasmic projections known as foot processes (FP). (Mundel and Kriz, 1995; Pavenstädt et al., 2003) Microtubules, intermediate filaments and actin cytoskeleton are the main structural and functional components of foot processes. (Andrews, 1981) In glomerulus, the interdigitated foot processes of adjacent podocytes are connected via special cell-cell contacts known as slit diaphragm (SD). (Fukasawa et al., 2009; Reiser et al., 2000) (Figure 3.1)

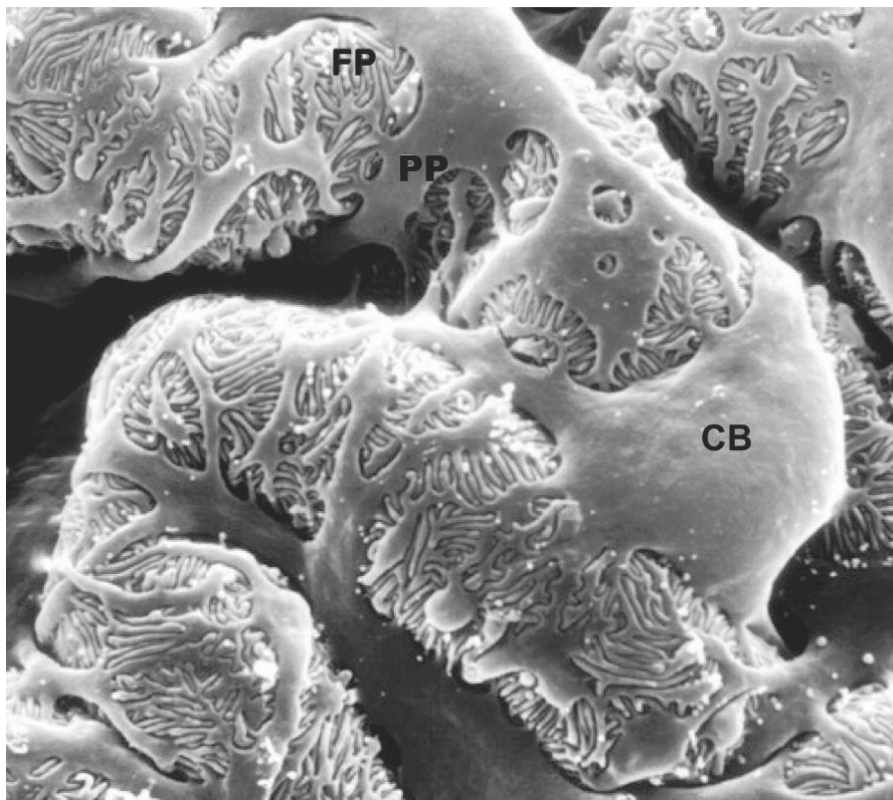


Figure 3.1: Electron microscopy image of normal rat glomerular capillaries.

The capillary tuft is covered by the interdigitated foot processes of podocytes. CB: cell body, PP: primary processes, FP: foot processes; magnification  $\times \sim 6,000$ . Adopted from (Pavenstädt et al., 2003)

The interdigitated foot processes, their underlying basement membrane known as the glomerular basement membrane (GBM) and the fenestrated endothelium establish the filtration barrier in the glomerulus. This exquisite structure and the negatively charged molecules within this barrier restrict the passage of proteins and guarantee a protein-free urine. When podocytes are damaged, the podocyte cytoskeleton undergoes massive dysregulation. The slit diaphragm becomes disintegrated and the foot processes collapse on their underlying GBM, a phenomenon known as effacement. (Figure 3.2) As a result, proteins leak into the primary urine filtrate. When this condition is persistent, excessive extracellular matrix deposition occurs leading to a thickened GBM; podocytes detach from the basement membrane and the sclerotic lesions develop. (Brinkkoetter et al., 2013; Haraldsson et al., 2008; Perico et al., 2016; Yu et al., 2018)

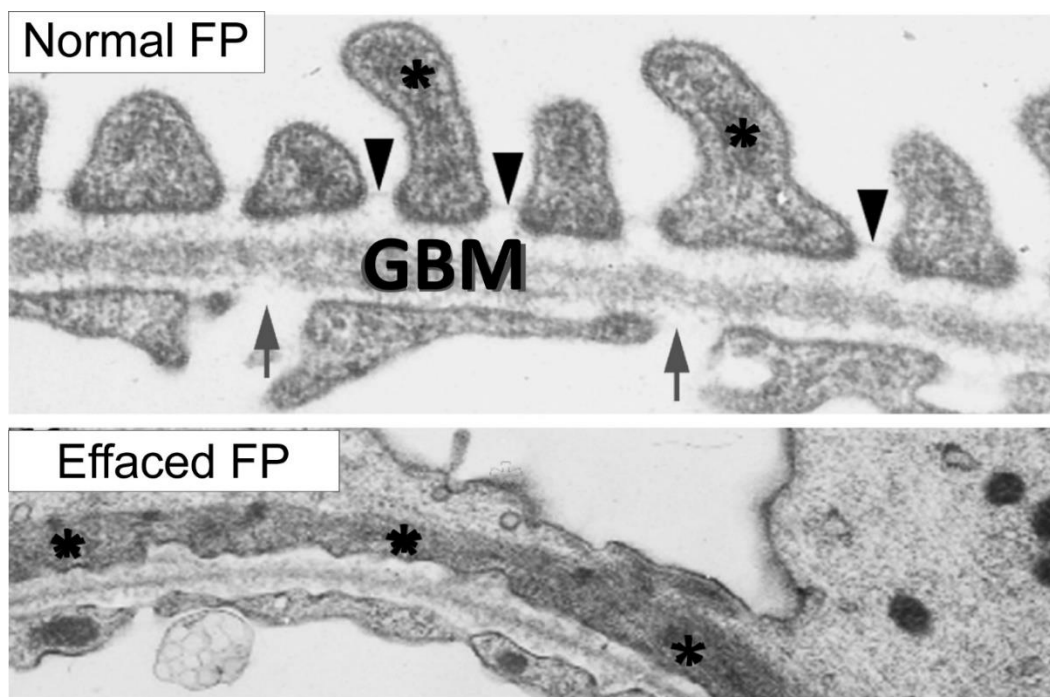


Figure 3.2: Transmission electron microscopy of human filtration barrier.

Fenestrated endothelium is indicated by arrows. SD is indicated by arrowheads. Asterisks show actin filaments in FP. During effacement, abnormal FP architecture and flattened actin filaments are visible. Figure adopted and modified from (Mathieson, 2010)

This chain of events is a histological phenomenon termed as Focal Segmental Glomerulosclerosis (FSGS) which is caused by primary (idiopathic) or secondary podocyte injury. FSGS refers to the partial scarring (segmental) of some but not all (focal) glomeruli in the kidney and it is a frequent pathological event in CKD. (Peev et al., 2017) (Figure 3.3)

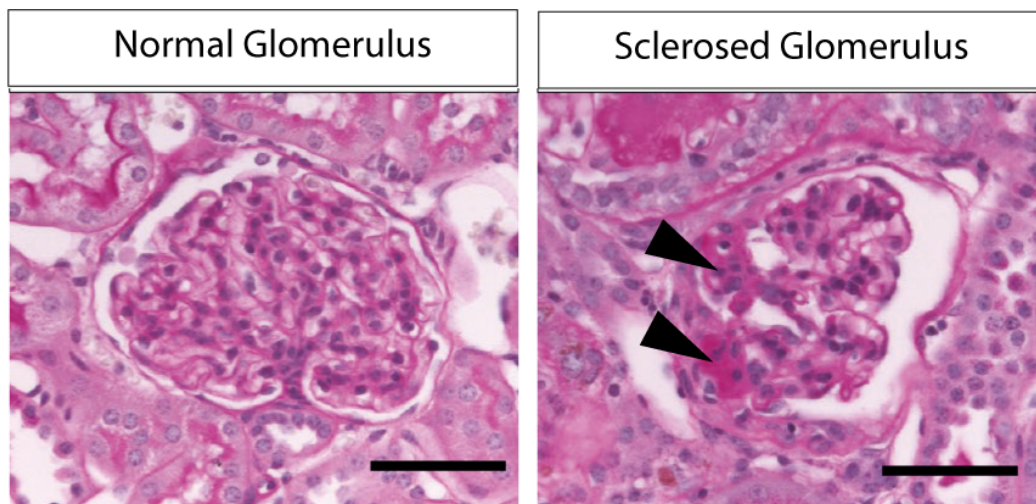


Figure 3.3: Histology images of the kidney sections showing normal vs. sclerosed glomeruli.

Periodic acidic Schiff (PAS) staining of kidneys from adult male FVB/N mouse (normal) and adult male *Wt1<sup>het del</sup>* mouse (FSGS mouse model). Arrowheads show sclerotic lesions. Scale bar: 20  $\mu$ m

During the progression of FSGS, the remaining functional glomeruli are posed by increased blood shear stress which can accelerate podocyte damage. When left untreated, FSGS can eventually result in kidney failure. (Rosenberg and Kopp, 2017) There are numbers of medications frequently used to control the symptoms. According to the Kidney Disease International Guideline Organization, prolonged steroids should be considered as the first-line therapy for patients suffering from FSGS. Intolerant patients, however, should receive Calcineurin inhibitors (CNIs). (Beck et al., 2013) Despite all the beneficial effects of both therapy lines on the remission of symptoms, neither of the approaches are curative and safe. (Lafayette, 2019) The window for podocyte salvage to prevent disease progression in FSGS is very narrow and the missing novel therapeutic approaches depend on further longitudinal investigations into the mechanism of podocyte damage in its early stage.

In recent years, the genetic factors contributing to the development of FSGS have caught increasing attention. Hereditary FSGS has been attributed to mutations in genes encoding for the important podocyte molecules. (Fogo, 2015; Wang et al., 2019) Table 3-1 enlists some but not all gene mutations resulting in hereditary FSGS. Although all these genes are crucial for the maintenance of podocyte homeostasis, some of them have a more central role in coordinating biological processes within the podocytes. Transcription factors are one of the major categories of such key genes. Thus, investigation of their functions under podocyte health and damage conditions can answer handfuls of questions in the context of FSGS.

Table 3-1: Genetic causes of FSGS and/or nephrotic syndrome.

<b>Gene</b>	<b>Protein</b>	<b>Function</b>	<b>Phenotype</b>
NPHS1	Nephrin	Podocyte slit diaphragm	Congenital nephrotic syndrome Finnish type, sporadic FSGS or nephrotic syndrome
CD2AP	CD2-associated protein	Podocyte slit diaphragm	Autosomal-dominant or autosomal-recessive sporadic adult-onset FSGS
NPHS2	Podocin	Podocyte slit diaphragm	Early onset autosomal-recessive FSGS
ACTN4	$\alpha$ -actinin-4	Podocyte cytoskeleton	Adult onset autosomal-dominant FSGS
MYO1E	Unconventional myosin 1E	Actin function	Early onset autosomal-recessive FSGS
INF2	Inverted formin-2	Actin regulation	Adult onset FSGS
PTPRO	Receptor-type tyrosine-protein phosphatase 0*	Podocyte signalling	Autosomal-recessive childhood FSGS
ARHGDI1	Rho GDP-dissociation inhibitor 1	Rho GTPase signalling, actin dynamics	Early onset nephrotic syndrome or FSGS
TRPC6	Transient receptor potential channel 6	Calcium channel, podocyte mechanosensing	Autosomal-dominant or autosomal-recessive sporadic adult onset FSGS
WT1	Wilms tumour protein	Podocyte development	Autosomal-dominant sporadic FSGS, diffuse mesangial sclerosis
PLCE1	Phospholipase C $\epsilon$ 1	Podocyte differentiation, signalling	Early onset autosomal-recessive FSGS or diffuse mesangial sclerosis
LMX1B	LIM homeobox transcription factor 1- $\beta$	Podocyte and GBM development	Nail-patella syndrome, rare FSGS
CD151	CD151 antigen	Podocyte and GBM, laminin-integrin interactions	Early FSGS, deafness, $\beta$ -thalassaemia
LAMB2	Laminin B2 chain	Interacts with integrin $\alpha$ 3 $\beta$ 1, links GBM to actin cytoskeleton	Autosomal-recessive Pierson syndrome or FSGS
ITGB4	Integrin $\beta$ 4	Cell-matrix adhesion	Rare FSGS
SMARCAL1	SWI/SNF-related matrix-associated actin-dependent regulator of chromatin subfamily A-like protein 1	Chromatin bundling and gene transcription	Autosomal-recessive Schimke immunoosseous dysplasia, childhood FSGS



COQ2	Polyprenyltransferase	Mitochondrial function, deficient Coenzyme Q10	Autosomal-recessive early onset nephrotic syndrome or FSGS
COQ6	Ubiquinone biosynthesis monooxygenase COQ6	Ubiquinone biosynthesis	Autosomal-recessive nephrotic syndrome, FSGS, deafness
PDSS2	Decaprenyl diphosphate synthase subunit 2	Coenzyme Q10 synthesis, mitochondrial function	FSGS or collapsing FSGS
ADCK4	AarF domain-containing protein kinase 4	Coenzyme Q10 modulation	FSGS
MTTL1	Mitochondrially encoded tRNA leucine 1	Mitochondrial tRNA	Autosomal recessive MELAS or FSGS
SCARB2	Scavenger receptor class B member 2	Putative lysosomal receptor	FSGS or collapsing FSGS
APOL1	Apolipoprotein L1	Function unknown	Risk of FSGS, collapsing FSGS or HIVAN

Adopted from (Fogo, 2015)

## 3.2 Transcriptional regulation

The genome is a dynamic gamut of 3-D chromatin ranging from accessible to inaccessible states. (Shema et al., 2019) Chromatin accessibility is defined by the interplay between different chromatin and histone modifications in one hand and transcription factor (TF) binding on the other. (Figure 3.4) (Mason and Vondriska, 2019; Soufi et al., 2015)

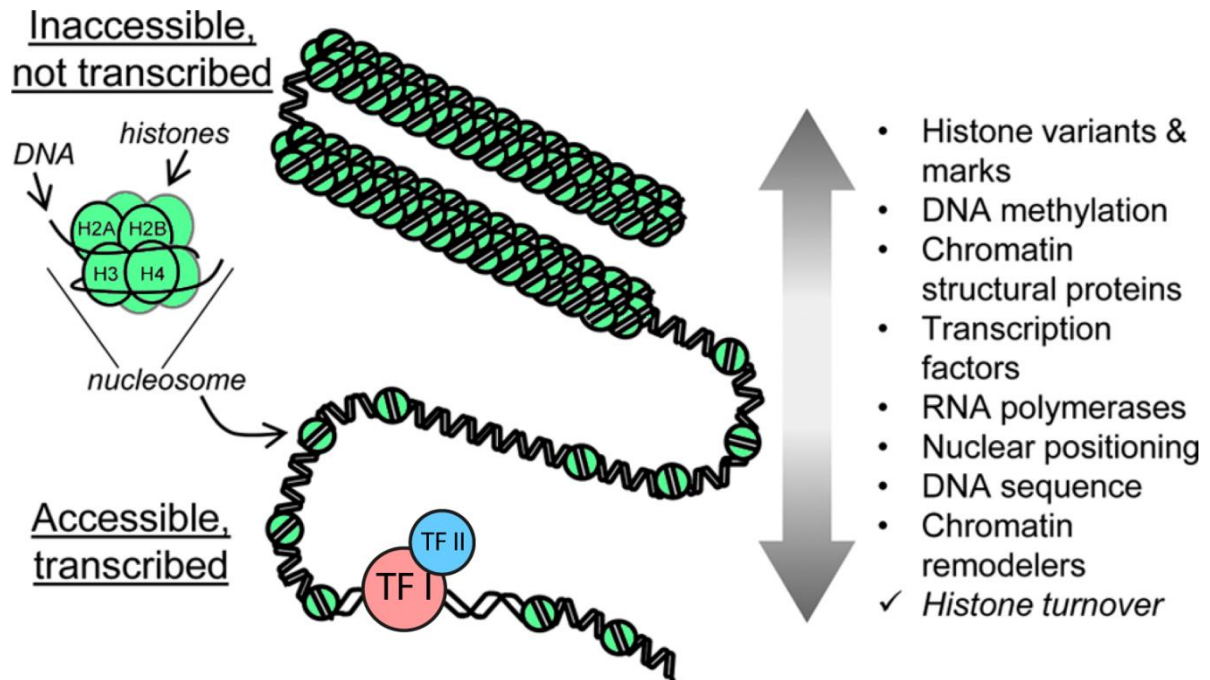


Figure 3.4: Controlling chromatin accessibility and transcription is governed by several factors.

Nucleosomes are structural units of chromatin comprised of different histone subtypes (octamer complex including one pair of: H2A, H2B, H3 and H4). Different chromatin and histone modifications can mobilize the nucleosome and shuffle the chromatin between inaccessible (heterochromatin) and accessible (euchromatin) states. TF: transcription factor. Figure adopted and modified from (Mason and Vondriska, 2019)

In eukaryotes, gene expression is the outcome of combinatorial function of *cis*- and *trans*-acting DNA elements which result in modifying the chromatin accessibility. (Kundaje et al., 2015; Mathelier et al., 2015) *Cis*-acting DNA elements or *cis*-regulatory elements (CREs) are typically non-coding DNA sequences bearing binding sites for transcription factors and DNA regulatory molecules. The most popular CREs are promoters, enhancers, silencers and insulators. (Wittkopp and Kalay, 2011) The *trans*-acting elements are transcription factors and DNA regulatory proteins required for the assembly of the transcriptional machinery on the *cis*-regulatory elements. The *trans*-acting elements bind to *cis*-regulatory regions on accessible chromatin and modulate transcription of target genes. (Figure 3.5)

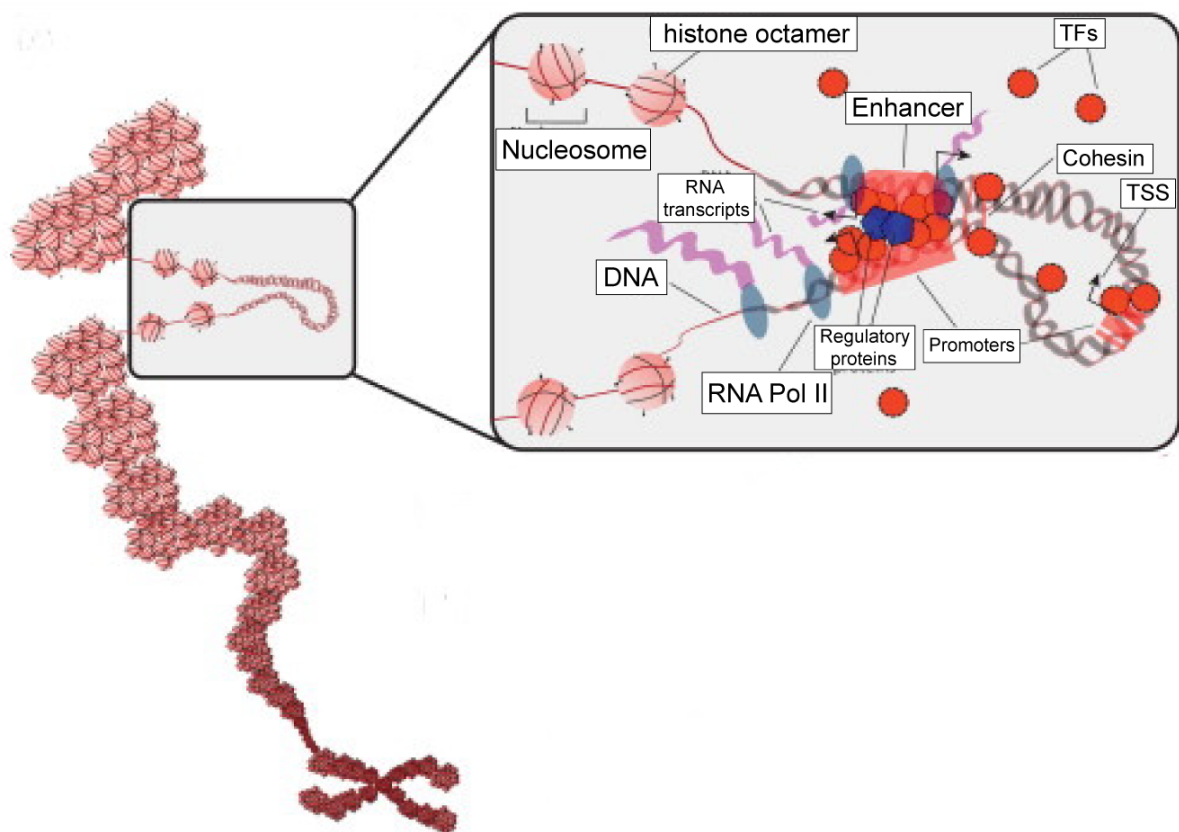


Figure 3.5: Overview of *cis*- and *trans*-regulatory elements.

Gene expression is the outcome of the interplay between *cis*- and *trans*-regulatory elements. Figure adopted and modified from (Mathelier et al., 2015)

Transcription factors regulate gene expression in two levels; firstly, they bind to enhancers (more) and promoters (less) and secondly, they recruit co-activators and histone modifying enzymes to target regions. Both ways define chromatin accessibility and therefore play a crucial role to determine and maintain cell states. (Graf and Enver, 2009)

Transcription factors comprise of 8% of the genes in human and nearly 49% of them are tissue specific. This explains why the gene regulatory landscape of most tissues is determined by the

expression level as well as functionality of their transcription factors. (Shema et al., 2019) Furthermore, it provides clues on why mutations in transcription factors are often deleterious. Conventionally, mutations in transcription factors are known to be associated with tumorigenesis and developmental syndromes in different organs. (Lambert et al., 2018) CDX2 mutation in colorectal cancer (Salari et al., 2012), SOX2 mutation in esophageal squamous cell carcinoma (Bass et al., 2009), Lmx1b mutation in Nail-Patella Syndrome (Dreyer et al., 1998), Wt1 mutations in Denys-Drash Syndrome and Frasier Syndrome are only a few to name. (Klamt et al., 1998; Mueller, 1994) Figure 3.6 enlists only some of the human disease phenotypes raised by transcription factor dysregulation.

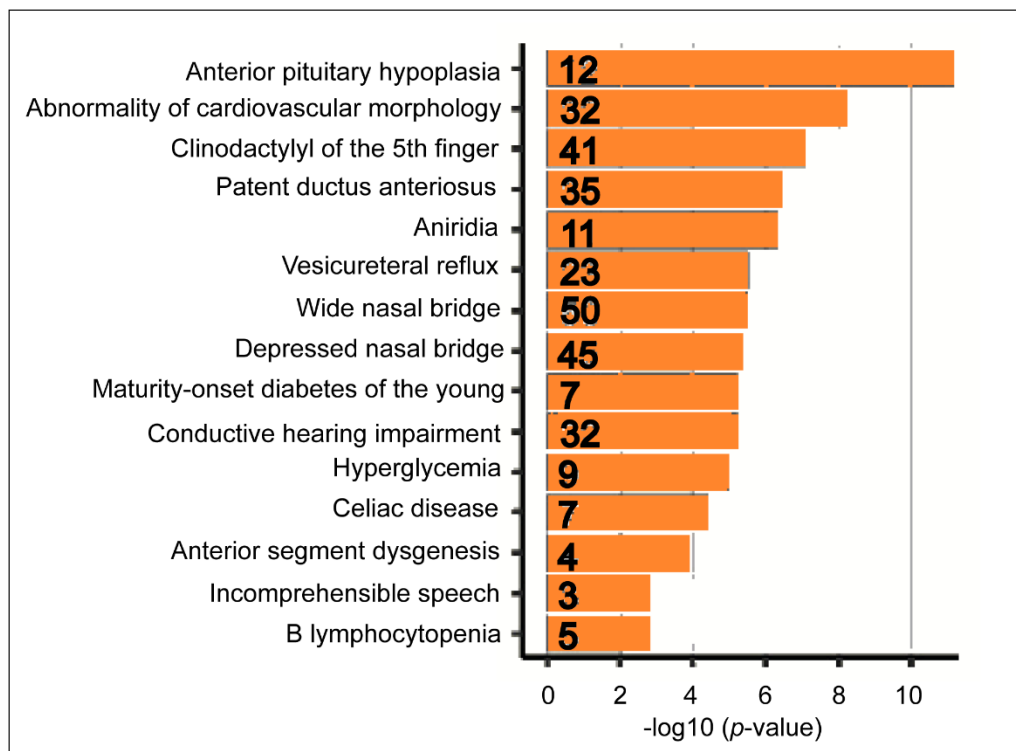


Figure 3.6: Human disease phenotypes caused by TF dysregulation.

Each bar represents genes contributing to the annotation. Values within bars indicate number of TFs associated with each annotation. The significance of the size of the intersection between the set of human TFs and the indicated gene sets is shown on the X axis. Figure adopted and modified from (Lambert et al., 2018)

In kidneys, not only a handful of developmental syndromes and malignancies are attributed to transcriptional dysregulation, but also the onset or progression of chronic kidney disease (CKD) is associated with mutations in transcription factors and/or transcriptional re-programming. (Hishikawa et al., 2018) Relevant examples of such event in podocytes is mutations in the Wt1 and Lmx1b genes which results in the development of podocyte injury and glomerular sclerosis.(Boyer et al., 2013; Iijima et al., 2012; Menke et al., 2003) Furthermore, solid evidence advocates the contribution of transcription factors in other forms of podocyte damage in which transcription factors are genetically intact. (Gebeshuber et al., 2013; Zhou et al., 2008) Despite of the existing knowledge surrounding TF functions in

podocytes, it is still unclear how the podocyte TF network (re)programs podocytes in response to internal and/or external offenses.

### 3.3 The podocyte transcription factor repertoire

Cellular processes are mostly executed by proteins which function via cooperating with other proteins. (Marcotte et al., 1999) Transcription factors are not exempt from this general rule in that they must cooperate in their gene regulatory functions. (Lambert et al., 2018) Cooperative function is advantageous in a cell in different ways. First, transcription factors cooperation offers combinatorial regulation which, *per se*, sets the ground for higher number of individual expression states without the need to produce different types of transcription factors. (Kato et al., 2004) Second, cells enjoying combinatorial regulation are more likely to be able to maintain certain regulatory functions when a transcription factor is non-functional. (Tsankov et al., 2006)

Analyzing Wt1ChIPseq in mice, our group was first to suggest podocytes enjoy an intricate network of transcription factors consisting of Wt1, Tead1, MAFB, Fox TFs, TCF21, LMX1B. (Figure 3.7) These transcription factors cooperate on podocyte-specific enhancers to drive their gene regulatory functions. (Kann et al., 2015) It is yet unknown which key podocyte pathways are co-directed by these master transcription factors.

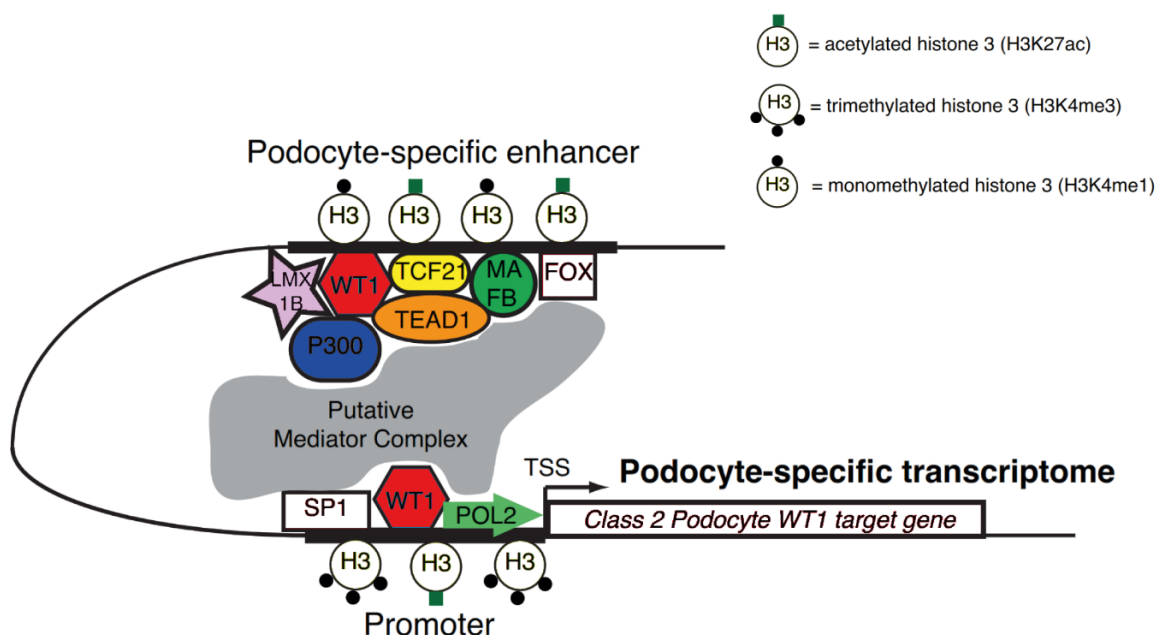


Figure 3.7: Wt1-dependent transcriptional network in podocyte.

Wt1 cooperatively binds to podocyte-specific enhancers. The podocyte transcription factor (TF) network consists of Wt1, Lmx1b, Fox family TFs, TCF family TFs, MAFB, etc. Figure adopted and modified from (Kann et al., 2015)

The Wilm's tumor 1 (Wt1) is an indispensable transcription factor for podocyte development and function. Mutations in Wt1 lead to different renal diseases ranging from severe congenital

disorders (such as Wilm's tumor or nephroblastoma, Denys-Drash syndrome, Frasier syndrome) to less severe but yet persistent and compelling disorders (such as minimal change disease and FSGS). (Baird et al., 1992; Klamt et al., 1998; Pelletier et al., 1991; Ruf et al., 2004) TEAD transcription factor family is encoded by different genes and varying expression profiles in different tissues. (Gibault et al., 2018) TEADs act as downstream mediators of Hippo pathway which is well-known for its role in regulation of organ growth. (Ma et al., 2019)

Although a fair amount of literature exists on the role of Wt1 and Tead1 in podocytes, the knowledge surrounding how these two transcription factors drive the cellular machinery in podocytes under healthy and damage conditions is still in its infancy. In this thesis, ChIP sequencing and RNA sequencing techniques are employed together with numerous data analysis approaches to uncover the gene regulatory networks governed by Wt1 and Tead1.

### **3.4 Transcriptomic analysis in kidneys**

In the context of transcriptional regulation, transcriptomic analysis links genomic features to gene function. In this sense, gene regulation studies are incomplete without a proper assessment of gene expression. In the past decades, RNA sequencing of a number of cells or tissue samples (bulk RNA) was the most precise approach to study RNA expression dynamics. However, unraveling the cell-type specific transcriptome was a longstanding enigma until the introduction of high resolution single-cell RNA sequencing in 2009. (Tang et al., 2009) Over the past decade, successive methodological developments have been introduced to the field, all of which are directed to explore cell type diversity within a tissue. (Svensson et al., 2018)

In the field of kidney research, several groups have directed their focus on using single cell RNA sequencing to answer hundreds of existing questions. Single cell transcriptomic of whole kidney from healthy mice suggests the existence of a novel transitional cell type which is mainly governed by Notch signaling. Employing the technique, authors claim that hereditary kidney disease with same pathological characteristics are likely to be originated from the same differentiated type of cells. (Park et al., 2018) In another study, single cell RNA sequencing of mouse developing kidneys shows that in the initial phases of nephrogenesis, single cell transcriptome signatures display several cellular pathways. During lineage specification, combinatorial gene repression and activation determines cellular fate in kidneys. (Brunskill et al., 2014) A separate study reveals a signaling crosstalk between the three main cell types of the collecting ducts using single cell RNA sequencing of mouse collecting duct cells. (Chen et al., 2017)

Despite all such studies, an exhaustive characterization of glomerular cells was still missing. The function of glomeruli is central in the kidney filtration apparatus. Glomerulus is composed of three main cell types: podocytes, endothelial cells and mesangial cells. Glomeruli are constantly exposed to physiological signals such as fluctuating blood shear stress along the capillaries and intra/extra cellular mechanical strain. In normal healthy kidneys, glomerular cells adapt themselves to the changing blood pressure and mechanical strain. Glomerular

disease is often accompanied by a dysregulated response to such stimuli. While the glomerular cell types have been identified for decades now, it remains unclear whether physiological cues induce individual cell response within the glomerulus. In this thesis, the glomerular cell type heterogeneity in wildtype mice is investigated using single-cell RNA sequencing. This technique offers a high-throughput transcriptome profiling of individual cells to identify cell-type subsets as well as novel markers of known cell populations.

## 4 Aims of thesis

Podocyte homeostasis is governed by the coordinated actions of an intricate network of transcription factors as well as epigenomic regulators. When compromised, podocytes undergo extensive characteristic changes leading to malfunctioning of these cells within the filtration apparatus of the kidneys. If such condition is persistent, it is often accompanied by proteinuria and the loss of podocytes leaving a scar behind. This is known as focal segmental glomerulosclerosis (FSGS), a common phenomenon in majority of the glomerular disease. If progressed, the disease of the glomeruli can lead to the loss of renal function. The existing knowledge about the gene regulation in podocytes is still missing key aspects in healthy podocytes let alone upon podocyte damage. Therefore, any palliative/curative attempt at the bedside depends on an exhaustive knowledge on the key regulators of gene expression in podocytes. This doctoral thesis is an attempt to unravel some but not all aspects of the gene regulatory networks in podocytes. To this end, this doctoral thesis covers the following three specific aims:

- 1- Characterization of Wt1-dependent gene regulatory network in a hereditary mouse model of FSGS (*Wt1<sup>het del</sup>* mice)

There are numerous studies on the role of Wt1 in podocyte development and homeostasis. (Morrison et al., 2008) Our lab was first to investigate the Wt1-dependent gene regulatory network in healthy podocytes *in vivo*. Wt1 cooperates with a panel of other TFs to govern podocyte-specific transcriptome in normal physiological conditions. (Kann et al., 2015) Of note, reduced levels of Wt1 is involved in the pathogenesis of FSGS. (Guo et al., 2002; Iijima et al., 2012) However, it is not known which Wt1-dependent gene regulatory circuits are involved in the development and progression of FSGS. In this thesis, Wt1 heterozygous deletion mouse model is used as a model for hereditary FSGS to investigate the role of Wt1 in the development and progression of podocyte disease. Differential binding on genomic features was assessed using chromatin immunoreaction followed by sequencing in the early phase of FSGS development. Differential gene expression was evaluated by RNA sequencing in early and late phases of FSGS and combined by the ChIPseq results to explore pathway perturbation in the course of disease.

- 2- *In vivo* characterization of Tead1-dependent gene regulatory network in healthy male CD1 mice

The studies surrounding the role of Hippo pathway in kidneys have mainly focused on the Yap and Taz transcriptional co-activators and cystic kidney disease. (Müller and Schermer, 2019; Rinschen et al., 2017; Wong et al., 2016) To date, no investigation is done on the role of TEADs in kidneys let alone in podocytes. In this thesis, chromatin immunoprecipitation followed by sequencing is performed in healthy male CD1 mice to unravel the Tead1-dependent gene regulatory network in podocytes. Moreover,



cooperative binding of Tead1 and Wt1 is assessed in genomic regions and the dependent functions of this cooperation is introduced.

3- Characterization of glomerular cell transcriptome on a single cell resolution to address cell-to-cell diversity

Glomeruli is composed of three main cell types: podocytes, endothelial cells and mesangial cells. However, the cellular heterogeneity of healthy glomeruli was not properly addressed to date. Using a nanodroplet-based highly parallel transcriptional profiling technique, the cellular features of isolated mouse glomeruli were re-investigated. Furthermore, a new immunofluorescent staining approach was employed to validate the findings on protein level.

## 5 Materials and Methods

### 5.1 Materials

#### 5.1.1 Chemicals

Table 5-1: List of chemicals, reagents and solutions

<i>Chemicals/reagents/solutions</i>	<i>Product no.</i>	<i>Provider</i>
1-Thioglycerol	M1753	Sigma
37% Formaldehyde Solution	4979.1	Th. Geyer GmbH
Acetic Acid	49199	Sigma
Bovine Serum Albumin	A9418	Sigma
Chloroform	1.02445.1000	Merck
D1000 DNA Ladder	5067-5586	Agilent
D1000 Sample Buffer	5067-5602	Agilent
D-Fructose	F0127	Sigma
Dimethyl Sulfoxide (DMSO)	A3672,0100	AppliChem
Dithiothreitol (DTT)	R0862	Thermo Fisher
dNTPs	R0182	Thermo Fisher
Dulbecco's Modified Eagle Medium (DMEM)	D6429	Sigma
Dynabeads M-450 tosylactivated	140.13	Invitrogen
Ethanol absolute	9065	Carl Roth
Ethidiumbromide solution 1%	2218	Carl Roth
Ethylenediaminetetraacetic acid disodium salt dihydrate (EDTA)	60-00-4	Sigma
Fetal Bovine Serum (FBS)	10270-106	Gibco
Gelatin	4070	Merck
Glutamax	35050-038	Gibco

Glycerol	3783	Carl Roth
Glycine	3908.3	Carl Roth
Glycogen	G8751	Sigma
Heparin	3862340	Rotexmedica
Histomount	HS-103	National Diagnostics
Isopropanol	5752.3	Carl Roth
Ketamine hydrochloride solution (Ketavet)	K-002	Merck
Lipofectamine® RNAiMAX Transfection Reagent	13778150	Thermo Scientific
Lithium Chloride	203637	Sigma
Magnesium Chloride	1.05833.0250	Merck
Magnetic Dynabeads	14203	Thermo Fisher Scientific
Matrigel	356231	BD Bioscience
Mayer's Hematoxylin Solution	MHS1	Sigma
mCas9 mRNA	L-6125-20	TriLink
Methanol	4627	Carl Roth
N,N,N',N'tetramethylethylenediamine (TEMED)	2367	Carl Roth
Periodic Acid 99%	3257	Carl Roth
Phenol:Chloroform:Isoamyl Alcohol 25:24:1	P2069	Merck
Polyacrylamide	T802	Carl Roth
Potassium Chloride	6781	Carl Roth
Power SYBR® Green PCR Master Mix	4368702	Invitrogen
Protease inhibitors	11697498001	Roche
Pure acetic acid 99% -100%	7332	Carl Roth
REDTaq® ReadyMix™ PCR Reaction Mix	R2523	Sigma
RNA Screen Tape Sample Buffer	5067-5577	Agilent

RNase-free water Ultra-Pure	10977-035	Invitrogen
Rompun 2%	DIN 02169592	Bayer
Schiff's Reagent	1.090.330.500	VWR
SDS pellets	CN30	Carl Roth
Sodium Chloride	S5886	Sigma
Sodium deoxycholate	D6750	Sigma
Sodium hydrogen carbonate	106329	Merck
Sodium hydroxide solution	T135	Carl Roth
Sodium(di-)hydrogenphosphate heptahydrate	SIALS9390	Sigma
Sodium(tetra-) diphosphate decahydrate	106591	Merck
TRI Reagent	93289	Sigma
Tris Base	T1503	Sigma
Tris Hydrochlorid (HCl)	9090.3	Sigma
Triton X-100	A4975,1000	Applichem
Trypsin-EDTA Solution (1x)	T3924	Sigma
Tween®20	3472	Caesar & Lorentz
Vectashield Mounting Medium with DAPI	H1200	Vector Laboratories
Water PCR Reagent	R2523	Sigma
Xylol >98%	0371.5000	Geyer

## 6 Kits and assays

Table 6-1: List of kits and assays

<b><i>Name</i></b>	<b><i>Product no.</i></b>	<b><i>Provider</i></b>
Creatinine Urinary Colorimetric Assay Kit	500701	Cayman
DNA Screen Tape	5067-5582	Agilent
GeneJet PCR purification kit	K0702	Thermo Scientific
High Capacity cDNA Reverse Transcription Kit	4368814	Applied Biosystems
HiScribe T7 High Yield RNA Synthesis Kit	E2040S	New England Bio Labs
miRNeasy Mini Kit	217004	Qiagen
Mouse Albumin ELISA Kit	E-90AL	Immunology Consultants Laboratory
RNA Screen Tape	5067-5576	Agilent
RNeasy mini kit	74104	Qiagen

### 6.1.1 Buffers and solutions

Table 6-2: List of buffers and solutions

<b>Name</b>	<b>Ingredients</b>
0.3mM NaCl RIPA	10 mM Tris-HCl pH 7.4 300 mM NaCl 1 mM EDTA 0.1% Triton X-100 0.1% SDS 0.1% Sodium Deoxycholate
0.4mM NaCl RIPA	10 mM Tris-HCl pH 7.4 400 mM NaCl 1 mM EDTA 0.1% Triton X-100 0.1% SDS 0.1% Sodium Deoxycholate
0M NaCl RIPA	10 mM Tris-HCl pH 7.4 1 mM EDTA 0.1% Triton X-100 0.1% SDS 0.1% Sodium Deoxycholate
10x HBSS Solution 1	5.4 mM KCl 0.3 mM Na <sub>2</sub> HPO <sub>4</sub> x 7H <sub>2</sub> O 0.4 mM KH <sub>2</sub> PO <sub>4</sub> 4.2 mM NaHCO <sub>3</sub> 137 mM NaCl 5.6 mM D-glucose Add ddH <sub>2</sub> O to 1 liter and adjust pH to 7.4 filter sterilize and keep at 4°C
10x HBSS Solution 2	1.3 mM CaCl <sub>2</sub> x 2H <sub>2</sub> O 0.5 mM MgCl <sub>2</sub> x 6H <sub>2</sub> O

	0.6 mM MgSO <sub>4</sub> x 7H <sub>2</sub> O Add ddH <sub>2</sub> O to 1 liter and keep at 4°C
1x HBSS	100 ml 10x Solution 1 100 ml 10x Solution 2 Add ddH <sub>2</sub> O to 1 liter and keep at 4°C
250mM LiCl Buffer	250mM LiCl 1mM EDTA 10mM Tris-HCl pH 7.4 0.5% NP-40 0.5% Na-Deoxycholate in ddH <sub>2</sub> O
500mM LiCl Buffer	500mM LiCl 1mM EDTA 10mM Tris-HCl pH 7.4 0.5% NP-40 0.5% Na-Deoxycholate in ddH <sub>2</sub> O
Anesthesia Solution	6.8 ml 0.9% NaCl 1 ml 100mg/ml Ketavet 0.4 ml Rompun
Base Solution (1x)	0.5 ml Base solution (50x) 24.5 ml ddH <sub>2</sub> O pH 12
Base Solution (50x)	12.5 ml NaOH (5N) 1 ml EDTA (0.5 M) 36.5 ml ddH <sub>2</sub> O
Chromatin Buffer	25% v/v 10% Triton X-100 25% v/v 1% Deoxycholate 25% v/v 1% SDS

	25% v/v 1.4 M NaCl
Clearing Solution	200 mM Boric Acid 4% SDS pH 8.5
Colloidal Coomassie Solution	80% Colloidal Coomassie Stock solution 20% (v/v) Methanol
Colloidal Coomassie Stock Solution	755 mM (NH <sub>4</sub> ) <sub>2</sub> SO <sub>4</sub> 2.55% (v/v) Phosphoric acid 0.1% (w/v) Coomassie brilliant blue G250
Fixing solution for Coomassie	25% (v/v) Isopropanol 10% (v/v) Acetic Acid
Hydrogel Solution	4% v/v Acrylamide 0.25% w/v VA-044 initiator PBS 1X
Laemmli Sample Buffer (2x)	100 mM Tris 4% (w/v) SDS 20% (v/v) Glycerol Bromphenol Blue 100 mM DTT pH 6.8
Neutralization Solution (1x)	0.5 ml of stock sol. 50X 24.5 ml ddH <sub>2</sub> O pH 5
Neutralization Solution (50x)	15.75 g Tris-HCl in 50 ml of ddH <sub>2</sub> O
Nuclei Lysis Buffer	50 mM Tris-HCl pH:8 10 mM EDTA 0.5% SDS in ddH <sub>2</sub> O
PBST	0.1% Triton-X



	1X PBS
Permeabilization Buffer	0,35 g Gelatin 50 ml PBS with Ca <sup>2+</sup> and Mg <sup>2+</sup> 0.5% Triton-X
Running Buffer	25 mM Tris 192 mM Glycine 0.1% (w/v) SDS
SDS Elution Buffer	1% SDS 10mM EDTA 50mM Tris-HCl pH 7.4 in ddH <sub>2</sub> O
Sonication Buffer	1mM DTT 0.25% Sarcosine 1x 0.3mM NaCl RIPA
Stacking Gel	250 mM Tris 5% (v/v) PAA 0.2%(w/v) SDS pH 6.8
TAE (1x)	40 mM Tris 20 mM Acetic Acid 1 mM EDTA pH 8.5
Tail Lysis Buffer	0.2% SDS 100 mM Tris pH: 8.5 5 mM EDTA 200 mM NaCl in 50 ml of ddH <sub>2</sub> O
TE Buffer	1mM EDTA 10mM Tris-HCl pH 7.4 in 50 ml of ddH <sub>2</sub> O

## 6.1.2 Oligonucleotides

Table 6-3: List of oligonucleotide sequences

<b>Primer name</b>	<b>Sequence (5'-&gt;3')</b>
<i>Bmp7</i> fp (ChIP-qPCR)	TACAAGTCCGGAGAGCGAGT
<i>Bmp7</i> rp (ChIP-qPCR)	AGATCGGAAAGGGGTTTGT
<i>Cre</i> fp (genotyping PCR)	GCATAACCAGTGAAACAGCATTGCTG
<i>Cre</i> rp (genotyping PCR)	GGACATGTTTCAGGGATCGCCAGGCG
<i>Flag-Tead1</i> fp (CRISPR T7 assay)	CTTACTATGCAGCTTGTAGAAGCAGTATATT
<i>Flag-Tead1</i> rp (CRISPR T7 assay)	CCCTGAAAGGAATGTTCCAGGCCACTTACCATAC
<i>Flag-Tead1</i> transgenic fp (genotyping PCR)	GACTACAAAGACGATGACGACAAGGGC
<i>Flag-Tead1</i> transgenic rp (genotyping PCR)	CCCTGAAAGGAATGTTCCAGGCCACTTACCATAC
<i>Flag-Tead1</i> wildtype fp (genotyping PCR)	TCTGTCTCCCACTACTGCATCTTG
<i>Flag-Tead1</i> wildtype rp (genotyping PCR)	GTCGCTCATCCTTTCCATGT
<i>Fyn</i> fp (ChIP-qPCR)	AAATAGGAATTGGCTTGGGG
<i>Fyn</i> rp (ChIP-qPCR)	GGGAGGTTCCAGAAATAGGC
<i>GAPDHs</i> fp (ChIP-qPCR)	CAGGAGCCCAGGGAAGATACAAATA
<i>GAPDHs</i> rp (ChIP-qPCR)	ACGCATACACATATACAACCAAGTCA
<i>Gas1</i> fp (ChIP-qPCR)	CCGCGAGGCTTTAAATACAA
<i>Gas1</i> rp (ChIP-qPCR)	CGGAGAGTGGAGAAAGGAGA
<i>Jmjd1a</i> fp (ChIP-qPCR)	GCAGCTCCATTCTTCCATTT
<i>Jmjd1a</i> rp (ChIP-qPCR)	GTCATGATCCTGGGTCTC
<i>Lats2</i> fp (ChIP-qPCR)	GCGGCGGCTCCATCTTCC
<i>Lats2</i> rp (ChIP-qPCR)	GGAGTGACGCGGGAGGAG
<i>mTmG</i> transgenic rp (genotyping PCR)	TCAATGGGCGGGGGTTCGTT
<i>mTmG</i> wildtype fp (genotyping PCR)	CTCTGCTGCCTCCTGGCTTCT

<i>mTmG</i> wildtype rp (genotyping PCR)	CGAGGCGGATCACAAGCAATA
<i>Nphs1</i> -Peak1 fp (ChIP-qPCR)	AAGAGAGAAGGGCGAGTTAG
<i>Nphs1</i> -Peak1 rp (ChIP-qPCR)	AATCAGGTGGCAAGTTCTG
<i>Nphs1</i> -Peak2 fp (ChIP-qPCR)	AGTTGACCCAGTGGTTACG
<i>Nphs1</i> -Peak2 rp (ChIP-qPCR)	TGGCGCTCAGCTTCTTAG
<i>Nphs2</i> fp (ChIP-qPCR)	ATGGTGGGGAGGAGAAGG
<i>Nphs2</i> rp (ChIP-qPCR)	TGAACCCGGTCCTAAACAAC
$\beta$ -globin fp (genotyping PCR)	TGCTCACACAGGATAGAGAGGGCAGG
$\beta$ -globin rp (genotyping PCR)	GGCTGTCCAAGTGATTCAGGCCATCG
<i>Sulf1</i> fp (ChIP-qPCR)	TGCTCCTCCTCTTCTTGAA
<i>Sulf1</i> rp (ChIP-qPCR)	GATAAACTGCCCGACCTGA
<i>Synpo</i> fp (ChIP-qPCR)	AGGTCCTTCTGGGGAAAG
<i>Synpo</i> rp (ChIP-qPCR)	TGGTCATAGGCTGATCCC
<i>Vegfa</i> fp (ChIP-qPCR)	AAGCTAGAGCGGTGGGAGAG
<i>Vegfa</i> rp (ChIP-qPCR)	CTTTGCTGTCACTGCCGTTT
<i>Wt1</i> PKG rp (genotyping PCR)	CCATTTGTCACGTCCTGC
<i>Wt1</i> wildtype fp (genotyping PCR)	GTGACCCGGCAGCTAGCC
<i>Wt1</i> wildtype rp (genotyping PCR)	GGAGCGTTCATCTCGGAGAC

### 6.1.3 Antibodies and enzymes

Table 6-4: List of antibodies and enzymes

<b>Name</b>	<b>Product no.</b>	<b>Provider</b>
Cald1	HPA008066	Sigma
Collagen IV	ab6586	Abcam
Collagenase II	LS004177	Worthington
Deoxyribonuclease I	A3778	Applichem
EphB1	PAB3018	Abnova
EphrinB1	AF473	R&D Systems
Go Taq Flexi DNA Polymerase	M7808	Promega
Lars2	ab187983	Abcam
mCas9	1074181	Integrated DNA Technologies
Nephrin	AF4269	R&D Systems
Nephrin	20R-NP002	Fitzgerald
Normal Goat IgG	sc-2028	Santa Cruz
Normal Mouse IgG	sc-2025	Santa Cruz
Normal Rabbit IgG	sc-2027	Santa Cruz
Podocin	P0372	Sigma-Aldrich
Protease from Streptomyces griseus	A3459	Applichem
Proteinase K	82456	Sigma
T7 Endonuclease I	M0302S	New England Bio Labs
Tead1	610922	BD Biosciences
Wt1	ab89901	Abcam
Wt1	sc-192	Santa Cruz
$\beta$ 1-integrin	9EG7	BD Biosciences

## 6.1.4 Equipment

Table 6-5: List of equipment

<b>Name</b>	<b>Product no.</b>	<b>Provider</b>
7900HT Fast Real-Time PCR System	4351405	Thermo Scientific Fisher
8-well $\mu$ -Slide	80826	ibidi
Cell Strainer, 100 $\mu$ m	10199-658	VWR
Cell Strainer, 40 $\mu$ m	10199-655	VWR
Cycler	S1000	BIO-RAD
Dumont #5 forceps	14098	WPI
Dumont #55 forceps	14099	WPI
DynaMag Magnet	12321D	Thermo Scientific Fisher
EnSpire Multimode Plate Reader	2300-0000	Perkin Elmer
Eppendorf LoBind microcentrifuge tubes	Z666521	Sigma
Fast thermal cycling 96- well plates	4346907	Applied Biosystem
Focused-ultrasonicator	M220	Covaris
Gel cassette 1mm	NC2010	Invitrogen
Glass bottom dish	P35G-1.5-14-C	MatTek
Glass cuvette	631-9511	VWR
Heating block	TH 21	Ditabis
Horizontal electrophoresis system	L 40-1214	PeqLab
Horizontal electrophoresis system	S 40-0708	PeqLab
Incubator	BD 115	Binder
Incubator (cell culture)	MCO-20AIC	Sanyo
Leica SP8	-	Leica

Micro tubes (1.5ml)	72.690.001	Sarstedt
Microcentrifuge	5421	Eppendorf
Microtome	RM2235	Leica
Multichannel pipette	316-3706	VWR
Nanodrop Spectrophotometer	1000	PeqLab
Odyssey CLx Imager	-	LI-COR Inc
Office scanner	C224e	Konica Minolta
Operating scissor	501754	WPI
Phase Lock Gel microcentrifuge tubes	733-2478	5Prime
Pipetteboy acu	613-4438	Integra
Pipettes: Research plus 3Pack Option 1	613-1143	Eppendorf
Polypropylene conical tube (15 ml)	734-0451	VWR
Polypropylene conical tube (50 ml)	734-0448	VWR
Rotiabo®-syringe filters, 0.22µm	P666.1	Carl Roth
Rotiabo®-syringe filters, 0.45µm	P667.1	Carl Roth
Safe Lock 1.5ml Eppendorf tubes	301 23 328	LMS
Slidescanner	SCN400	Leica
STED superresolution and confocal microscope	-	Leica
Sterile hood	Mars Safety Class 2	SCANLAF
Stripettes (10 ml)	4101	LMS
Stripettes (25 ml)	4251	LMS
Stripettes (5 ml)	4051	LMS
Suction pump	181-0067DE	VWR
Suction pump (cell culture)	HLC	DITABIS
SuperFrost®/Plus microscope slides	H867.1	Th.Geyer Group

Syringe (1ml)	7392/2007	BD
Thermoshaker	444-0823	Grant
TipOne (0.1-10 µl XL), sterile	S1110-3810-c	Starlab
TipOne 101-1000µl graduated, sterile	S1111-2831-c	Starlab
TipOne 1-200µl beveled, sterile	S1111-1816-c	Starlab
UV Transilluminator system	-	INTAS UV-System
Vannas Scissors	500086	WPI
Vortex Mixer	444-1372	VWR
Water bath	HBR4	IKA
Water bath (for paraffin sections)	HI1210	Leica

## 6.1.5 Software

Table 6-6: List of software

<b><i>Software</i></b>	<b><i>Version no.</i></b>	<b><i>Provider</i></b>
Adobe Illustrator	22.0.1	Adobe
Adobe Photoshop	11.0	Adobe
DataAssist	3.01	Applied Biosystems
GraphPad Prism 5 for Windows	6.05	GraphPad Software Inc.
ImageJ/Fiji	-	Wayne Rasband
ImageScope	12.0.1.5030	Aperio
ImageStudio	5.2	LI-COR
LAS X software	3.1.5	Leica Microsystems, Wetzlar, Germany
LSM Software	-	Zeiss
Mausoleum	6.6.1	H.E. Stöffler
Microsoft Office Suite	2010	Microsoft
Nanodrop 1000	3.7	Thermo Scientific
QuPath	0.1.2	Queen's University Belfast
SDS Software	2.4	Applied Biosystems
TapeStation	A.02.01	Agilent Technologies
ZEN Software	2009	Zeiss
Zotero	5.0.74	-



## 6.2 Methods

### 6.2.1 Cell culture

#### 6.2.1.1 Culture of immortalized cell lines

Monolayer cultures of cells were maintained in their respective media at 37°C under 5% CO<sub>2</sub> condition. Inner mouse collecting duct (mIMCD3) cells were cultivated in DMEM:F12 media supplemented with 10% FBS and 1x Glutamax to optimize the Tead1ChIPseq protocol. Mouse Motor Neuron (NSC-34) cells were cultivated in DMEM media supplemented with 10% FBS and 1x Glutamax to perform cell transfection for CRISPR/Cas9 mediated genome editing.

For passaging, cells were washed with 1x PBS without Ca<sup>2+</sup> and Mg<sup>2+</sup> and trypsinization was complete by adding 1 ml Trypsin for 2-5 min at 37°C. The reaction was stopped by addition of media and the cells were seeded in a sterile 10-cm culture dish with pre-warmed media in desired ratios for mIMCD3 and NCS34 cells, respectively. Cells were passaged two times per week to maintain the line and they were only passaged up to 10 times to avoid abnormal cell growth and morphology. Table 6-7 enlists the cell lines used during this thesis.

Table 6-7: List of cell lines

<i>Name of the cell line</i>	<i>Provider</i>
mIMCD3 (Mouse Inner Medullary Collecting Duct Cells)	Nephrolab, Cologne
NSC-34 (Mouse Motor Neuron-like cells)	Nephrolab, Cologne

#### 6.2.1.2 Freezing and thawing of cells

For freezing, cells were washed with 1x PBS without Ca<sup>2+</sup> and Mg<sup>2+</sup>. After trypsinization, cells were re-suspended in 9 ml of fresh pre-warmed media and centrifuged for 5 min at 1000 rpm at 4°C. The pellet was re-suspended in 1 ml freezing medium containing 45% DMEM, 45% FBS and 10% DMSO. Cells were quickly transferred into a cryovial and gradually frozen in a freezing chamber at -80°C. For thawing, cells were thawed by dipping the cryovials in pre-warmed water bath at 37°C for 1 min and the cell suspension was mixed with 5 ml fresh media. After centrifugation for 5 min at 1000 rpm at 4°C, the cell pellets were re-suspended in 9 ml pre-warmed fresh media and seeded in a sterile culture dish accordingly.

#### 6.2.1.3 Co-transfection with mCas9 and gRNA

For transfection, cells were grown to a confluency of 50% in 6-well sterile culture dishes and transfected with Lipofectamine RNAimax (final concentration: 20 nM), gRNA (total amount: 700 µg) and mCas9 RNA (total amount: 1µg/ul). Transfected cells were incubated for 24-48 h and then trypsinized to perform the T7 endonuclease I assay.

## 6.2.2 CRISPR/Cas9-mediated genome editing

### 6.2.2.1 Design and production of small guide RNA

*In silico* guide RNA design was performed in Benchling using the following settings: *NGG* was assigned as the desired Protospacer Adjacent Motif (PAM) sequence and the sgRNA length was adjusted to 20 nucleotides. The sequence for the gene of interest was queried using the *Mus musculus* reference genome mm10. Aiming for insertion of a single *Flag*-tag after the start codon, a region spanning approximately 100 bp around the start codon was selected as input for the gRNA design algorithm in Benchling. Best-matching oligo template was selected and a 60-bp custom oligo was ordered containing the following elements (5'→3')

- 1- T7 RNA polymerase recognition sequence (TTAATACGACTCACTATAGG)
- 2- 20-bp oligo template (NNNNNNNNNNNNNNNNNNNNNN)
- 3- Cas9 recruiting sequence (GTTTTAGAGCTAGAAATAGC)

sgRNA was generated *in vitro* using T7 RNA polymerase and pSpCas9(BB)-2A-Puro (PX459) V2.0 plasmid (Addgene # 62988) from Feng Zhang's lab and purified using miRNeasy Mini Kit. (Ran et al., 2013) Table 6-8 enlists all the designed guide RNAs. The *Tead1* sgRNA has been used in this thesis and the other three sgRNAs are designed for other projects.

Table 6-8: List of designed guide RNA

<b><i>Gene of interest</i></b>	<b><i>gRNA sequence</i></b>
<i>KLF15</i>	TTAATACGACTCACTATAGGGCTCGGCCAGGCCAGCATGGGTTTTAGAGCTAGAAATAGC
<i>MafB</i>	TTAATACGACTCACTATAGGCTCGCTTTTAGCGATGGCCGGTTTTAGAGCTAGAAATAGC
<i>TCF21</i>	TTAATACGACTCACTATAGGACCTCTCTAAACATGTCCACGTTTTAGAGCTAGAAATAGC
<i>Tead1</i>	TTAATACGACTCACTATAGGGCCCTGCCGAAAACATGGAAGTTTTAGAGCTAGAAATAGC

### 6.2.2.2 T7 endonuclease I assay

Genomic DNA from transfected NCS34 cells was extracted using the HotSHOT extraction method. (Truett et al., 2000) In brief, samples were incubated in 50-150 µl Base solution for 30min at 95°C followed by incubation on ice for 5 minutes. The reaction was stopped by addition of 50-150 µl Neutralization solution. PCR was run using REDTaq® ReadyMix™ PCR reaction mix and two primers flanking the sgRNA region to amplify a window of 300-500 bp. The PCR products were purified using GeneJet PCR purification kit and 200 ng of the purified

DNA was incubated for hybridization reaction. Table 6-9 enlists the reaction composition and the cycling conditions used for hybridization reaction.

Table 6-9: Hybridization reaction reagents and cycling conditions

<b>Reaction mix</b>	<b>Step</b>	<b>Cycling condition</b>
DNA 200 ng	Initial denaturation	95°C 5 min
10X NEBuffer 2 2 µl	Annealing (Ramp rate)	95-85°C -2°C/second
Nuclease-free Water To 19 µl	Final hold	85-25°C -0.1°C/second 4°C forever

After this step, T7 endonuclease I reaction was performed using half of the product according to the manufacturer's protocol. The remaining DNA was kept as a negative control. T7 assay product was ran on a 2% agarose gel together with the negative control. Table 6-10 enlists the PCR reaction composition and the cycling conditions used for T7 endonuclease I assay.

Table 6-10: PCR reaction reagents and cycling conditions

<b>Reaction mix</b>	<b>Step</b>	<b>Cycling condition</b>
1x Red Taq Sigma master mix	Initialization	95°C 5 min
1 pM fp	Denaturation	95°C 60 s
1 pM rp	Annealing	60°C 60 s
~ 50 ng DNA	Extension	72°C 90 s
Add H2O to 20 µl		go to step 2, repeat 29 times
	Final extension	72°C 10 min
	Final hold	15°C forever

### 6.2.2.3 Designing single-stranded oligonucleotide donor (ssODN)

ssODN was designed complementary to the strand from which the sgRNA was designed. The ssODNs were designed asymmetrical and contained <200 nucleotides to increase the efficiency of the homology directed repair (HDR) according to the latest literature to date. (Richardson et al., 2016) The *Flag* sequence (GACTACAAAGACGATGACGACAAG) followed by a flexible spacer (GGCGGAGGGGAAGC) was inserted between the short and long homology arms. Custom-made ssODNs were ordered from Integrated DNA Technologies. Table 6-11 enlists all the designed ssODNs. The Flag-Tead1 ssODN has been used in this thesis and the other three ssODNs are designed for other projects.

Table 6-11: List of designed ssODN

<b>Gene of interest</b>	<b>ssODN sequence</b>
<i>Flag- Tead1</i>	GGGCCTCCTGGAAACTCTGCTCAATATCAGGACTCCAGACGCCCTCCGCGTC GTTGTCAATCGGCTTATCTGCCGAGTCGCTCATCCTTTTCGCTTCCCCCTCCGC CCTTGTCGTCATCGTCTTTGTAGTCCATGTTTTTCGGCAGGGCTCTCGCTGCCG CTCCAGCT
<i>Flag-KLF15</i>	GTATGGCTGCCGGCTGGCCAGCCTGTCCCCTAGGTAACCCACTGAGCATTTC GGTGACGAGAAGGTCTCGTCCACTGGAAGCAGGTGGTCCACGCTTCCCCCT CCGCCCTTGTGTCATCGTCTTTGTAGTCCATGCTGGCCTGGCCGAGCCTGTG GTGACTGCAGAG
<i>Flag-MafB</i>	TCACGTCGAACTTGAGAAGGTCTGAAGTCGTTGACGTAATCCATGGCCAGCG GGCTGGTGGGCAGCTCTTGCCCCATGCTCAGCTCCGCGGCGCTTCCCCCTCC GCCCTTGTGTCATCGTCTTTGTAGTCCATCGCTAAAAGCGAGGCTCAGCCG CCGCTGCCGCG
<i>Flag-TCF21</i>	TCCAAACTCCTTGTTGGAGTCCACTTTCAGGGAGTCACAGTCCAGCATCTCCA CCTCTGAAGGTCTTCTACATCGCTGAGGGAGCCAGTGGAGCTTCCCCCTCC GCCCTTGTGTCATCGTCTTTGTAGTCCATGTTTAGAGAGGTGGAGGGAGG GAGGGA

#### 6.2.2.4 Electroporation of zygotes

After validating steps, CRISPR/Cas9 components were submitted to the *in vivo* Research Facility, University of Cologne for generation of Flag-Tead1 transgenic mice using Easy Electroporation of Zygotes (EEZy) method in C57BL/6J mice. (Tröder et al., 2018) The EEZy reaction mix consists of mCas9 mRNA (final concentration: 50ng/μl), sgRNA (final concentration: 50ng/μl), template DNA or ssODN (final concentration: 100ng/μl) and mCas9 protein (final concentration: 30ng/μl).

To test the target recombination in F0 mice, a genotyping PCR was done on the extracted DNA from mice ear tags using previously discussed primers. The amplicons were checked on a 2% agarose gel to find the expected bands. The rest of the PCR product was used for topo cloning reaction according to the standard protocol provided by the manufacturer. After completion of the topo cloning reaction, chemical transformation of the clones into competent *E. coli* DH10B was done. Isolation of DNA from mini cultures was completed using GeneJet Plasmid Miniprep Kit and the DNA was further processed for sequencing.

#### 6.2.2.5 Sanger sequencing

To confirm the expected recombination, all inserts were sequenced using the BigDye Terminator v3.1 Cycle Sequencing Kit. Each sequencing reaction consisted of 150 ng DNA, 2 pmol of the sequencing primer primer, 0.25 μl BigDye Terminator, 2.25 μl sequencing buffer

to a final reaction volume of 10  $\mu$ l. Cycling steps were as follows: 1 min at 96°C, (10 s, 96°C; 5 s, 55°C) for 40 cycles and 4 min at 60°C. DNA was submitted to the Cologne Center for Genomics (CCG, Cologne, Germany) for Sanger sequencing. Sequence alignment and comparison of the results with the initially designed insert was performed in Benchling.

## 6.2.3 Mouse experiments

### 6.2.3.1 Mouse lines

All the mouse lines for this thesis were housed based on standardized specific pathogen-free conditions in the *in vivo* Research Facility of the University of Cologne. All mouse experiments were carried out within the guideline frame provided by the LANUV NRW (Landesamt für Natur, Umwelt und Verbraucherschutz Nordrhein-Westfalen/State Agency for Nature, Environment and Consumer Protection North Rhine-Westphalia) and were approved by the same Institution.

### 6.2.3.2 DNA extraction from mouse tissue

Ear or tail biopsies were used to extract genomic DNA using the HotSHOT method for *Flag-Tead1* and *Nphs2Cre x mTmG* mice. For *Wt1<sup>het del</sup>* mice, Proteinase K-mediated genomic DNA extraction method was used. In brief, biopsies were lysed in Tail Lysis Buffer supplemented with Proteinase K (final concentration: 0.1 mg/ml) at 60°C overnight. Extracted DNA was recovered the next day using Isopropanol and re-suspended in TE buffer.

### 6.2.3.3 Polymerase chain reaction for genotyping

REDTaq® ReadyMix™ PCR reaction mix and Go Taq Flexi DNA Polymerase 5U/ $\mu$ l were used for genotyping PCR reaction according to the manufacturer's protocol. Table 6-3 enlists the specific primer sequences for the genotyping PCRs. Detailed PCR reaction composition as well as cycling conditions for all primer pairs are listed in the Table 6-12 and Table 6-13, respectively.

Table 6-12: Genotyping PCR reaction reagents

<b><i>Gene name</i></b>	<b><i>Reaction mix</i></b>
<i>Cre</i>	1x Red Taq Sigma master mix 1.25 pM Cre fp 1.25 pM Cre rp 1.25 pM $\beta$ -globin fp 1.25 pM $\beta$ -globin rp ~ 50 ng DNA Add H2O to 25 $\mu$ l
<i>Flag-Tead1</i>	1x Green Flexi Buffer

	<p>1.5 mM MgCl<sub>2</sub>  0.2 mM dNTP (each)  1.25 pM Flag-Tead1wildtype fp  1.25 pM Flag-Tead1 wildtype rp  1.25 pM Flag-Tead1transgenic fp  1.25 pM Flag-Tead1transgenic rp  ~ 50 ng DNA  0.2 Units Taq polymerase  Add H<sub>2</sub>O to 25 μl</p>
<i>mTmG</i>	<p>1x Green Flexi Buffer  1.5 mM MgCl<sub>2</sub>  0.2 mM dNTP (each)  25 pM mTmG wt fp  17 pM mTmG wt rp  33 pM mTmG tg rp  ~ 50 ng DNA  0.2 Units Taq polymerase  Add H<sub>2</sub>O to 25 μl</p>
<i>Wt1</i>	<p>1x Green Flexi Buffer  1.5 mM MgCl<sub>2</sub>  0.2 mM dNTP (each)  1.25 pM <i>Wt1</i><sup>het del</sup> fp  1.25 pM <i>Wt1</i><sup>het del</sup> rp  1.25 pM <i>Wt1</i><sup>het del</sup> PKG cassette rp  ~ 50 ng DNA  0.2 Units Taq polymerase  Add H<sub>2</sub>O to 25 μl</p>

Table 6-13: List of PCR cycling conditions and the product sizes

<b><i>Gene name</i></b>	<b><i>Step</i></b>	<b><i>Cycling condition</i></b>	<b><i>Product size</i></b>
<i>Cre</i>	Initialization	94°C....3 min	Internal control band: 494 bp  Transgenic band: 269 bp
	Denaturation	94°C....45 s	
	Annealing	59°C....60 s	
	Extension	72°C....45 s → go to step 2, repeat 30 times	
	Final extension	72°C....10 min	
	Final hold	10°C.... forever	
<i>Flag-Tead1</i>	Initialization	94°C....2 min	Wildtype band: 586 bp  Transgenic band: 222 bp
	Denaturation	94°C....20 s	
	Annealing	55°C....15 s	
	Extension	72°C....1 min → go to step 2, repeat 34 times	
	Final extension	72°C....10 min	
	Final hold	15°C.... forever	
<i>mTmG</i>	Initialization	94°C....3 min	Wildtype band: 330 bp  Transgenic band: 250 bp
	Denaturation	94°C....30 s	
	Annealing	61°C....60 s	
	Extension	72°C....60 s → go to step 2, repeat 35 times	
	Final extension	72°C....120 s	
	Final hold	10°C.... forever	
<i>Wt1</i>	Initialization	95°C....2 min	Wildtype band: 320 bp  Transgenic band: 260 bp
	Denaturation	95°C....30 s	
	Annealing	54°C....30 s	
	Extension	72°C....2 min → go to step 2, repeat 34 times	
	Final extension	72°C....10 min	
	Final hold	15°C.... forever	

#### 6.2.3.4 Body and kidney weight analysis and urine collection

*Wt1<sup>het del</sup>* mice were weighed, and the urine was collected before sacrificing the mice. For the kidney to body weight ratio analysis, mice were sacrificed on postnatal day 6 and the kidneys were weighed accordingly. To minimize the technical errors during the experiment, the same balance was used throughout the study.

#### 6.2.3.5 Immunofluorescent staining on kidney tissue

For the immunofluorescent (IF) staining of the kidney tissue, different methods were applied in different projects according to the protein of interest and its localization in one hand and how the technique of choice can address the underlying question on the other hand.

To achieve higher resolution at the glomerular basement membrane (GBM) level, an optical clearing technique was employed prior to immunofluorescent staining for the *Wt1<sup>het del</sup>* study. (Unnersjö-Jess et al., 2018) Perfused kidneys were fixed in 4% formalin at 4°C overnight and transferred to ice-cold PBS the next day. Kidney samples were shipped to Royal Institute of Technology in Sweden under 4°C condition. Dr. David Unnersjö Jess has done the IF staining of the kidney samples for the *Wt1<sup>het del</sup>* project.

In brief, fixed pieces of kidneys were incubated at 4°C in hydrogel solution (HS) overnight. Samples were immersed in clearing solution (CS) at 50°C for 6 h. Kidney pieces were cut into 0.3 mm-thick slices using a Vibratome. Slices were incubated at 50°C in CS overnight. Before immunolabeling, samples were washed in PBST for 10 min and incubated in primary antibody for 24 h at 37°C. Next day, samples were washed in PBST for 10 min at 37°C followed by secondary antibody incubation for 24 h at 37°C. For mounting, samples were immersed in 80% (w/w) fructose with 0.5% (v/v) 1-Thioglycerol at 37°C for 1 h before imaging. Samples were mounted in a glass bottom dish and imaged using a Leica SP8 3X STED system. The antibodies used were as follows:  $\beta$ 1-integrin, Nephritin, Collagen IV, Podocin, EphB1 and EphrinB1. PBST was used as diluent for all the steps.

To address differential protein expression within glomerular cell types and overcome the inherent autofluorescence effect in the kidney tissue, a novel technique was adapted from IF staining of the spheroids in culture. (Giles et al., 2014) In brief, isolated mouse glomeruli from *Nphs2Cre x mTmG* mice in a CD1 background were seeded in Matrigel in 8-well  $\mu$ -slides. After solidification, fixation was completed using 10% PFA for 30 min at room temperature (RT) and wells were gently washed with PBS containing  $\text{Ca}^{2+}$  and  $\text{Mg}^{2+}$ . Samples were permeabilized with the permeabilization buffer for 30 minutes at RT and incubated with the primary antibody at 4°C overnight. After washing, the secondary antibody incubation was done for 4 h at RT. Samples were mounted with Vectashield and confocal stacks were acquired using a Leica SP8 confocal microscope equipped with a 63x/1.4 oil immersion objective operated with the LAS X software version 3.1.5. Image acquisition settings were comparable among all images. The antibodies used were as follows: Cald1, Lars2 and their relevant isotype controls. Permeabilization buffer was used as diluent for all the steps.



#### **6.2.3.6 Image analysis**

For the GBM thickness analysis,  $\beta$ 1-integrin signal was used to assign the inner and outer boundaries of the GBM in ImageJ and the lines were imported into MATLAB and a custom-written code was used to measure the GBM thickness in 100-nm intervals along the GBM and the GBM thickness was reported in microns by Dr. David Unnersjö Jess. The GBM thickness of relevant biological samples was plotted in GraphPad Prism 5.

For EphrinB1 signal intensity quantification, regions of interest (ROI) and the slit diaphragm (SD) were manually assigned using the podocin signal in ImageJ. The mean intensity values and SD length were obtained from ROI manager command. The EphrinB1 mean intensity was normalized to that of podocin to correct for possible technical artefacts and the Spearman correlation test was employed in R to plot the results.

#### **6.2.3.7 Periodic Acid–Schiff staining**

The kidneys were fixed in 4% formalin at 4°C overnight. The samples were soaked in cold PBS the next day and inserted in a tissue processor in the Center of Pathology, University Hospital Cologne. After complete dehydration, tissue was embedded in paraffin and sections of 4  $\mu$ m were cut and air-dried overnight on glass slides. Afterwards, sections were rehydrated and soaked in 0.9% Periodic Acid for 10 minutes and rinsed with distilled water for 1 minute. Next, the slides were soaked in Schiff reagent for 10 minutes and rinsed with tap water for 2 minutes and incubated in Mayer's Hematoxylin Solution. After washing for 8 minutes, the blue color was developed in the nuclei. Sections were dehydrated in increasing ethanol concentrations and mounted with Histomount. Images were obtained using Leica SCN400 Slide Scanner on a 40x magnification. Glomeruli of the P6 mice were manually counted in ImageJ and the glomeruli counts were reported in mm<sup>2</sup> cortex area.

#### **6.2.3.8 Colloidal Coomassie Blue staining**

Urine samples were cooked in a 1:10 ratio in a mix of 2xLaemmli buffer supplemented with Dithiothreitol and ddH<sub>2</sub>O for 5 minutes at 95°C. Samples were loaded on 10% Sodium Dodecyl Sulfate Polyacrylamide gel electrophoresis. SDS gels were incubated in 25ml fixation solution for 30 minutes at RT on a shaker. Gels were washed with slow-running tap water for a few seconds and incubated in 25 ml Colloidal Coomassie Brilliant Blue solution activated with methanol overnight at RT on a shaker. De-staining was carried out using distilled water at room temperature for 48 h. Images were acquired after complete de-staining with Odyssey CLx imaging device.

#### **6.2.3.9 Albumin to Creatinine Ratio (ACR) determination**

Urinary albumin concentration was measured with a commercially available ELISA kit according to the kit instruction. In brief, 100  $\mu$ l of the standard or diluted urine samples (1:1000) were loaded in pre-coated wells and incubated for 30 minutes at RT. After washing, secondary antibody incubation was done for 30 minutes at RT. Chromogenic substrate was added in dark and the reaction was stopped by addition of stop solution after 10 minutes. The

absorbance was determined at 450 nm on a multimode plate reader. Analysis was performed according to the kit instructions. Using the standard sample reads, standard curve was obtained, and the test sample values were interpolated accordingly. The results were corrected for the dilution factor to acquire the original values.

Urinary creatinine concentration was determined using a colorimetric assay. 15 µl of the standard or the diluted urine samples (1:20) were loaded per well. After addition of 150 µl alkaline picrate solution, the initial absorbance was measured at 490 nm. Final absorbance was determined after the addition of 5 µl acid solution at 490 nm. An equation was acquired using the linear regression of the standard curve. Creatinine levels per sample was calculated using the following equations:

*Corrected absorbance for each sample = average initial absorbance - average final absorbance*

$$\text{Creatinine} \left( \frac{\text{mg}}{\text{dl}} \right) = \left[ \text{corrected sample absorbance} - \left( \frac{Y\text{-intercept}}{\text{slope}} \right) \right] \times \text{sample dilution}$$

#### **6.2.3.10 Isolation of the glomeruli from mouse kidney**

Glomeruli were isolated from the mouse kidneys as described before. (Boerries et al., 2013) In brief, kidneys were dissected together with the abdominal aorta after cervical dislocation of the mouse and each kidney was perfused with 1-2 ml of magnetic beads solution consisting of Magnetic Dynabeads in 1x Hank's Buffered Salt Solution (HBSS). Renal capsules were removed, and kidneys were minced in 1-mm<sup>3</sup> pieces using a scalpel. Digestion was done in 3 ml of the digestion solution in 37 °C for 15 minutes on a plate shaker. To facilitate digestion, kidney pieces were triturated using a cut pipettete filter tip. Digested kidneys were meshed twice through a 100-µm cell strainer and centrifuged. Glomeruli were collected after re-suspending the pellet using DynaMag Magnet.

#### **6.2.3.11 RNA isolation**

Isolated glomeruli were homogenized in 700 µl TRI reagent and 140 µl chloroform was added to the homogenate. After centrifugation, the aqueous phase was collected, and total RNA was extracted using the miRNeasy RNA extraction kit. RNA quality was assessed on RNA screen tape and all the samples showing RNA integrity number (RIN) > 8 were submitted to the Cologne Center for Genomics (CCG, Cologne, Germany) for sequencing. Ribo-minus libraries were constructed according to the standardized protocols and paired-end sequencing was done on an Illumina HiSeq sequencer.

#### **6.2.3.12 Wt1 chromatin immunoprecipitation**

Wt1 chromatin immunoprecipitation (ChIP) was performed by Dr. Maximillian Lenz in Nephrolab, University of Cologne. Mouse kidneys from 4-week old mice were processed by dissecting the cortex from medulla and mincing. Crosslinking was performed using 1% formaldehyde in PBS followed by quenching with 125 mM glycine. Further tissue disruption was carried out using a rotor-stator homogenizer in sterile 0.3 mM NaCl RIPA supplemented

with protease inhibitor. The pellet was sonicated in the sonication buffer on a probe-tip sonicator to achieve an average chromatin size ranging between 200-600 bp. Sonication efficiency was checked on a 2% agarose gel for each ChIP round. After sonication, sample was filled up to 1 ml with 0.3 RIPA, the Protease inhibitor was refreshed, and IP was carried out overnight by adding 3 µg of Wt1 C19 antibody or IgG isotype control. Samples were incubated with Protein G Dynabeads the next day for 2-3 hours at 4°C. After washing and elution, de-cross linking was done in SDS elution buffer at 65°C overnight. DNA extraction was completed using phenol / chloroform/ isoamylalcohol 25:24:1. Following centrifugation, the aqueous phase containing the purified DNA is transferred to clean tubes and DNA is recovered by alcohol precipitation.

#### **6.2.3.13 Tead1 chromatin immunoprecipitation**

Mouse kidneys from 8 to 10-week old mice were used for isolation of glomeruli. Crosslinking was performed using 1% formaldehyde in PBS followed by quenching with 125 mM glycine. Sonication was completed in the ice-cold fresh nuclear lysis buffer (NLB) supplemented with protease inhibitors on a Covaris M220 Focused-ultrasonicator for 5 minutes. A total of 8 mice were used as input per immunoprecipitation round and the sonication efficiency was checked on a 2% agarose gel per round. Chromatin buffer was added to samples in a 2:3 ratio, protease inhibitor was refreshed, and IP was carried out at 4°C overnight by adding 6 µg of Tead1 antibody or IgG isotype control priorly bound to Protein G Dynabeads. After washing and elution, de-cross linking was done in SDS elution buffer at 65°C overnight. DNA extraction was completed using phenol / chloroform/ isoamylalcohol 25:24:1. Following centrifugation, the aqueous phase containing the purified DNA is transferred to clean tubes and DNA is recovered by alcohol precipitation.

#### **6.2.3.14 Analysis of ChIP efficacy by qPCR**

Before proceeding to sequencing, qPCR was routinely employed for each ChIP round using equal amounts of 1% Input, IgG and IP DNA in Power SYBR Green PCR master mix reaction a fast real-time PCR system. Fold enrichment analysis of ChIP DNA compared to IgG control DNA was calculated as  $2^{((Ct(IgG)-Ct(input))-(Ct(ChIP)-Ct(input)))}$ . All the primers used in qPCR experiments are enlisted in Table 6-3. To compare the fold enrichment between the positive and the negative loci, student's *t*-test with Bonferroni's correction was used. The 1% Input DNA and IP DNA samples passing the quality control check, were submitted to the Cologne Center for Genomics (CCG) for library preparation. Strand single-end library was constructed according to the standardized protocols and sequencing was performed using Illumina HiSeq sequencer.

#### **6.2.3.15 Preparation of single cells from isolated mouse glomeruli**

For single cell preparation, isolated mouse glomeruli from 8-week old CD1 male mice were re-suspended in 1 ml of tissue digestion solution and digestion was performed on a thermo-shaker set to 37°C at 1400 rpm for the total of 40 minutes. Mechanical dissociation of the glomerular structure was facilitated by vortexing, trituration through a pipette and/or gentle shearing through a 27-gauge syringe on 5-minute intervals. Next, magnetic Dynabeads were

removed and the single cells were collected by centrifugation at 5000x g at 4°C for 10 minutes. Cells were re-suspended in ice-cold PBS and sieved through a 50-µm mesh. Cell sorting was carried out on a FACS Aria III device gated for live single cells. 7-Aminoactinomycin D (7-AAD) was used to mark the dead cells. Cell fixation was done in ice-cold 80% methanol in PBS and shipped to the Max Delbrück Center for Molecular Medicine in Berlin for the preparation of monodisperse droplets for single cell RNA sequencing.

#### **6.2.3.16 Single-cell mRNA-sequencing**

Dr. Christine Kocks and Ms. Anastasia Boltengagen have performed the experiments regarding the drop-sequencing procedure, single-cell and bulk mRNA library preparation and sequencing according to an established protocol. (Macosko et al., 2015) In brief, 1-nanoliter monodisperse droplets were prepared on a drop-seq setup. During the formation of nanoliter droplets, single cells were encapsulated with individual, uniquely barcoded beads. Single cells were lysed and the polyadenylated RNA molecules were hybridized to the polyd(T) primers attached to the beads. Next, nanoliter droplets were collected and RNA molecules were captured, and paired end read library was prepared accordingly. Sequencing was performed after spiking 1% PhiX Control v3 Library on Illumina Nextseq 500 sequencer. For bulk mRNA sequencing, total RNA was extracted from isolated glomeruli or fixed single cells using TRI reagent. Single end read libraries were prepared and sequenced on Illumina Nextseq 500 sequencer.

#### **6.2.4 Bioinformatics analysis**

For the *Wt1*<sup>het del</sup> and Tead1 projects, all the NGS analyses have been done by Tim Padvitski. If not stated otherwise, plotting and data analysis was performed in R software environment (version 3.4), plotting was done using ggplot() function. Dr. Nikos Karaikos has carried out the single cell RNAseq analysis.

##### **6.2.4.1 Mapping and peak calling of ChIPseq data**

To map the ChIPseq reads on the mouse genome, mm10 was retrieved from UCSC genome browser. Mapped reads with MAPQ quality score < 30 and the duplicated reads were filtered out and the remaining reads were used to call peaks using MACS2 NarrowPeak algorithm with default parameters.

##### **6.2.4.2 Quality control**

Cross correlation analysis and IDR analysis were applied as the quality control step. Metagene plots of the nucleotide conservation and primary motif enrichment were generated for consensus *Wt1*ChIPseq and *Tead1*ChIPseq peaks in the respective samples. The nucleotide conservation around the peaks center was generated by bwtool using mm10 phastCons scores for multiple alignments of 59 vertebrate genomes to the mouse genome, retrieved from UCSCS. The primary *Wt1* and *Tead1* motif density around the peaks center was calculated with Homer software.

### 6.2.4.3 Differential binding analysis

Differential binding analysis was performed using DiffBind R package. The location of peaks was extended up to 500 nucleotides in both directions and merged into one consensus peak. Consensus peakset was derived by selecting peaks occurring in both ChIPseq samples. The input control read counts were subtracted from each site per sample and the reads from the IP samples were counted into consensus peakset. Differential binding analysis compares number of reads between wildtype and *Wt1*<sup>het del</sup> samples in each peak of the consensus peakset using DEseq2 algorithm.

Target gene inference was completed using ClosestGene algorithm from TFTargetCaller R package. The algorithm identified 602 target genes (FDR 10%) of the consensus wildtype peakset. No statistically significant targets (FDR 10%) were found using *Wt1* differentially bound sites and therefore all the assigned 602 genes were used in the downstream analysis. Genome browser plots of selected *Wt1* target genes were generated using Gviz R packages.

### 6.2.4.4 Peak annotation and region-gene association analysis

Each peak in *Wt1* and *Tead1* consensus peak sets was annotated with nearest TSS and GO term using annotatePeaks.pl tool from homer v4.9.1 suite of tools, the same tool was used to calculate distances between closest *WT1* and *Tead1* peaks.

### 6.2.4.5 *Wt1*-*Tead1* co-binding analysis

*Wt1*-*Tead1* co-binding was defined as any instance of overlap between *Tead1* and *WT1* peaks and then co-bound regions were annotated as described above.

### 6.2.4.6 Mapping and differential expression analysis of RNAseq data

Raw RNAseq reads were mapped to GRCm38.p5 mouse genome assembly using STAR. Percentage of reads uniquely mapped to mouse genome for all 12 samples was in the range between 87%-89%. Distribution of mapped tags across different groups of features (exons, introns, UTRs, etc.) was estimated using GRCm38\_GENCODE\_VM11\_comprehensive reference gene model downloaded from UCSC. Genes with average expression across all samples below 1 were excluded from the analysis. The factors of unwanted variation (possible batch effects) were estimated by RUVr function of RUV-seq R package and differential expression analysis was performed by DEseq2.

### 6.2.4.7 Hierarchical clustering and GO term functional annotation analysis

GO enrichment analysis was performed with a custom function developed by the group of Professor Dr. Andreas Beyer (<https://github.com/robertsehlke/SETHRO>). For each gene list, gene ontology annotations of mouse genes were obtained from R package. Hierarchical clustering of gene expression logarithmic fold changes between wildtype and *Wt1*<sup>het del</sup> mice was made using Manhattan distances and ward.D agglomeration method. GO enrichment of genes differentially expressed in early or late FSGS were tested against the whole gene universe. 1325 GO terms were significant after FDR correction (adjusted q value <0.1) in one

or both stages of FSGS. Next, mean logarithmic fold change (LFC) of all gene members was separately calculated for early and late FSGS for each of the 1325 GO terms. As a result, each term had 2 mean LFC values associated with it which correspond to the overall changes in early and late FSGS. Consequently, mean LFC at early FSGS was plotted against mean LFC at late FSGS for each GO term.

#### **6.2.4.8 SPIA pathway analysis**

Signaling Pathway Impact Analysis (SPIA) was done with Graphite v1.24.1 R package for KEGG and Reactome pathways. The algorithm combines 2 kinds of evidence: gene enrichment and strength of pathway perturbation in one summary statistics. Specifically, the probability of obtaining at least the observed number of genes on the given pathway just by chance ( $p_{NDE}$ ) is combined with the probability of obtaining the observed or more extreme total accumulation on the given pathway just by chance ( $p_{PERT}$ ).

#### **6.2.4.9 RNAseq and ChIPseq integration analysis**

For generation of LFC density and volcano plots, top 100 target genes of Wt1 differential binding were defined as genes with 100 highest scores from unfiltered TFTargetCaller results. Distribution of logarithmic fold changes (LFC) of the top 100 targets of Wt1 differential binding and all significant targets of wildtype Wt1 binding were plotted for both stages of FSGS. LFC distribution of all quantified genes was plotted as a background density.

For the integrative GO plot, target genes of Wt1 differential binding were functionally annotated using the GO annotation function described above. Significant (q-value <0.1) annotations were then visualized using information of differential binding and differential expression.

#### **6.2.4.10 Single-cell and bulk mRNAseq mapping**

For the alignment of bulk mRNAseq, reads were mapped to the *Mus musculus* reference genome mm10. Gene expression quantification was done using the GENCODE M12 (Ensembl 87) annotation. In brief, read 1 was defined as the first 20 base pairs spanning the cell barcodes from 1 to 12 bp and the UMI from 13 to 20 bp. The remaining 64-bp sequence was defined as read 2 leaving out the 8bp index reads. Sequencing quality was assessed by FastQC, the cell and molecular barcodes were added to the reads and barcodes with low quality bases were filtered out. The reads were then mapped to the reference genome and the multi-mapping reads were removed. Next, gene annotation tags were added to the reads using the Drop-seq toolkit 2.

#### **6.2.4.11 Clustering, t-SNE representation and marker discovery**

First, principal component analysis was performed using Seurat. The utmost principal components were used for clustering and tSNE representation. Next, the function “FindAllMarkers” in Seurat was employed to unbiasedly identify the markers per cluster.

#### **6.2.4.12 Sub-clustering and gene ontology analysis**

To identify podocyte and endothelial cell sub-clusters, both cell types were extracted from the main cluster and treated independently. The resulting digital gene expression (DGE) matrices were sent to Seurat. For the podocyte sub-clusters, stress response genes were regressed out. To identify the functional annotations associated with podocytes and endothelial cell sub-clusters, pathway and gene set overdispersion analysis (PAGODA) was employed.

## 7 Results

### 7.1 Part one: *Wt1*

#### 7.1.1 Haploinsufficiency of *Wt1* triggers no defect in the kidney development.

Mice carrying a neomycin selection cassette substituting the exon 1 + 0.5 kb of the *Wt1* sequence develops a gradual and yet slow podocyte damage marked by proteinuria and sclerotic lesions. (Kreidberg et al., 1993; Menke et al., 2003) These mice were crossed with the FVB/N breeder mice up to >20 generations to expedite the onset of the podocyte injury. (Figure 7.1-A) *Wt1*<sup>het del</sup> mice were born healthy according to the mandolin ratios and the average litter size of 9.5 known from FVB/N inbred strain. (Taketo et al., 1991) The male *Wt1*<sup>het del</sup> mice were used as the experimental mice throughout all the procedures. The mice manifested no evident developmental phenotype in the kidneys when the urine samples from P6 mice were evaluated for proteinuria using the Coomassie staining. (Figure 7.1-B) Moreover, analysis of the urinary albumin/creatinine ratios (ACR) showed that albumin excretion was not significantly different between the *Wt1*<sup>het del</sup> mice and the control littermates. (Figure 7.1-D) The kidneys displayed no size, weight, color or shape difference when comparing the *Wt1*<sup>het del</sup> with the wildtype mice. (Figure 7.1-C) In line with this, the kidney/body weight ratios were not different between the *Wt1*<sup>het del</sup> and the control mice. (Figure 7.1-E) To further investigate the impact of *Wt1* haploinsufficiency in the kidney development, kidney histology was assessed using PAS staining. The general kidney structure as well as the glomerular architecture showed normal morphology at P6 in *Wt1*<sup>het del</sup> mice and the wildtype controls. (Figure 7.1-F) Besides, no significant difference was found in the number of glomeruli between wildtype and *Wt1*<sup>het del</sup> mice at P6. (Figure 7.1-G) Altogether, no defect was identified in the kidney development of *Wt1*<sup>het del</sup> mice.

This finding is particularly important due to several key aspects: Firstly, *Wt1* is a master transcription factor with multiple functions in podocyte development, homeostasis and injury. (Hastie, 2017) Secondly, majority of the malignancies and syndromes associated with mutations in *Wt1* compromise the role of *Wt1* in development. These ailments are often represented by Glumerosclerosis besides urogenital defects and other disease phenotypes. (Baird et al., 1992; Klamt et al., 1998; Pelletier et al., 1991; Ruf et al., 2004) Thirdly, disrupted kidney development can involve initial podocyte deformity and dysfunction which can lead to Glumerosclerosis. However, the focus of this thesis is the concept of FSGS as a pathological pattern of either primary or secondary podocyte injury in which the podocyte homeostasis is perturbed. The aim is to mechanistically investigate into the pathways linked to FSGS pathology. Hence, the selected murine animal model should enable us to differentiate between an initial as opposed to a late phase of podocyte damage. The model of choice must represent a normal kidney development with no podocyte injury manifestation (e.g.: proteinuria, decreased glomerular count, aberrant glomerular histology, etc.). Yet, the podocytes should gradually start to show abnormal structural and functional features.



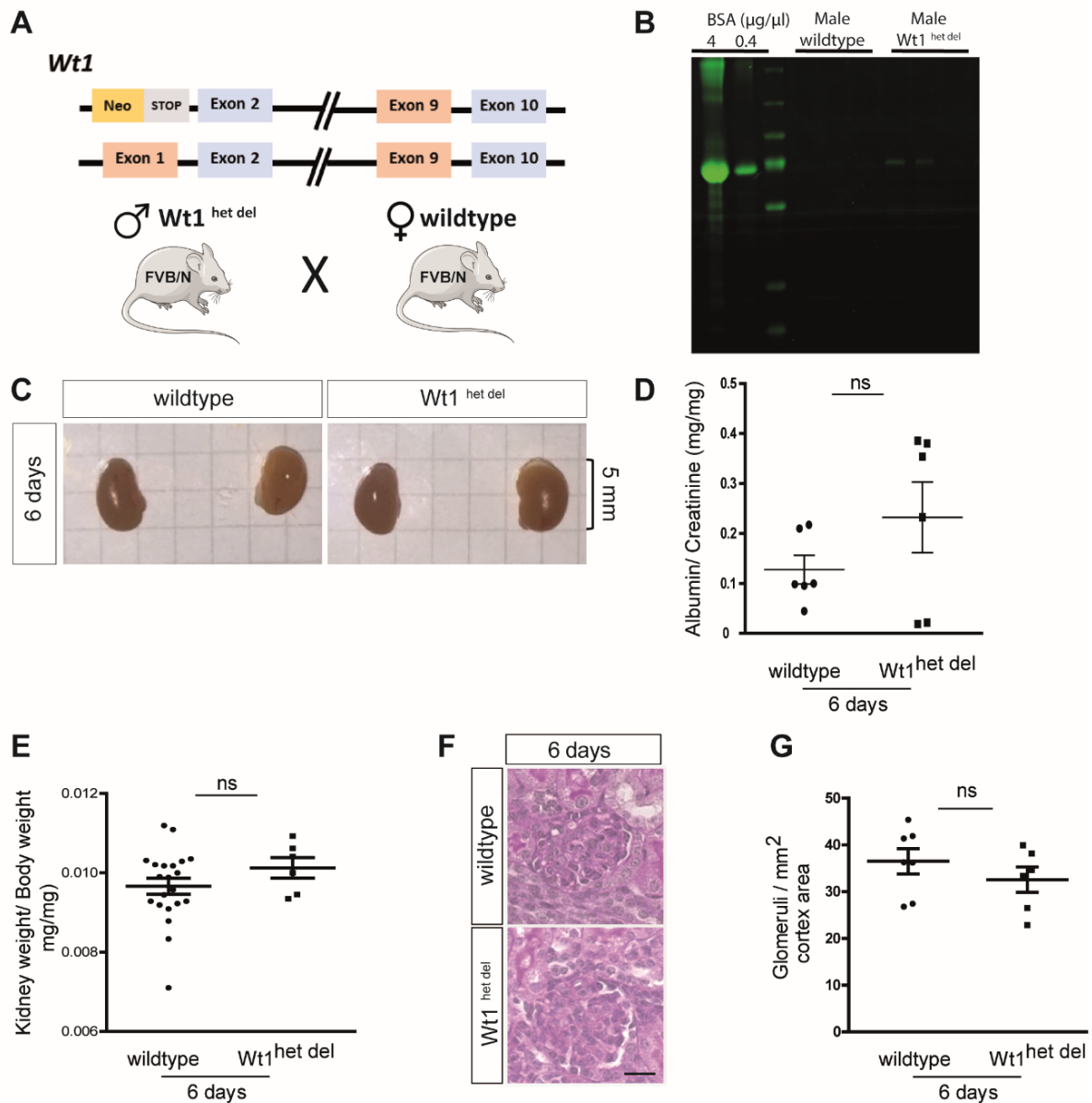


Figure 7.1: Heterozygous deletion of *Wt1* does not impose any developmental defect in mouse kidneys.

A- Schematic representation of the *Wt1*<sup>het del</sup> mouse model. *Wt1* Exon 1 and its 0.5 kb upstream is substituted with a neomycin cassette in one of the alleles. B- Coomassie staining for the urine samples of mice at postnatal day 6 (P6) shows no proteinuria in male mice under heterozygous deletion of *Wt1*. C- Images of the kidneys at P6 show no difference in size, color and morphology in mice between *Wt1*<sup>het del</sup> mice and littermate controls. D-Quantification of urinary albumin at P6 between *Wt1*<sup>het del</sup> and the control mice. ns: not significant. E- Kidneys to body weight ratios (mg/mg) of mice at P6 show no significant difference between *Wt1*<sup>het del</sup> and control mice. ns: not significant. F- PAS staining of the kidneys at P6 in both wildtype and *Wt1*<sup>het del</sup> mice. At P6, the glomeruli are completely developed, and no abnormality is detectable. Scale bar: 20  $\mu$ m. G- Analysis of the glomerular numbers in *Wt1*<sup>het del</sup> vs. control mice at P6. Glomerular counts are not significantly different in the *Wt1*<sup>het del</sup> and control mice

Majority of the existing FSGS mouse models show very severe and rapidly progressive phenotypes. Thus, they hardly allow for reasonable longitudinal investigation to differentiate between mechanisms relevant to early vs. late phase FSGS. (Fogo, 2003) To overcome this issue, *Wt1*<sup>het del</sup> model was re-investigated as an FSGS mouse model which mimics a human mutation described as causative for SRNS/FSGS. (Menke et al., 2003; Schumacher et al., 2011) In this regard, the first step was to check the gradual appearance of FSGS phenotype. Therefore, the urinary and histological assessment of the *Wt1*<sup>het del</sup> mice was performed at a rather young age (4-week-old mice) and in adulthood (12-week-old mice) and compared to the control littermates.

### **7.1.2 Heterozygous deletion of *Wt1* leads to development of FSGS.**

As previously mentioned, *Wt1*<sup>het del</sup> mice is reported to develop FSGS. (Menke et al., 2003) To confirm the contribution of *Wt1* heterozygous deletion in the development of FSGS in the new background strain and to assess the onset of phenotypes, the urine samples were examined for albuminuria using Coomassie staining and ACR analysis. *Wt1*<sup>het del</sup> mice developed a prominent and yet significant protein excretion at age 4 weeks. Albuminuria continued to exist as the mice aged. (Figure 7.2-A) ACR analysis showed significant elevation in albumin excretion in the *Wt1*<sup>het del</sup> mice. (Figure 7.2-B) Assessment of the kidneys of *Wt1*<sup>het del</sup> mice using PAS staining showed no evident sclerosis in mice at 4 weeks. However, the EM images of the kidney cortex displayed scarce ultrastructural changes at the slit diaphragm resolution. At age 12 weeks, both PAS and EM images confirm evident sclerosis marked by extensive foot processes effacement and the thickening of glomerular basement membrane. (Figure 7.2-C) Altogether, these data showed that in the *Wt1*<sup>het del</sup> mice, FSGS starts to develop as of around 4 weeks with proteinuria and no explicit sclerosis (non-sclerotic FSGS) and continues to progress to a marked sclerosis associated with proteinuria at age 12 weeks (sclerotic FSGS). In other words, podocyte damage in 4-week *Wt1*<sup>het del</sup> mice are in its early stage whereas 12-week *Wt1*<sup>het del</sup> mice manifests late stage of podocyte injury. Therefore, it is logical to expect differences in transcriptomic signature between early vs. late stage of podocyte damage. To investigate this, RNA sequencing analysis was performed in the next step.

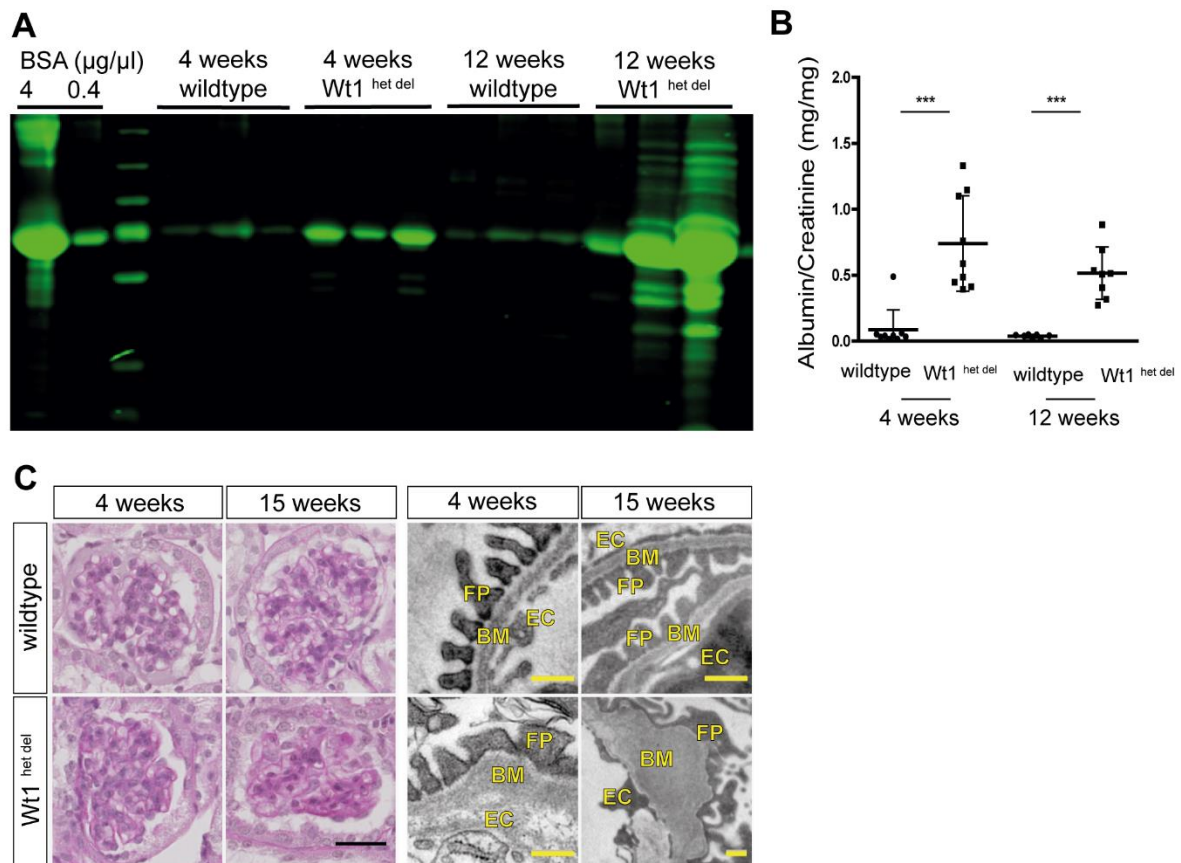


Figure 7.2: *Wt1*<sup>het del</sup> mice develops proteinuria and FSGS.

A- Coomassie staining for the urine samples from *Wt1*<sup>het del</sup> mice at 4 and 12 weeks shows mild and severe proteinuria, respectively. B- Albumin/creatinine ratios (ACR) at week 4 and 12 are significantly elevated in *Wt1*<sup>het del</sup> mice. Asterisk depicts  $p$  value is  $< 0.05$ . C- PAS staining of the kidneys at week 4 and 15 in both wildtype and *Wt1*<sup>het del</sup> mice. At week 4, there is no sign of sclerosis. At week 15, however, sclerotic lesions are apparent. Scale bar: 20  $\mu\text{m}$ . Corresponding electron microscopy images of the kidney samples at 4 vs. 15 weeks in control vs. *Wt1*<sup>het del</sup> mice. There are slight ultrastructure changes at 4 weeks whereas majority of the foot processes exhibit a normal structure. Extensive effacement of foot processes and the basement membrane thickening is evident at 15 weeks. BM: basement membrane, FP: foot processes, EC: endothelial cell. Scale bar: 500 nm

### 7.1.3 Distinct analysis modalities offer exquisite information by focusing on “Early FSGS”, “Late FSGS”, “FSGS progression” and “glomerular maturation and aging”.

RNAseq analysis of isolated mouse glomeruli was performed in *Wt1*<sup>het del</sup> mice at 4 (non-sclerotic FSGS) and 12 weeks (sclerotic FSGS) and compared with wildtype controls. As the RNAseq dataset is comprised of four groups (*Wt1*<sup>het del</sup> and wildtype, 4 weeks versus 12 weeks), the comparison modality was schemed in the first step. Figure 7.3-A shows four modes of comparison in our experimental design and the relevant MA plots depicting the differential expression for each pairwise comparison are plotted in Figure 7.3-B. Comparison of *Wt1*<sup>het del</sup> and control mice at 4 weeks and 12 weeks of age show the differential expression

of genes in early and late stage of FSGS, respectively. (termed as “Early FSGS” and “Late FSGS” hereafter). On the other hand, comparison of control mice at 4 weeks and 12 weeks of age denotes the differential expression of genes involved in “glomerular maturation and ageing”. Similarly, comparison of *Wt1*<sup>het del</sup> mice at 4 weeks and 12 weeks of age denotes the differential expression of genes involved in “FSGS progression”. At the first glance, the “FSGS progression” represents highest number of differentially expressed genes (DEGs). However, “glomerular maturation and ageing” is an inherent phenomenon even in damaging podocytes and thus, the high number of DEGs in “FSGS progression” comparison is a result of “FSGS progression added by glomerular maturation and aging”. When “glomerular maturation and aging” is factored out, there are only very few DEGs contributing to “disease progression only”. (Figure 7.3-C)

Conclusively, it is critical to mention that the comparison modality must give the most meaningful readout when collated with the bedside situation. In this regard, “glomerular maturation and aging” is not separate from “FSGS progression” in FSGS patients. Moreover, the aim in this thesis is to differentiate between the mechanisms involved in early vs. late podocyte damage. Therefore, the focus of the analysis is directed to comparing *Wt1*<sup>het del</sup> and wildtype mice at 4 weeks (“Early FSGS”) and at 12 weeks (“Late FSGS”). Nonetheless, such datasets offer a versatile analysis potential which should not be taken for granted.

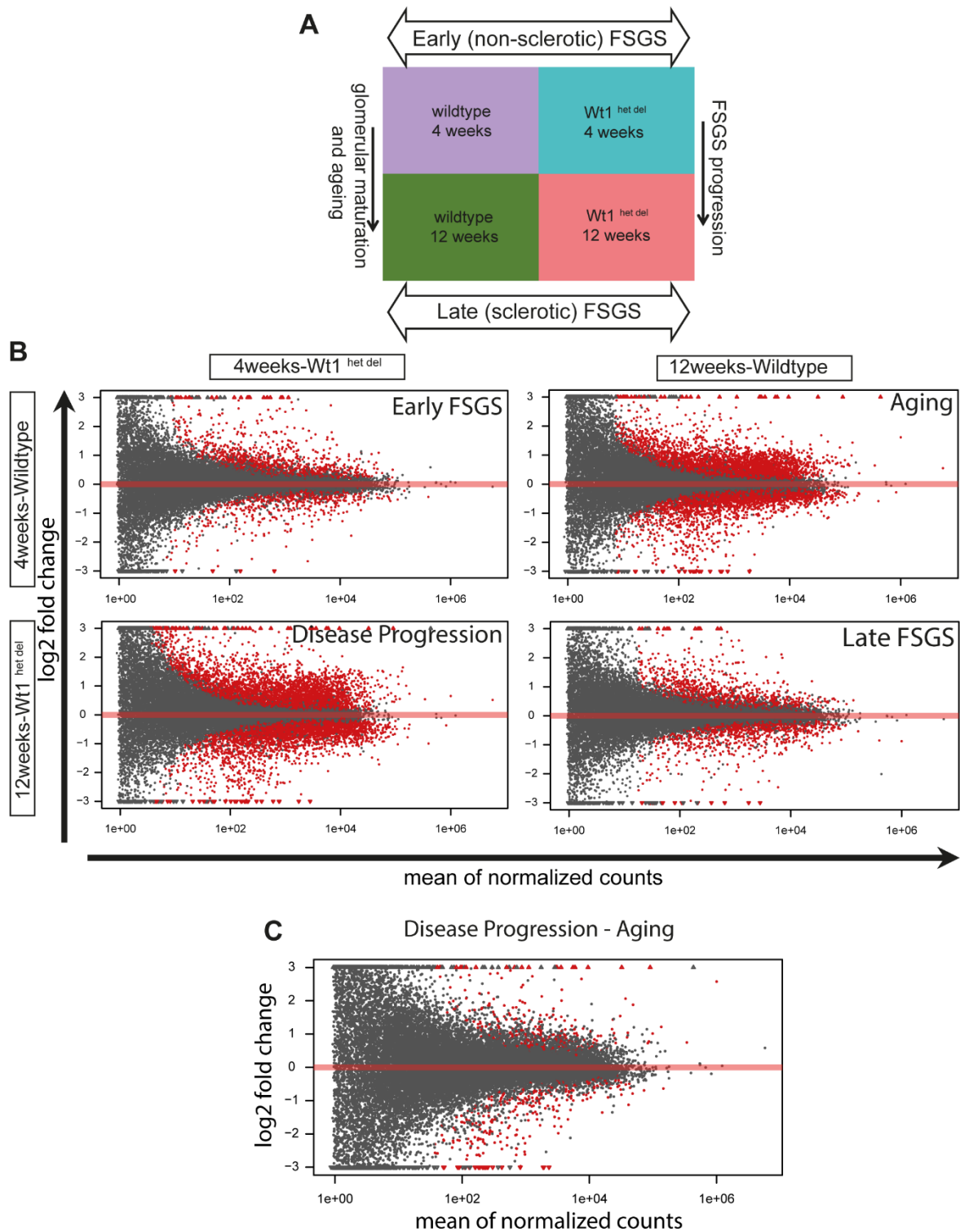


Figure 7.3: RNAseq analysis of the isolated mouse glomeruli from *Wt1*<sup>het del</sup> and wildtype mice at age 4 and 12 weeks.

A- RNAseq analysis modality. Four comparisons are represented in the scheme: early non-sclerotic and late sclerotic FSGS (thick arrows) denote the comparison between wildtype and *Wt1*<sup>het del</sup> at 4 and 12 weeks, respectively; glomerular maturation and ageing and FSGS/disease progression (narrow arrows) denote the comparison between 4 and 12 weeks in wildtype and *Wt1*<sup>het del</sup>, respectively. B- MA plot shows the relation between the mean of normalized counts (X axis) and the log<sub>2</sub> FC (Y axis) of genes, computed for four selected comparisons explained in A. The red dots represent the

significantly DEGs (FDR adjusted  $p$  values  $< 0.05$ ). C- MA plot shows the relation between the mean of normalized counts (X axis) and the  $\log_2$  FC (Y axis) of genes, computed for “disease progression” when “aging” is factored out. The red dots represent the significant DEGs (FDR adjusted  $p$  values  $< 0.05$ ).

#### **7.1.4 Haploinsufficiency of *Wt1* leads to differential regulation of genes and or pathways in podocytes.**

PCA analysis of the dataset was performed as the first-step sanity check. The analysis revealed that the biological replicates cluster according to the age and genotype as the utmost sources of variation in this context. (Figure 7.4-A) Alignment of RNAseq data to the reference genome showed that between 30-40% of reads were mapped to the intronic regions and 25-30% to the coding exonic regions. (Figure 7.4-B, C) According to literature, the changes in the intronic read counts are not merely due to the technical artefacts. In fact, they directly reflect changes in transcriptional activity. (Gaidatzis et al., 2015) Hence, both exonic and intronic reads were utilized in downstream analysis to increase the statistical power of detecting direct transcriptional changes. Differential expression analysis of genes showed that although there is a remarkable overlap between the DEGs at early and late FSGS, majority of the DEGs are specific to either early or late FSGS. (Figure 7.4-D) Hence, it is highly likely that the mechanisms involved in podocyte damage are stage-specific.

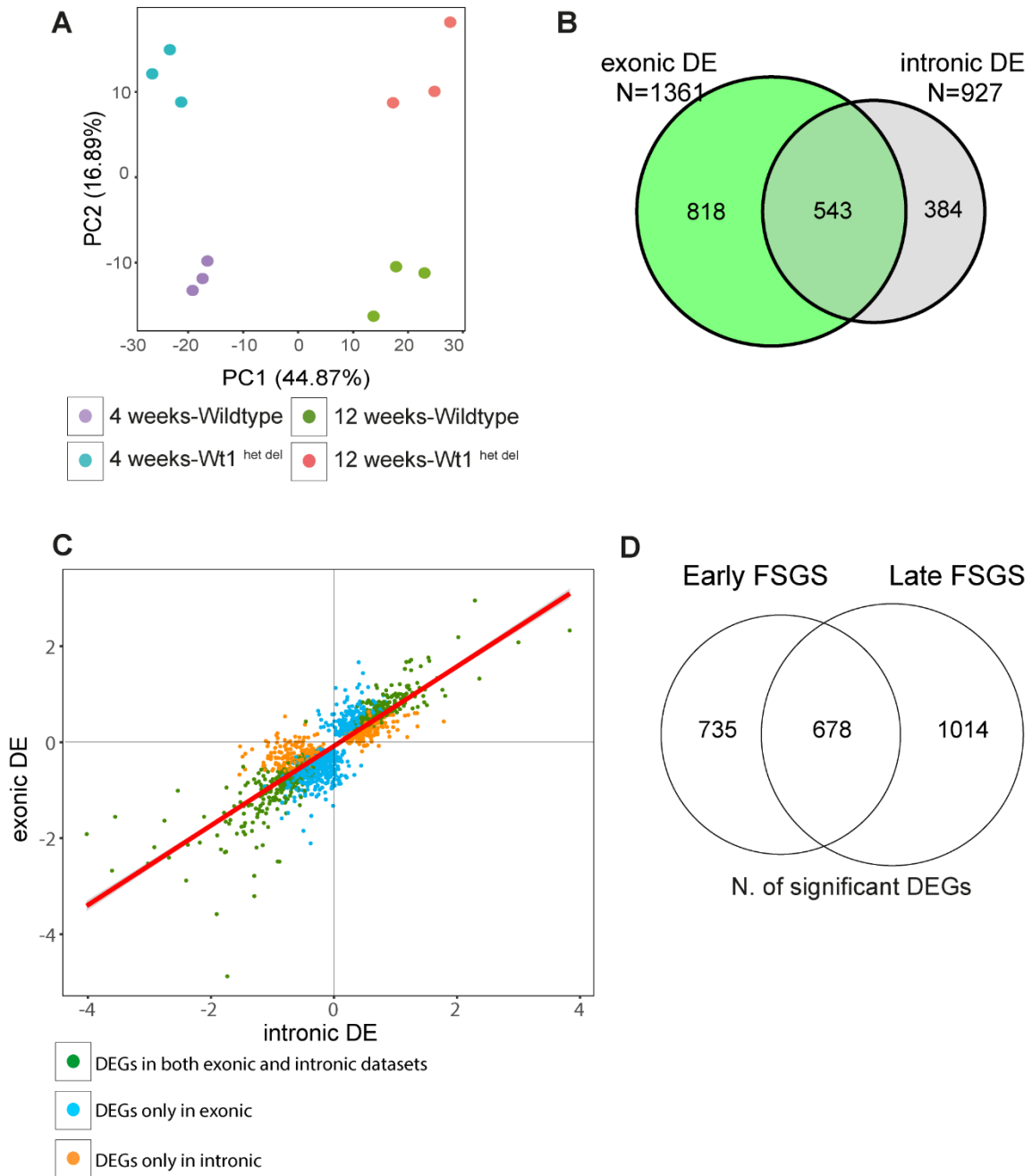


Figure 7.4: Principal component analysis (PCA) and differential expression (DE) analysis of RNAseq data.

A- The Principle Component Analysis (PCA) analysis of the RNAseq after application of removal of unwanted variation using residuals (RUVr). Principle component 1 (PC1) and 2 (PC2) represent age and genotype, respectively; percentages show the amount of variation explained by each principal component. Each dot represents one biological replicate. B- Venn diagram shows overlap of significant DEGs in exonic and intronic datasets. C- 2-D plot shows LFC values from DE analysis on exonic vs. intronic reads. The relationship between logarithmic fold changes in exonic and intronic datasets. Pearson’s correlation coefficient: 0.84, colored by adjusted  $p$  value. D- Venn diagram shows the intersect between genes significantly differentially expressed (FDR adjusted  $p$  values  $< 0.05$ ) at early and late FSGS. Differential expression was computed using DEseq2.

Expectedly, GO term analysis showed the same trend, i.e.: there were some GO terms enriched either at early or at late FSGS and some others were enriched both at early and late FSGS. (Figure 7.5) The GO terms involved only in early FSGS probably reflect the events ensuing haploinsufficiency of *Wt1* whereas the GO terms involved in late FSGS can reflect the inflammation and sclerosis during progressed podocyte damage. Similarly, the terms which are enriched both at early and late FSGS may denote the events generally happening during the podocyte damage. Expectedly, majority of the annotated GO terms were previously established as the key podocyte functions. There are solid pieces of evidence from literature suggesting the relevance of actin cytoskeleton homeostasis, cell adhesion, collagen biology, Ephrin signaling pathway, etc. in podocyte biology all of which have been found in our GO analysis. (Lennon et al., 2014; Sever and Schiffer, 2018; Weiss and Kispert, 2016)

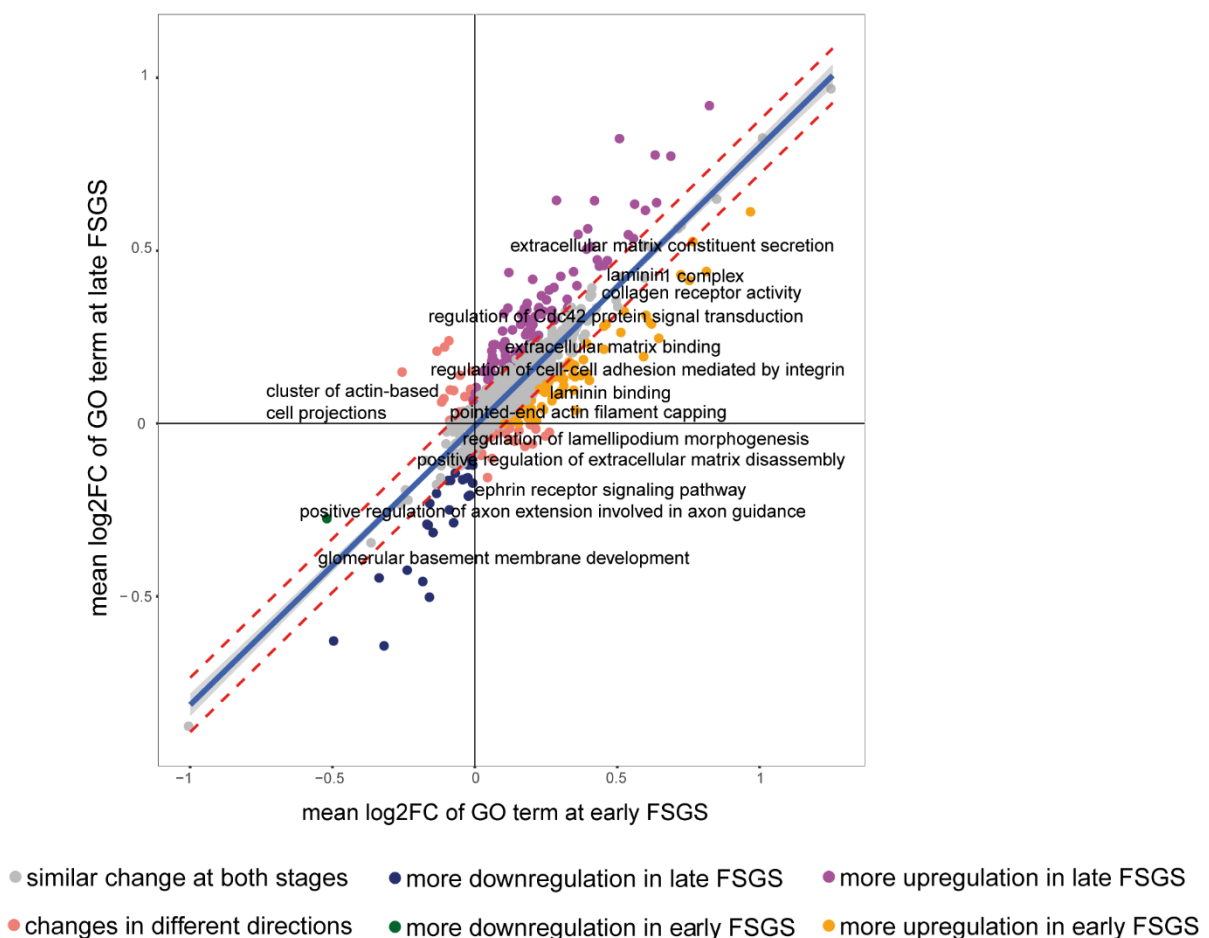


Figure 7.5: Functional annotation of DEGs at early and late FSGS.

GO term plot depicting significant functional annotations of the DEGs in early and/or late FSGS. Each circle represents one GO term. X and Y axis represent mean log<sub>2</sub>FC of gene expression for the enriched GO terms in early and late FSGS, respectively. The blue line depicts the regression line and the red dash line defines the 95% prediction interval (PI). The terms located outside the PI have greater expression change of the contributing genes in early or in late FSGS.



One general limitation in the GO term analysis is that it is restricted to the DEGs and the network-based regulatory interactions are not considered. Hence, a network-based pathway analysis approach was employed to overcome this limitation. Signaling Pathway Impact Analysis (SPIA) is based on DEGs and the interaction between the genes in the relevant context. (Tarca et al., 2009)

Essentially, SPIA uses two types of evidence to perform the pathway ranking:

- 1-  $p_{NDE}$  is defined as the probability of obtaining the observed number of genes (NDE) on the given pathway just by chance.
- 2-  $p_{PERT}$  corresponds to the probability of obtaining the observed perturbation on the given pathway just by chance.

SPIA analysis offered a more in-detail and yet podocyte-specific insight on the pathways differentially regulated during the development of FSGS in the *Wt1*<sup>het del</sup> mice. Again, some pathways were found to be perturbed only either at early or late FSGS and some other pathways were perturbed both at early and late FSGS. (Figure 7.6)

Differential pathway regulation during the development of FSGS, fueled the speculation on *Wt1* differential regulatory activity on the genome. Therefore, ChIPseq analysis of *Wt1* was performed at non-sclerotic stage of FSGS (i.e.: at 4 weeks) to target potential transcriptional re-programming at the beginning of the disease.



Figure 7.6: Results of the Signaling Pathway Impact Analysis (SPIA) of DEGs at early and late FSGS using KEGG and REACTOME databases.

Global adjusted  $p$ -values ( $p_{GFDR}$ ) from SPIA statistics were  $\log_{10}$  transformed and resulted values for inhibited pathways were multiplied by -1 to reflect “repression” as opposed to “activation” of the pathways. Some pathways are perturbed exclusively at early or late FSGS whereas some other pathways are perturbed both at early and late FSGS.

### 7.1.5 Differential binding of Wt1 on the regulatory regions suggests transcriptional reprogramming at early disease stage.

To further study if the differential gene and pathway regulation is a trail of an early reprogramming event under the *Wt1*<sup>het del</sup> condition, Wt1 ChIPseq analysis was performed in 4-week *Wt1*<sup>het del</sup> and wildtype mice. Different ChIPseq quality metrics were employed to assess the quality of Wt1 ChIPseq dataset according to the ENCODE guidelines. (Landt et al., 2012)

The consistency between the relevant biological replicates was evaluated using IDR analysis. (Figure 7.7-A) Majority of the signal from the samples was at the threshold  $\leq 0.01$  substantiating the high quality of the Wt1ChIPseq dataset. To further assess the dataset quality, peak conservation score and *de novo* motif enrichment score were calculated for the merged peak summits and compared to the wildtype. (Figure 7.7-B, C) The quality of this dataset was approved again as the plots demonstrate sharp peaks at the center. Finally, the correlation heatmap of the ChIPseq normalized reads depicted that the samples are clustered according to the genotype. (Figure 7.7-D) Altogether, the quality of the ChIPseq dataset was high and the next analysis steps could be done on this dataset.

Next, Wt1 peak distribution was assessed across the whole genome in *Wt1*<sup>het del</sup> and wildtype samples. Majority of the peaks were concentrated remotely from the TSS. (Figure 7.7-E) This was in line with what was found previously on the binding affinity of Wt1 on different regulatory elements. (Kann et al., 2015)

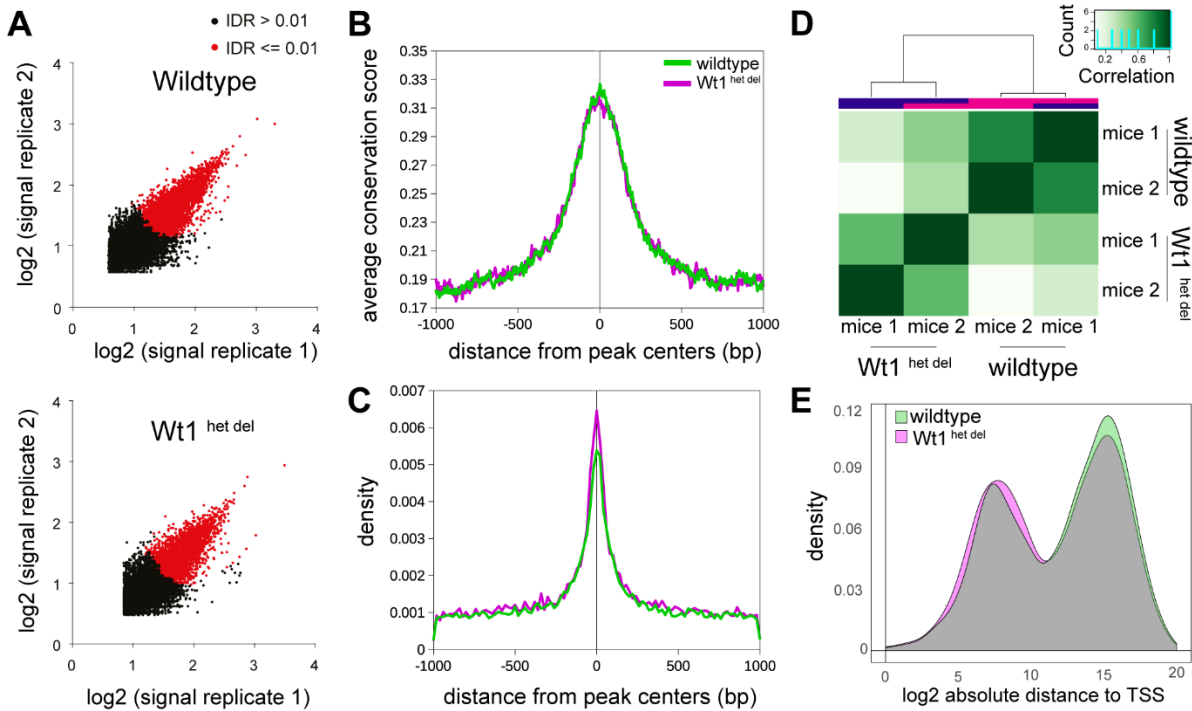


Figure 7.7: Wt1ChIPseq at non-sclerotic stage of FSGS (4 weeks) compared to the wildtype mice.

A- Irreproducibility Discovery Rate (IDR) analysis shows reproducibility of ChIPseq peaks of the relevant biological replicates for wildtype (upper panel) and *Wt1*<sup>het del</sup> (lower panel). Each dot represents a peak: red dots correspond to genuine peaks at IDR ≤ 0.01. The axes show the log<sub>2</sub> transformed signals for each replicate. B, C- Metagene plots for consensus Wt1 ChIPseq peaks in wildtype (green) and *Wt1*<sup>het del</sup> (magenta). The upper panel shows the nucleotide conservation around the peaks center where the nucleotide conservation is represented by mm10 phastCons 60-way scores. The lower panel shows the primary motif density around the peaks center. D- Correlation heatmap of Wt1ChIPseq samples based on normalized read counts. It shows samples are clustered according to the genotype as the key source of variance. E- Density plot showing the distribution of distances between consensus Wt1ChIPseq and the nearest transcription start site for peaks in wildtype (green) or *Wt1*<sup>het del</sup> (magenta). The density distribution is bimodal reflecting preferential binding at distant *cis* regulatory regions.

Ultimately, differential binding analysis enabled identification of >600 regions significant at FDR < 0.05. Not surprisingly, majority of the differentially bound (DB) regions were less bound in *Wt1*<sup>het del</sup> mice. (Figure 7.8-A) Taking a closer look at the certain target gene levels such as *Actn1*, *Efnb1* and *Col4a3* and 4 validated differential binding under het del condition. (Figure 7.8-B)

Taken together, these results show that haploinsufficiency of *Wt1* primes re-programming events in earlier disease stages resulting in differential pathway regulation and the subsequent disease progression.

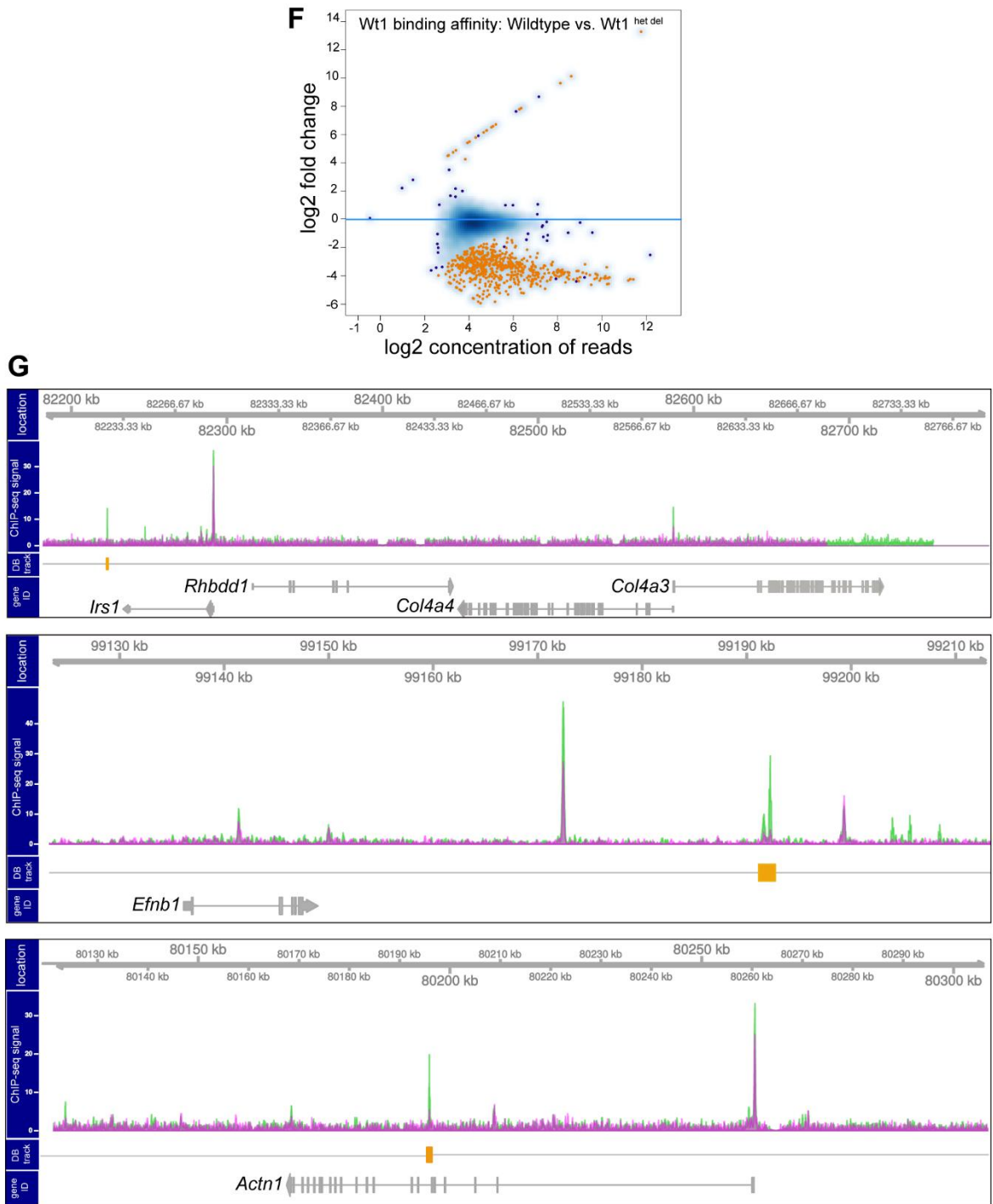


Figure 7.8: Differential binding analysis of *Wt1*-bound loci in *Wt1*<sup>het del</sup> and control mice at 4 weeks.

A- MA plot showing the results of the differential binding (DB) analysis. Each point represents a binding site, with points in orange representing sites identified as differentially bound at FDR < 5%. Majority of the DB regions are less bound under *Wt1*<sup>het del</sup> condition. B- Genome browser plots for *Wt1* target genes (*Actn1*, *Efnbb1* and *Col4a3/Col4a4*) show decreased *Wt1* ChIPseq signal (normalized to Input) in *Wt1*<sup>het del</sup> mice (magenta) compared to wildtype (green). The DB track shows the location of the DB regions (orange). The annotation track shows the gene level annotation of mouse genome from Ensembl Release 96 (April 2019).

### 7.1.6 Integrative analysis of binding and expression

In order to pinpoint the key biological phenomenon underlying the development of FSGS in this study, the target genes of the Wt1 differential binding were predicted and the top 100 genes were used to be assessed in terms of expression properties at early and late FSGS. For this purpose, log<sub>2</sub> fold change of differential expression for these genes was plotted against the q value of their expression level. (Figure 7.9)

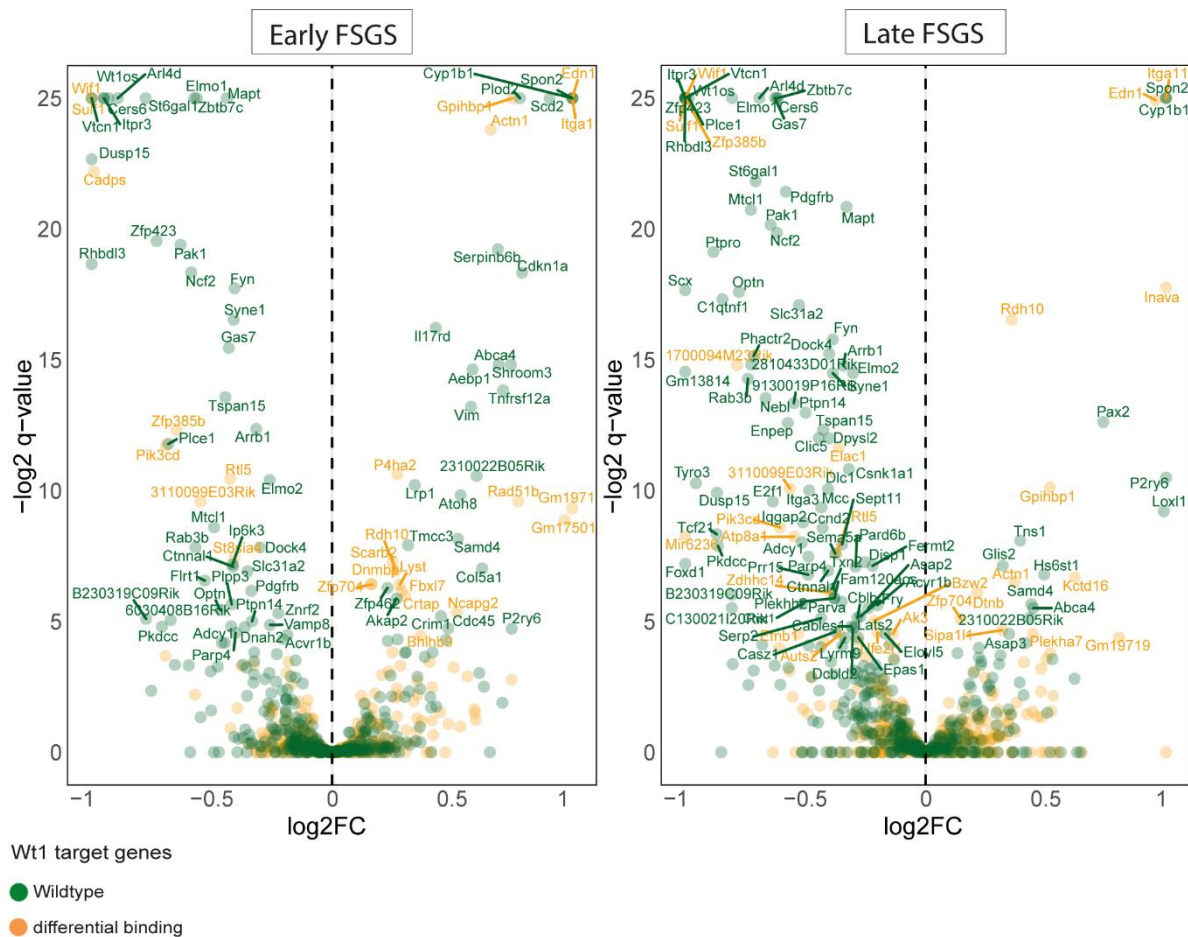


Figure 7.9: Volcano plot representing the targets of Wt1 differential binding (orange) and Wt1 binding in control condition (dark green) at early and late FSGS.

Y axis shows the  $-\log_2 q$  value of expression and is limited to 25 while the X axis shows the log<sub>2</sub> fold change which is limited between -1 and 1. All points outside of the axis limits are plotted on borders. Expectedly, majority of DB genes have downregulated in late FSGS whereas in early FSGS, the total expression behavior of target genes has not markedly changed. Another representation of the volcano plots showed the same readout when plotting the log<sub>2</sub>FC of DEGs using the two aforementioned gene groups and all target genes as the background. (Figure 7.10)

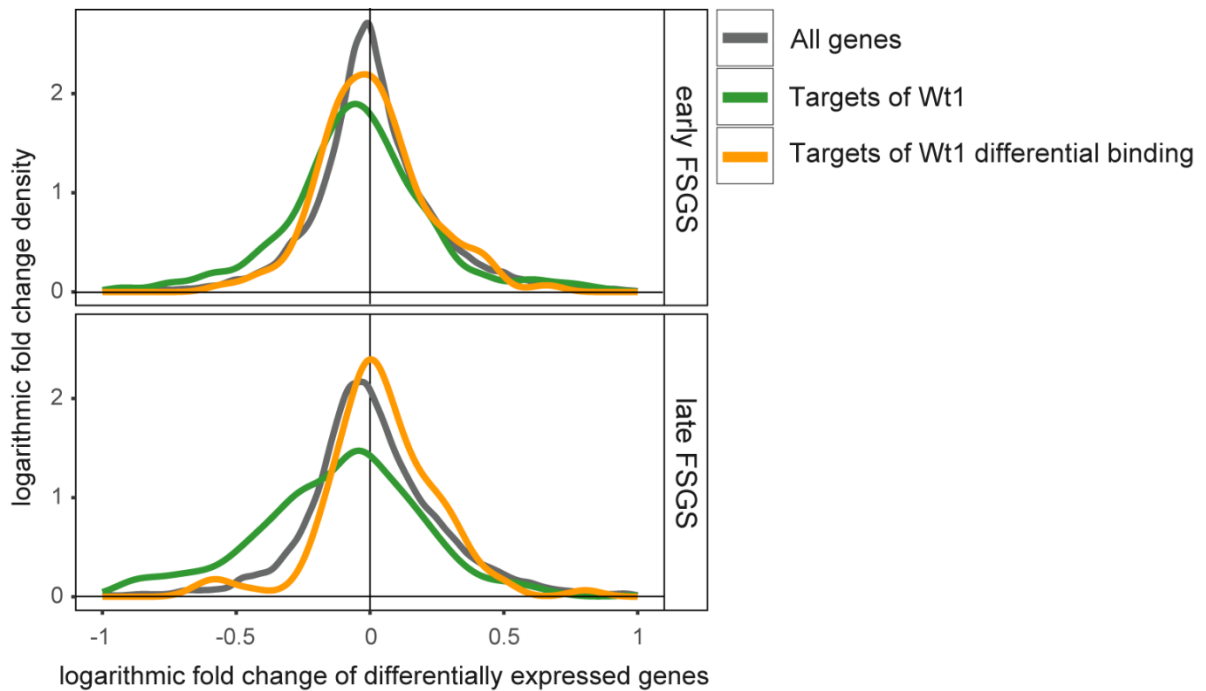


Figure 7.10: LFC-density plot of differentially bound genes for early and late FSGS.

LFC-density plots of top 100 DB (orange) and wildtype (green) Wt1 target genes at early (top panel) and late (bottom panel) FSGS. Both plots show that LFC distributions are different from that of the background for the aforementioned groups of target genes. The comparison of the plots for both groups of target genes highlights the shift in the LFC distribution between the early and late FSGS.

The power of integrative computational analysis to infer the gene regulatory functions is way more robust than genome-wide profiling of TFs or gene expression alone. (Jiang and Mortazavi, 2018) Therefore, the next intriguing step was to functionally analyze the ChIPseq and RNAseq integration. For this purpose, target genes of Wt1 differential binding were functionally annotated and the significant annotations were derived using differential binding and differential expression of the target genes. The results of functional analysis were stimulating since “Collagne Binding” and “Ephrin Signaling” were enriched. (Figure 7.11) These functions were already found in the GO term enrichment analysis as well as pathway enrichment analysis of the RNAseq data. Therefore, they were further investigated in the context of FSGS using immunofluorescent imaging.

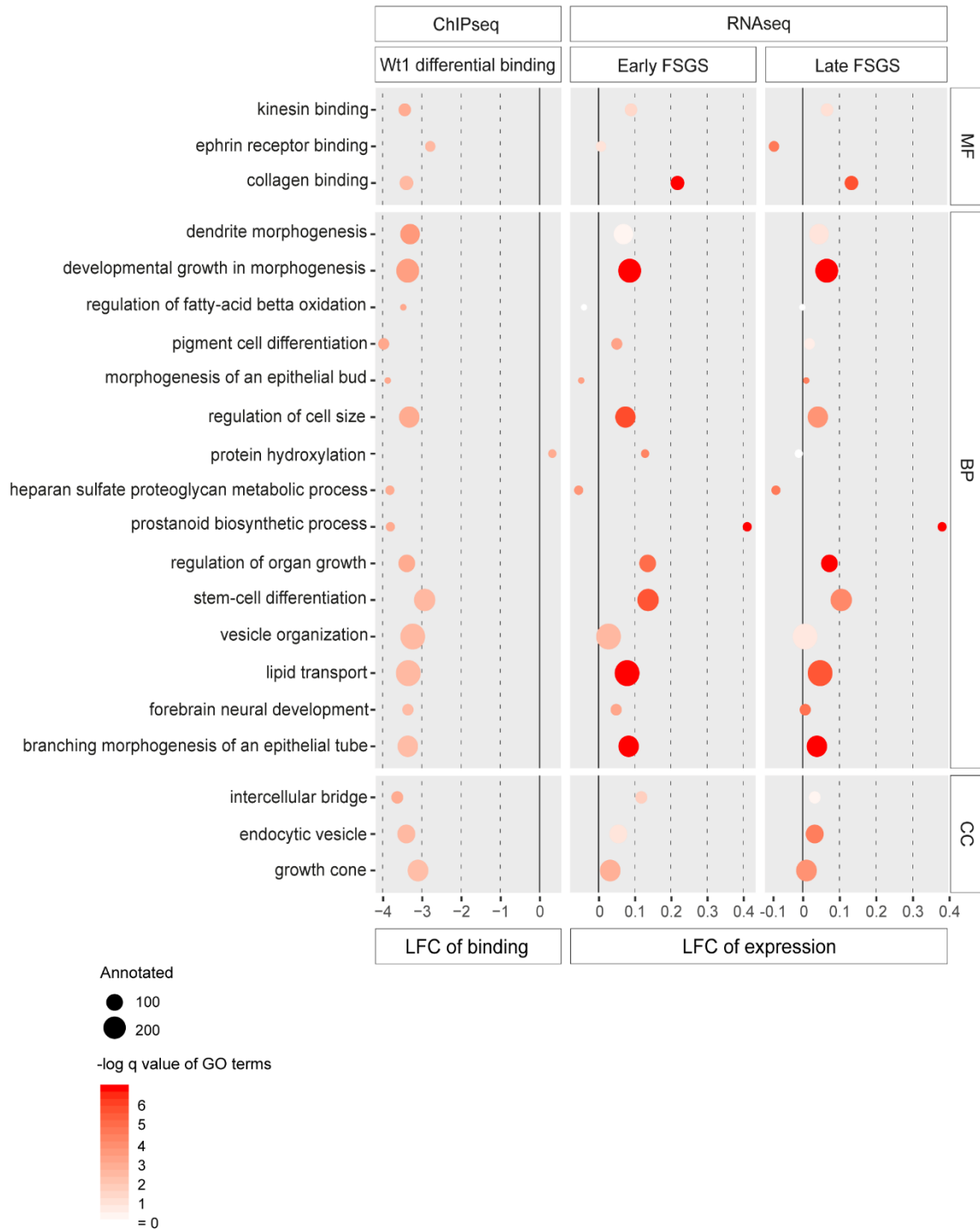


Figure 7.11: Integration of RNAseq and ChIPseq highlights key GO annotations contributing to the early and late FSGS.

ChIPseq-RNAseq integration plot showing the LFC of binding and expression at early and late FSGS (X axis) for GO terms enriched in the DB genes. The color intensity of circle is proportional to the significance of GO term (-log<sub>2</sub> of q-value) in the respective dataset. The size of circle is proportional to the size of the term (number of annotated genes). The GO terms are grouped by three categories: biological processes (BP), cellular components (CC) and molecular functions (MF). Selected terms are shown.



### 7.1.7 Collagen biology is disturbed as FSGS develops.

The glomerular basement membrane is a dense network composed of collagens, laminins, proteases, growth factors, heparan sulfate proteoglycans and other structural proteins. (Lennon et al., 2014) Among all the GBM constituents, collagens play a key role in providing a foundation for other structural molecules. In *Wt1<sup>het del</sup>* and control mice, 22 subtypes out of 28 known collagens are expressed at 4 and 12 weeks. (Figure 7.12)

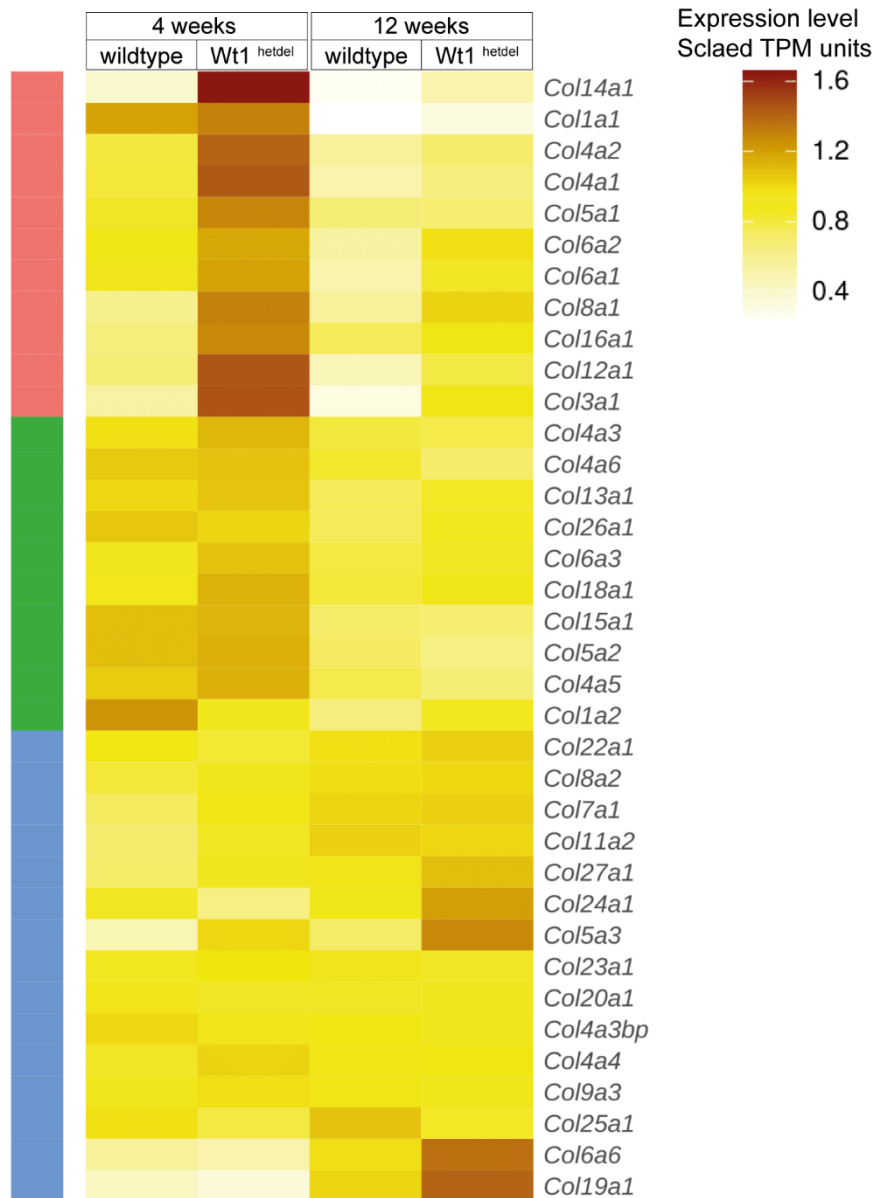


Figure 7.12: Heatmap depicts the expression values of collagen subtypes in *Wt1<sup>het del</sup>* and control mice at 4 and 12 weeks.

Only genes with a certain average expression across all replicates (> 0.5 Transcripts Per Million; TPM) are shown. This criterion does not exclude any significantly DE genes.



Genes contributing to collagen-related GO terms included the core components of the GBM and exhibited a significant differential expression in the course of FSGS (both at 4 and 12 weeks). (Figure 7.13)

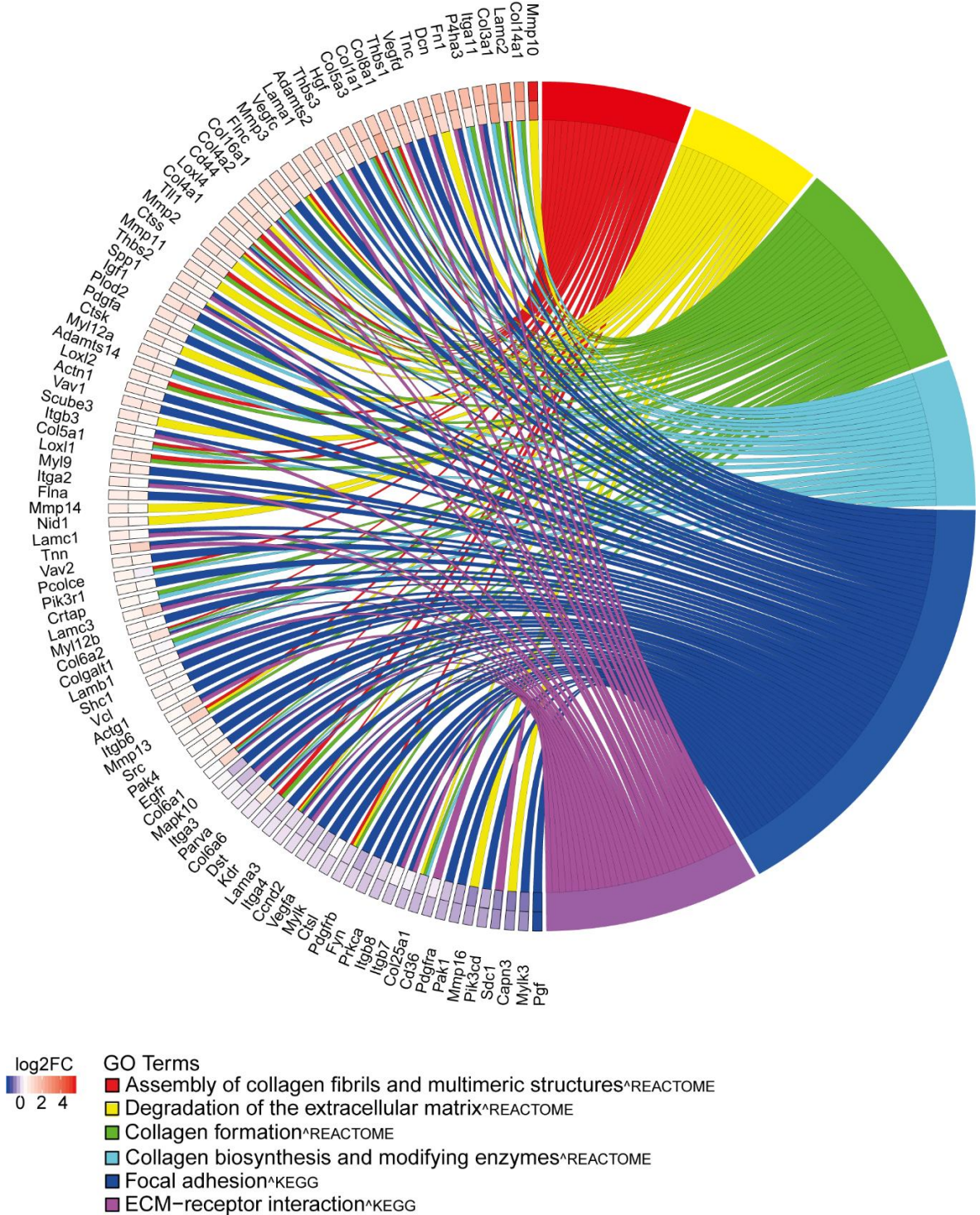


Figure 7.13: Chord plot for Collagen Biology.

Represented GO terms are relevant to collagen biology and their contributing DEGs at 4 and 12 weeks are shown. Only log2 transformed fold changes of the DEGS significant for both ages are depicted.

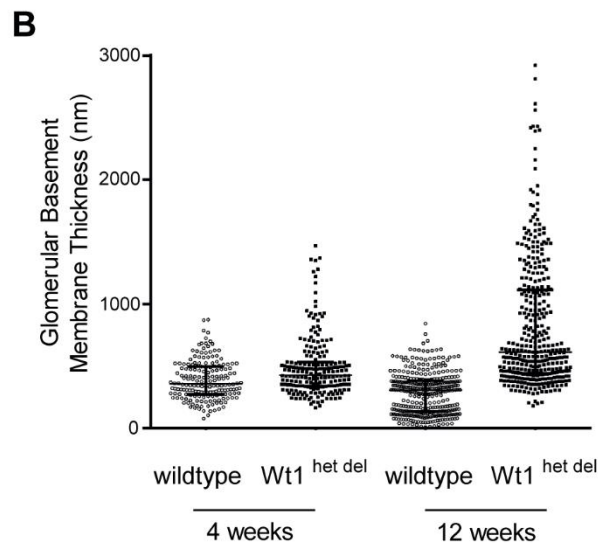
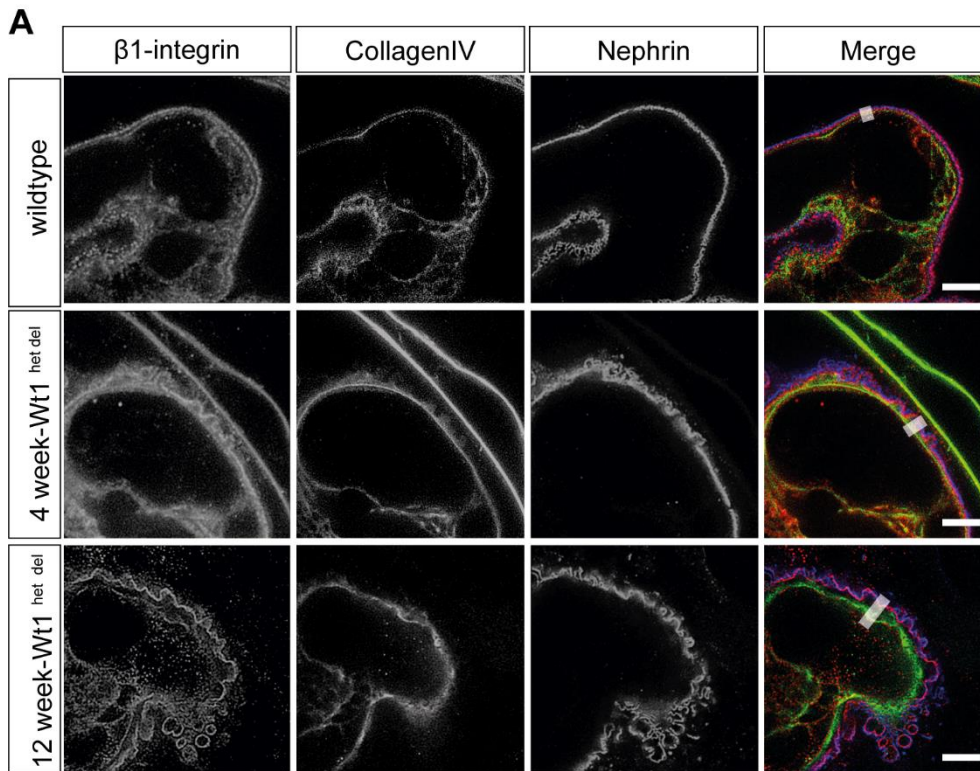


Figure 7.14: Immunofluorescence staining of GBM components and evaluation of GBM thickness.

A-Immunofluorescent staining for collagen IV,  $\beta$ 1-integrin and nephrin in *Wt1*<sup>het del</sup> and wildtype mice at weeks 4 and 12. STED images reflect the comparison between the wildtype and *Wt1*<sup>het del</sup> mice at early and late FSGS. Appearance of hummocks along the glomerular basement membrane (GBM) as well as GBM thickening is visible less at early and more at late FSGS. (yellow arrows) The GBM expansion is increasing as the disease progresses (late FSGS). Scale bar: 2  $\mu$ m. Image adapted and modified from (Jess, 2019) B- Quantification of the GBM thickness using the  $\beta$ 1-integrin signal from the podocyte and the endothelial cell shows a marked increase in GBM thickness at early and late FSGS. The plot depicts median  $\pm$  95% of the confidence interval (CI).

In line with the transcriptomic analysis, immunofluorescence staining of nephrin,  $\beta$ 1-integrin and collagen IV is suggestive of distorted GBM components especially Collagen IV. STED

images showed appearance of hummocks along the slit diaphragm in *Wt1<sup>het del</sup>* mice both at non-sclerotic and sclerotic stage of FSGS. (Figure 7.14-A) This phenomenon is accompanied by the contorted expression of the collagen IV subtypes in the areas where the GBM is visibly thickened. Using  $\beta$ 1-integrin signal from the podocytes and endothelial cells, the GBM thickness was quantified at 4 and 12 weeks in *Wt1<sup>het del</sup>* and wildtype mice. A marked increase in the GBM thickness is evident in the *Wt1<sup>het del</sup>* mice during the progression of FSGS. (Figure 7.14-B)

### **7.1.8 Ephrin signaling pathway is progressively impaired in the course of FSGS.**

Eph-Ephrin signaling is the largest kinase pathway which is under-investigated in the context of podocyte biology. The signaling cascade is routinely initiated upon receptor-ligand binding. (Lisabeth et al., 2013) Go term analysis of our RNAseq data showed that majority of the contributing genes to the “Ephrin signaling” GO term have undergone significant up/down regulation. (Figure 7.15-A) In a separate study, our single cell RNA sequencing revealed EphrinB1 and its receptor EphB1 have the highest expression among all other Ephrins and Ephs, respectively. (Figure 7.15-B) (Karaikos et al., 2018)



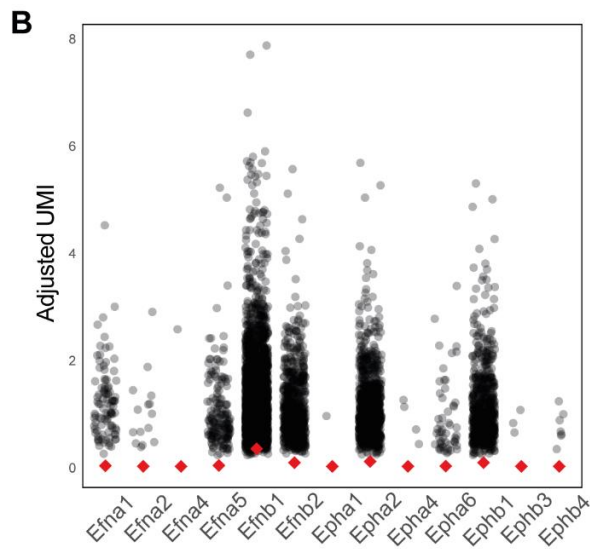
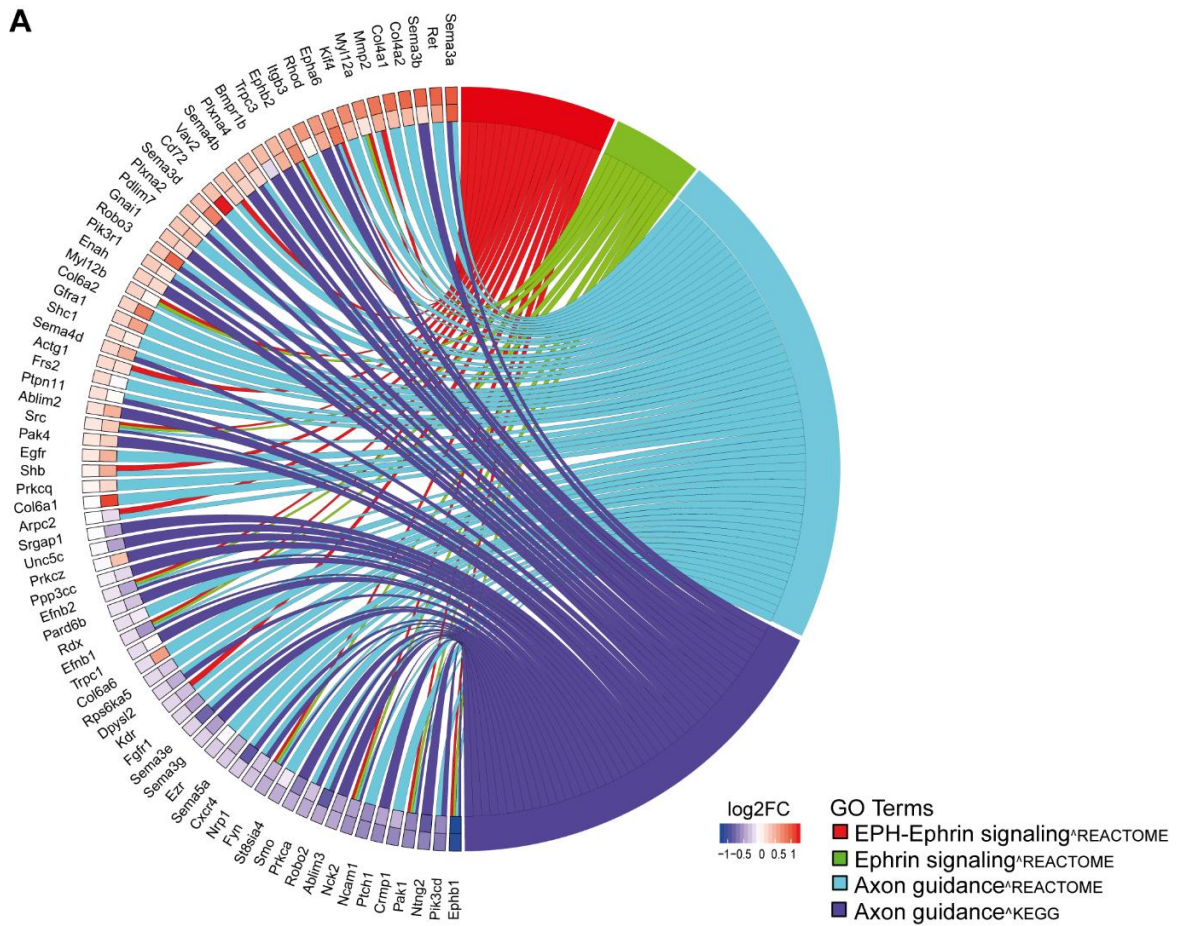


Figure 7.15: DEGs contributing to Ephrin Signaling and podocyte-specific expression values of the Ephs and Ephrins.

A- Chord plot for ephrin signaling. Represented GO terms are relevant to ephrin signaling and their contributing DEGs at 4 and 12 weeks are shown. Only log<sub>2</sub> transformed fold changes of the DEGS significant for both ages are depicted. B- Density plot represents the expression values of Eph receptors and Ephrin ligands in the podocytes of CD1 male mice. The Y axis shows the expression values shown by adjusted UMIs (unique molecule identifiers). Data adopted from (Karaiskos et al., 2018)

EphrinB1 is located at the slit diaphragm and it contributes to actin cytoskeleton remodeling via triggering an intracellular phosphorylation cascade which leads to increased podocyte motility and detachment. (Hashimoto et al., 2007) In *Wt1*<sup>het del</sup> mice, the non-sclerotic FSGS (4 weeks) reflects only minor alterations in the glomerular architecture. Hence, any change at the protein level can be detected at progressed disease stage i.e. in late FSGS (12 weeks). Using a targeted mass spectrometry approach, EphrinB1 reduction was approved at 12 weeks. (Figure 7.16-A) However, this reduction was not significant which, *per se*, substantiated our speculation on the dependence of the EphrinB1 reduction to the extent of sclerosis at certain loci of the kidney. Therefore, EphrinB1 and EphB1 proteins were stained in 12-week mice using the optical clearing technique and images were taken across the kidney sections in order to have an overview on more damaged glomeruli. Not surprisingly, both EphrinB1 and EphB1 showed a strong decrease in sclerotic areas in 12-week *Wt1*<sup>het del</sup> mice when compared to controls. (Figure 7.16-B)

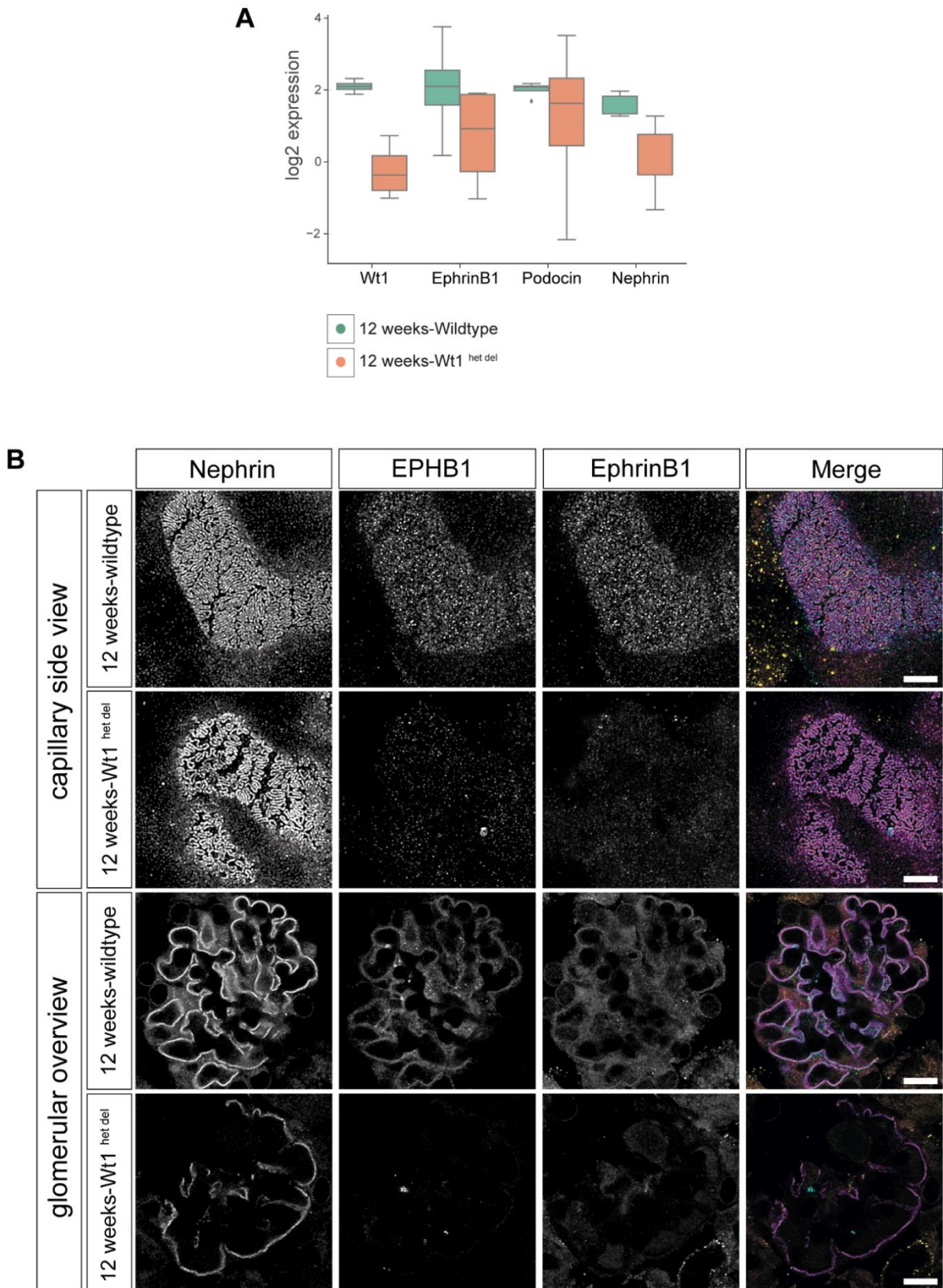


Figure 7.16: Assessment of EphrinB1 and EphB1 protein expression in late FSGS.

A- Targeted proteomics on the isolated glomeruli of *Wt1<sup>het del</sup>* and wildtype mice at 12 weeks. *Wt1*, *NPHS1*, *NPHS2* are also included for normalization. EphrinB1 protein level is decreased when the sclerosis is explicit at 12 weeks when its abundance is normalized to the housekeeping and tubular

proteins. B- Immunofluorescent staining for nephrin (magenta), EphB1 (yellow) and EphrinB1 (blue) in *Wt1<sup>het del</sup>* and wildtype mice at 12 weeks. The two upper panels depict the capillary side view (scale bar: 3  $\mu$ m) whereas the lower two panels depict the glomerular overview (scale bar: 15  $\mu$ m). Marked reduction of nephrin, EphB1 and EphrinB1 is visible in glomeruli affected by FSGS. EphB1 and EphrinB1 signals show a dotted pattern covering the capillary area. In *Wt1<sup>het del</sup>* mice, loss of nephrin signal is evident at sclerotic loci. EphB1 and EphrinB1 co-disappear with the nephrin signal.

Since EphrinB1 showed the highest expression level among the Eph receptors and the Ephrin ligands, it was tempting to perform EphrinB1 staining and quantify its intensity according to the disease progression. EphrinB1 was stained in 12-week mice together with podocin using the same staining technique. (Figure 7.17-A) In *Wt1<sup>het del</sup>* mice, EphrinB1 mean intensity showed a significant reduction when it was normalized to podocin signal within the capillary area. (Figure 7.17-B)

Our colleagues have recently found that the slit diaphragm (SD) length decreases significantly in sclerotic glomeruli in the course of FSGS. (unpublished data) Acknowledging this, SD Length/Capillary Area was employed as a measure of disease progression. In line with what our colleagues have shown, a marked decrease in SD Length/Capillary Area was measured in sclerotic mice (progressed disease). (Figure 7.17-C) To answer if the EphrinB1 intensity reduction is dependent on the extent to which the disease has progressed, the correlation between the SD Length/Capillary Area (disease progression) and the EphrinB1 mean intensity normalized to podocin mean intensity was assessed. A strong correlation was detected using the Spearman correlation test (correlation coefficient = 0.81). (Figure 7.17-D) Conclusively, this correlation suggests that EphrinB1 expression is adversely affected by the disease magnitude.



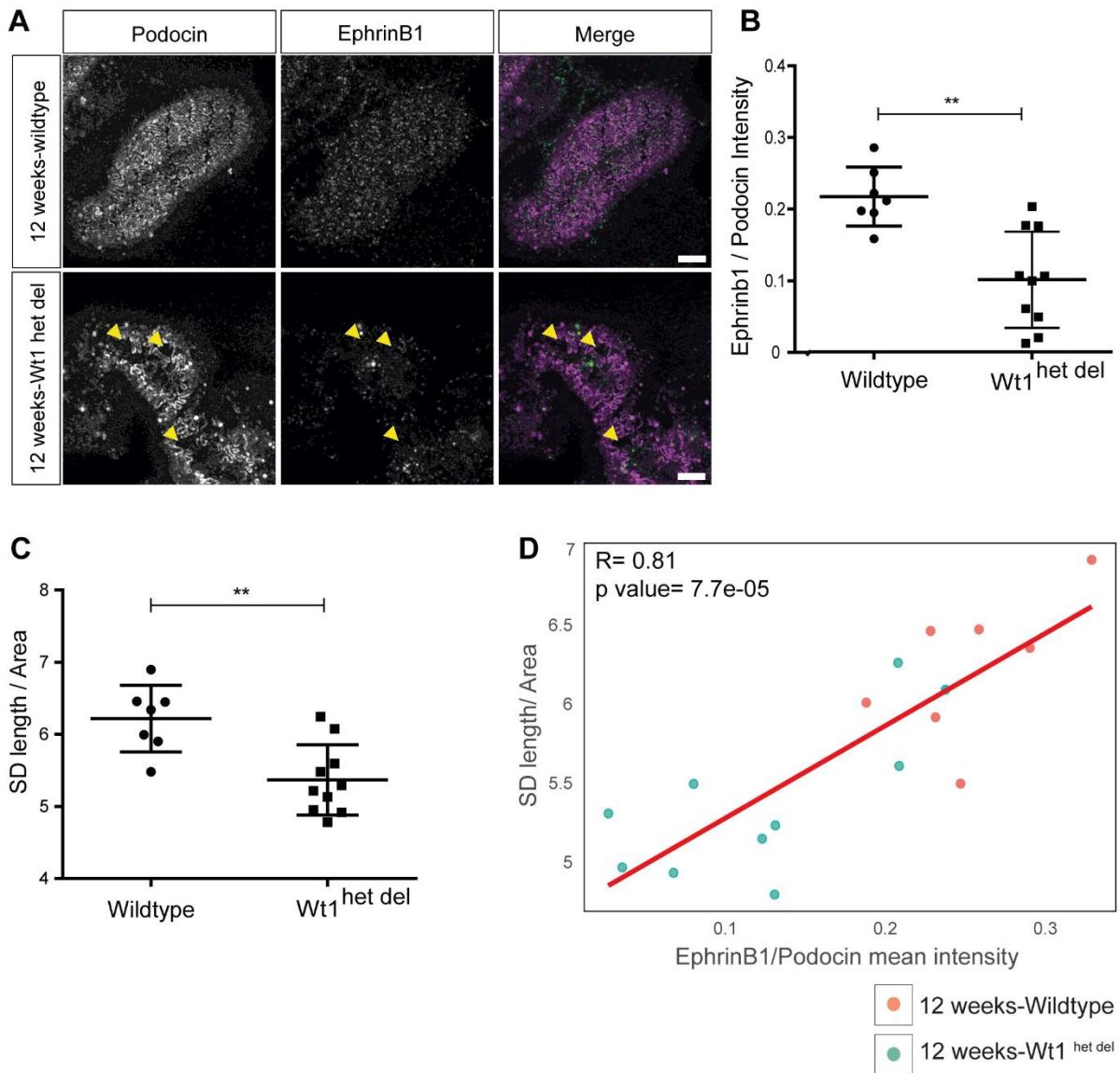


Figure 7.17: EphrinB1 progressively reduces in the course of FSGS.

A- Immunofluorescent staining for podocin and EphrinB1 in *Wt1<sup>het del</sup>* and wildtype mice at 12 weeks. Images show the *en face* view of adjacent podocyte foot processes. In wildtype mice, podocin signal (magenta) shows the interdigitated foot processes with a normal structure. EphrinB1 signal (green) shows a dotted pattern covering the podocin-positive area. In *Wt1<sup>het del</sup>* mice, however, loss of podocin signal is evident at sclerotic loci at 12 weeks (yellow arrows). EphrinB1 co-disappears with the podocin signal. Scale bar: 3  $\mu$ m. B- Dot plot shows a significant reduction in EphrinB1 mean intensity as normalized to podocin signal intensity in *Wt1<sup>het del</sup>* mice. (*p* value: 0.0011) C- Dot plot shows the SD length/Area in *Wt1<sup>het del</sup>* and control mice at 12 weeks. SD length/Area is used as a measure of disease progression. SD length/Area is significantly less in progressed disease (12-week het del mice) when compared to the control mice. (*p* value: 0.0026) D- Evaluation of correlation between EphrinB1/Podocin signal and the disease progression. Disease progression is measured by SD length/ Area. Spearman correlation test suggests a strong correlation between disease progression and the EphrinB1/Podocin signal (*p* value: 7.7E-05). Each dot represents the SD length per area and the contributing EphrinB1/Podocin mean intensity ratio within the area. The red line represents the correlation coefficient (0.81).



## 7.2 Part two: Tead1

### 7.2.1 In wildtype mouse glomeruli, Tead1 is the effector of Hippo signaling pathway.

The TEA domain (TEAD) transcription factors have four highly conserved subtypes in mammals with different levels of tissue expression. (Gibault et al., 2018) Our single cell RNAseq data revealed that Tead1 and 2, respectively, are the most and the least abundant transcription factors of the TEAD family in podocytes. (Figure 7.18-A) (Karaïskos et al., 2018) Using mass spectrophotometry, our colleagues have found Tead1 is significantly higher in podocytes as compared to non-podocyte cells in the kidney. (Figure 7.18-C) In line with this, Immunofluorescence staining of kidney sections validated this finding as Tead1 co-localized with Wt1 in the podocyte nucleus. (Figure 7.18-B)

Taken together, Tead1 is the predominant Hippo effector in wildtype mouse glomeruli. Therefore, an in-depth molecular understanding of Tead1 function in podocytes depends highly on exploring the transcriptional network governed by this protein.

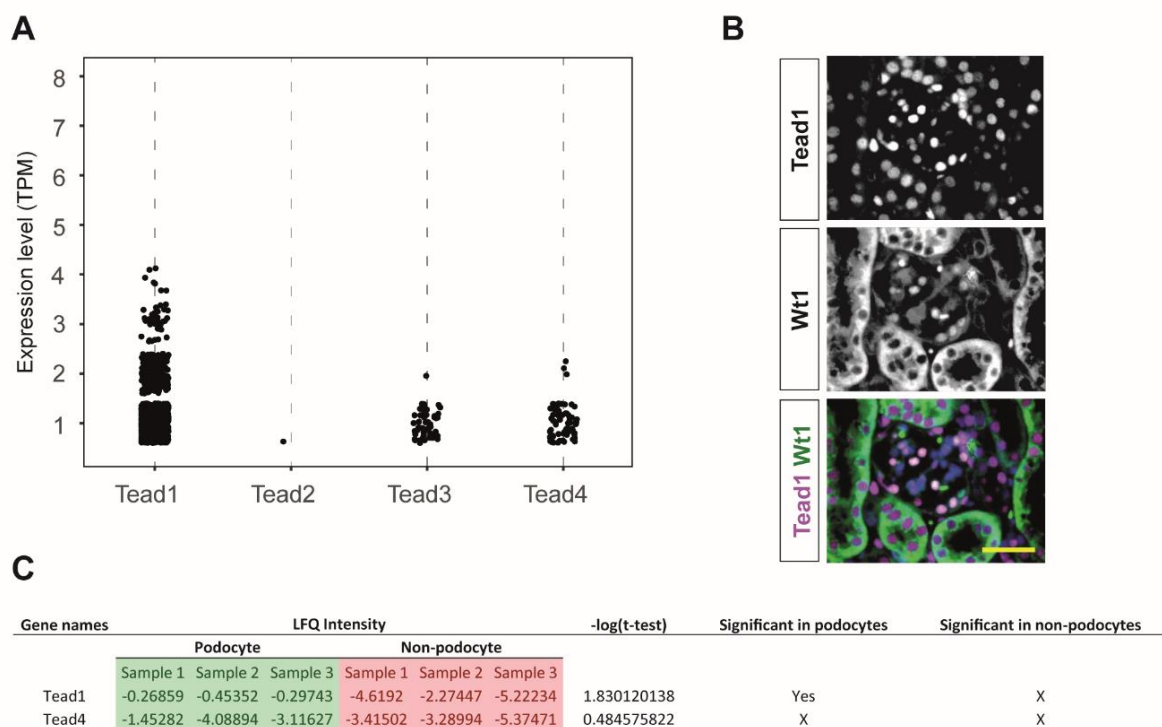


Figure 7.18: RNA and protein expression of TEAD family members in podocytes.

A- mRNA expression values of TEAD family TFs derived from glomerular single cell RNAseq dataset. (Karaïskos et al., 2018). B- Immunofluorescence staining of wildtype mouse glomeruli shows that Tead1 co-localizes with Wt1 in the nucleus. Green and magenta show Tead1 and Wt1 signals, respectively. Scale bar: 20  $\mu$ m. Dr. Fabian Braun has performed the IF staining. C- FACS-sorted podocytes and non-podocyte cells derived from *Nphs2Cre x mTmG* mice shows differing protein abundance for Tead1 and 4 as evaluated by LFQ intensity values. Tead1 is significantly higher in podocytes compared to non-podocyte cells. Dr. Markus Rinschen has kindly shared the results from an unpublished dataset.

## 7.2.2 Chromatin immunoprecipitation of Tead1 in isolated mouse glomeruli introduced technical hurdles.

There are handfuls of challenges in obtaining antibodies for an efficient ChIP experiment. These challenges are more critical in the context of ChIPing for endogenous proteins in model organisms such as mice because the starting material for the immunoprecipitation is limited. A highly recommended alternative in such cases is to tag the protein of interest with an exogenous epitope and use an already-validated antibody against the exogenous tag. (Landt et al., 2012) Epitope-tagging solves the issue of batch to batch variation for antibodies. Moreover, using a well-characterized monoclonal antibody against the exogenous tag eliminates the possibility of epitopes cross-reaction. Given this, a novel mouse line bearing an exogenous *Flag* tagged to *Tead1* was generated in this project using CRISPR/Cas9 technology.

In order to efficiently design the recombinant Flag-tag Tead1, the first criterion to consider was to target the fusion peptide for a locus remote from the nuclear localization signal (NLS) sequence. All the TEAD family members have a classical bipartite NLS consensus sequence which is highly conserved. (Magico and Bell, 2011) In Tead1, the NLS consensus sequence is located at the residues 30 to 97. Moreover, the transcriptional activating domain is located at the residues 167 to 426 in the C-terminus of Tead1. Therefore, the best strategy was targeting the Flag-tag in exon 2 where it does not interfere with any of the mentioned domains. Another criterion was utilization of the endogenous start codon to avoid non-desired Flag expression without Tead1 protein. Furthermore, a flexible spacer (GGGGS) was included to avoid protein misfolding and compromised Tead1 function. (Chen et al., 2013) After the precise evaluation of several *in-Silico* designed sgRNA oligos, the best-matching one was selected for *in vitro* synthesis of the sgRNA. (Figure 7.19)

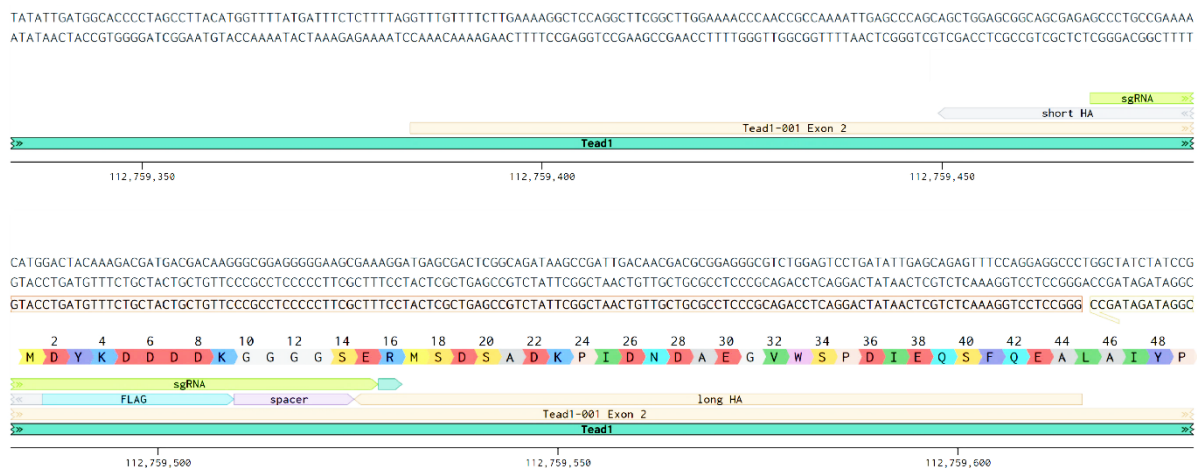


Figure 7.19: Recombination target locus in the exon 2 of the mouse Tead1.

The first two strands are the sense and non-sense nucleotide sequence of the target locus. The third sequence depicts the designed ssODN. The sgRNA targets Cas9 to cut after the start codon. The Flag and spacer sequences will be recombined after the first residue (Methionine). The amino acid sequence of the recombined locus is depicted as well.

T7 endonuclease I assay was used as the primary evaluation for successful sgRNA/Cas9 mediated targeting. (Wyvekens et al., 2015) The heteroduplex DNA which was produced during the hybridization reaction was identified and cleaved by T7 endonuclease I. As a result, two DNA fragments with different band sizes (DNA modified after Cas9-mediated cut and non-modified DNA) appeared in the agarose gel electrophoresis showing that Cas9 has cut the desired loci guided by sgRNA. (Figure 7.20)

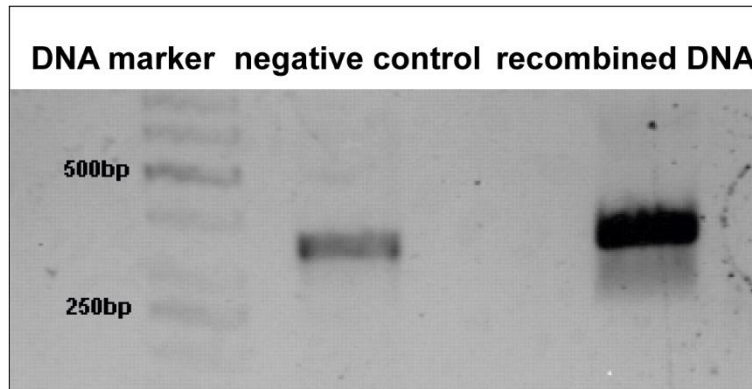


Figure 7.20: T7 endonuclease assay shows successful recombination of the sequence of interest.

The genomic DNA is extracted from transfected NSC-34 cells after recombination. After cleavage by T7 endonuclease I, the recombined DNA is cut to a small and a big fragment shown on 2% agarose gel. The non-recombined DNA will not be cleaved by T7 endonuclease I.

After this step, the electroporation of the zygotes with CRISPR/Cas9 components was performed as previously described. F0 generation mice included 9 live pups and sequencing results showed one mouse has the desired sequence. (Figure 7.21) The male founder was backcrossed to the inbred control females (C57BL/6) to obtain experimental mice after F10 according to the guidelines provided by the LANUV NRW.



Figure 7.21: Alignment of the sequence reads from the founder FLAG-Tead1 mouse with the designed recombinant Tead1.

The upper panel depicts the recombined sequence using Benchling. The colored bars depict sgRNA, short and long homology arms and the flag and spacer sequences. The annotated sequence validates the successful recombination of Flag tag in Tead1 exon 2 with no off-target events within this window.

Although exogenous tagging serves as a robust technique for ChIP experiments, it often raises doubts on the changes that it might introduce to the factor's activity. ENCODE guidelines recommend employing a parallel endogenous protein IP in ChIP experiments in such cases.

(Landt et al., 2012) Besides, the time period for obtaining the experimental mice to perform ChIP experiments is often lengthy. To this end, a modified immunoprecipitation strategy was tested in parallel to mouse breeding to expedite the progress of ChIP experiments.

Standard ChIP experiments are often performed using protein G magnetic beads. However, some mouse antibody isotypes do not efficiently bind to protein G magnetic beads. The Tead1 antibody used in this project was validated for ChIP in several publications previously. (Stein et al., 2015; Tome-Garcia et al., 2018) However, all the Tead1 ChIP experiments have been performed in cells where the starting material is not a limit. After several attempts in performing Tead1 ChIP in isolated mouse glomeruli, the enrichment of the Tead1 target loci was not satisfactory. Therefore, addition of the pre-bound antibody-protein G complex to the nuclear lysate was employed as an alternative strategy to traditional immunoprecipitation assays and a commercially available bridging antibody was included prior to the addition of Tead1 antibody to the protein G magnetic beads. Bridging antibody is essentially a rabbit anti-mouse IgG antibody which binds to both protein G magnetic beads and the mouse-driven antibody with a strong affinity. Therefore, it boosts the enrichment of protein-chromatin complex in ChIP experiments. The performance of bridging antibody in successful Tead1 ChIPing was evaluated in IMCD3 nuclear lysates using mass spectrophotometry. A 250-fold enrichment of Tead1 was observed when bridging antibody was included in the immunoprecipitation procedure. (Figure 7.22-A) The result of ChIP-MS was encouraging to perform the Tead1 ChIP in nuclear lysates obtained from isolated mouse glomeruli. Successful Tead1ChIP in four replicates was assessed by qPCR and as expected, target gene loci (*Lats2*) was enriched significantly higher when the bridging antibody was included in the ChIP procedure. (Figure 7.22-B) Therefore the IP and input samples were submitted for sequencing.

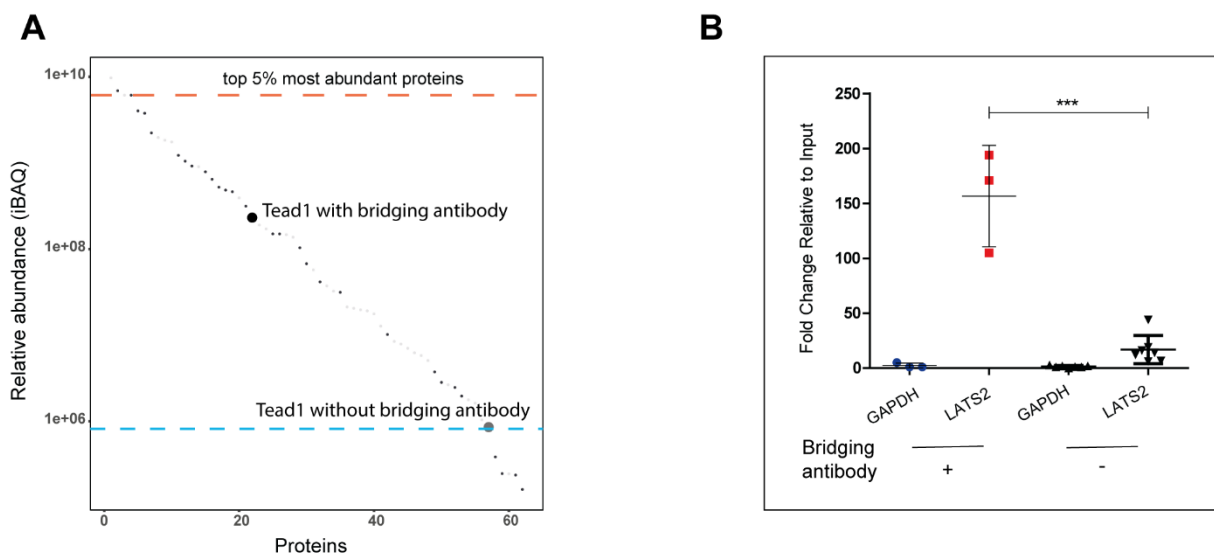


Figure 7.22: Addition of the bridging antibody significantly increases the Tead1 chromatin immunoprecipitation.

A- Tead1ChIP-MS of the cross-linked IMCD3 nuclear lysates with and without the bridging antibody. The x-axis shows the ranking of the proteins from the most abundant to the least abundant. The y-axis shows the relative protein abundance (iBAQ- log10 scale). There is a 250-fold enrichment of

Tead1 when the IP is performed with the bridging antibody. B- Tead1ChIP-qPCR of the cross-linked nuclear lysates taken from the mouse isolated glomeruli with and without the bridging antibody. There is a significant relative fold enrichment of the Tead1 target gene loci, *Lats2*, compared to the negative control loci, *GAPDH*, when the bridging antibody is used in the IP experiment. ( $p$  value < 0.0001)

### 7.2.3 Quality check for Tead1 ChIPseq verifies robustness of the dataset.

To assess the quality of Tead1 ChIPseq dataset, strand cross-correlation analysis was performed which showed a high signal-to-noise ratio. (Figure 7.23-A) As the next step of quality check, pairwise comparison of Tead1 ChIPseq peaks was done by the IDR method. (Figure 7.23-B)

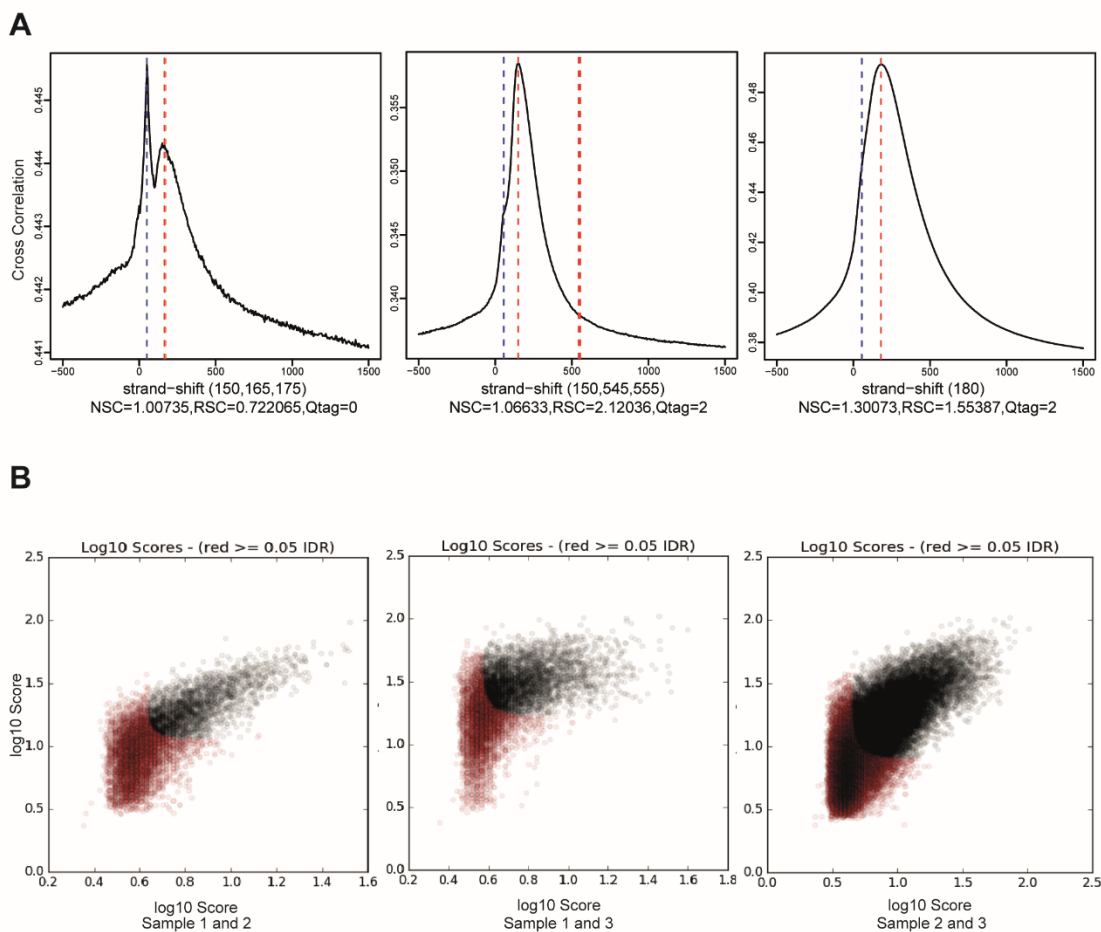


Figure 7.23: Three replicates of Tead1ChIP-seq show decent quality.

A- Strand cross-correlation analysis suggests the second and the third replicates have higher quality when compared to the first replicate. B- The IDR analysis shows that majority of the signal pass the threshold at 0.05.

The consistency between the sample pairs was approved as majority of the signal passed the IDR threshold set at 0.05. Furthermore, peak conservation and *de novo* motif enrichment scores were calculated for the merged peak summits demonstrating very sharp peaks at the

center. (Figure 7.24-A, B) Expectedly, the known Tead1 motif had the highest enrichment score besides Wt1, Klf, etc. Finally, the spearman correlation test for the ChIPseq normalized reads depicted robust correlation coefficients for each sample and its relevant pseudo pair. (Figure 7.24-D)

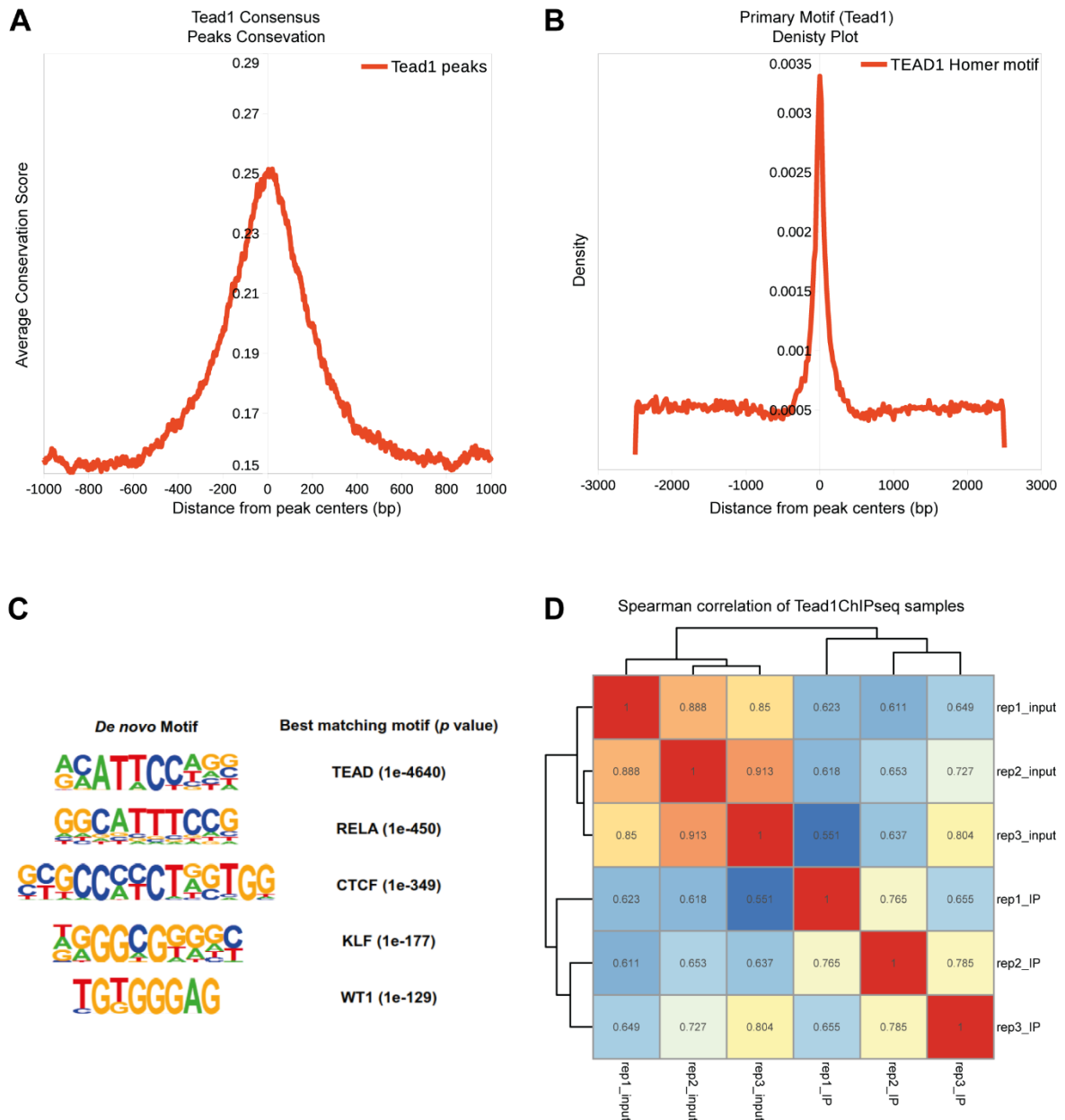


Figure 7.24: Tead1ChIPseq quality evaluation.

- A- Metagene plot of consensus Tead1 peaks shows high peak conservation. The x and y-axis depict the distance from the peak center and the average conservation score, respectively. B- Motif density plot of primary motif in Tead1 consensus peaks. High enrichment of Tead1 primary motif shows successful ChIP experiment. The x and y-axis depict the distance from the peak center and the peak density, respectively. C- Sequence logos of the top 5 enriched TF motifs from *de novo* motif enrichment analysis of Tead1 ChIPseq. D- Spearman correlation test for the normalized reads shows high correlation coefficients per sample.

#### **7.2.4 In podocytes, Tead1 predominantly regulates genes involved in cell-adhesion and actin cytoskeleton regulatory pathways.**

Tead1 peak distribution assessment across the whole genome revealed that most of the peaks were located far from the TSS. (Figure 7.25-A) In fact, majority of Tead1 peaks were in intronic and intergenic elements suggesting an enhancer-based transcriptional regulation. This is in line with existing literature on the enhancer-mediated transcriptional activity of TEAD family members. (Stein et al., 2015)

Previously, TEA family members have been identified to mediate handfuls of cellular functions majority of which dealing with cell-substrate adhesion, cell migration, EGFR signaling and mechano-sensation via actin cytoskeleton homeostasis. (Tome-Garcia et al., 2018; Totaro et al., 2018, 2019) However, a great deal of literature in this area has focused on cancer cells. In this thesis, functional annotation analysis identified Tead1-dependent functions in podocytes. In wildtype healthy podocytes, Tead1 predominantly orchestrates gene-regulatory functions in cell-adhesion and actin cytoskeleton pathways. (Figure 7.25-B) Based on what was observed in Tead1 binding on the gene regulatory elements, it is not far from expectation that Tead1 exerts its cellular functions by binding to intergenic and intronic sites in putative enhancers.







## 7.2.5 Cooperation of Tead1 and Wt1 in gene regulation by co-binding at key podocyte target genes.

Our group has previously shown the co-occurrence of Wt1 and Tead1 motifs in Wt1 ChIPseq dataset obtained from adult mice. (Kann et al., 2015) In line with this, motif enrichment analysis of the Tead1 ChIPseq data showed mutual existence of Wt1 and Tead1 motifs, as well as Tcf21, KLF TFs, MafB, Lmx1B and CTCF motifs, suggesting these TFs tend to cooperate in their gene regulatory programs. (Figure 7.26-A) Acknowledging this, the distance distribution of the Tead1 and Wt1 ChIPseq adjacent peaks revealed majority of them happen to be remote from the TSS (more than 200 bp distance). Within this window, over 7000 mutual binding loci were identified for Tead1 and Wt1. (Figure 7.26-C)

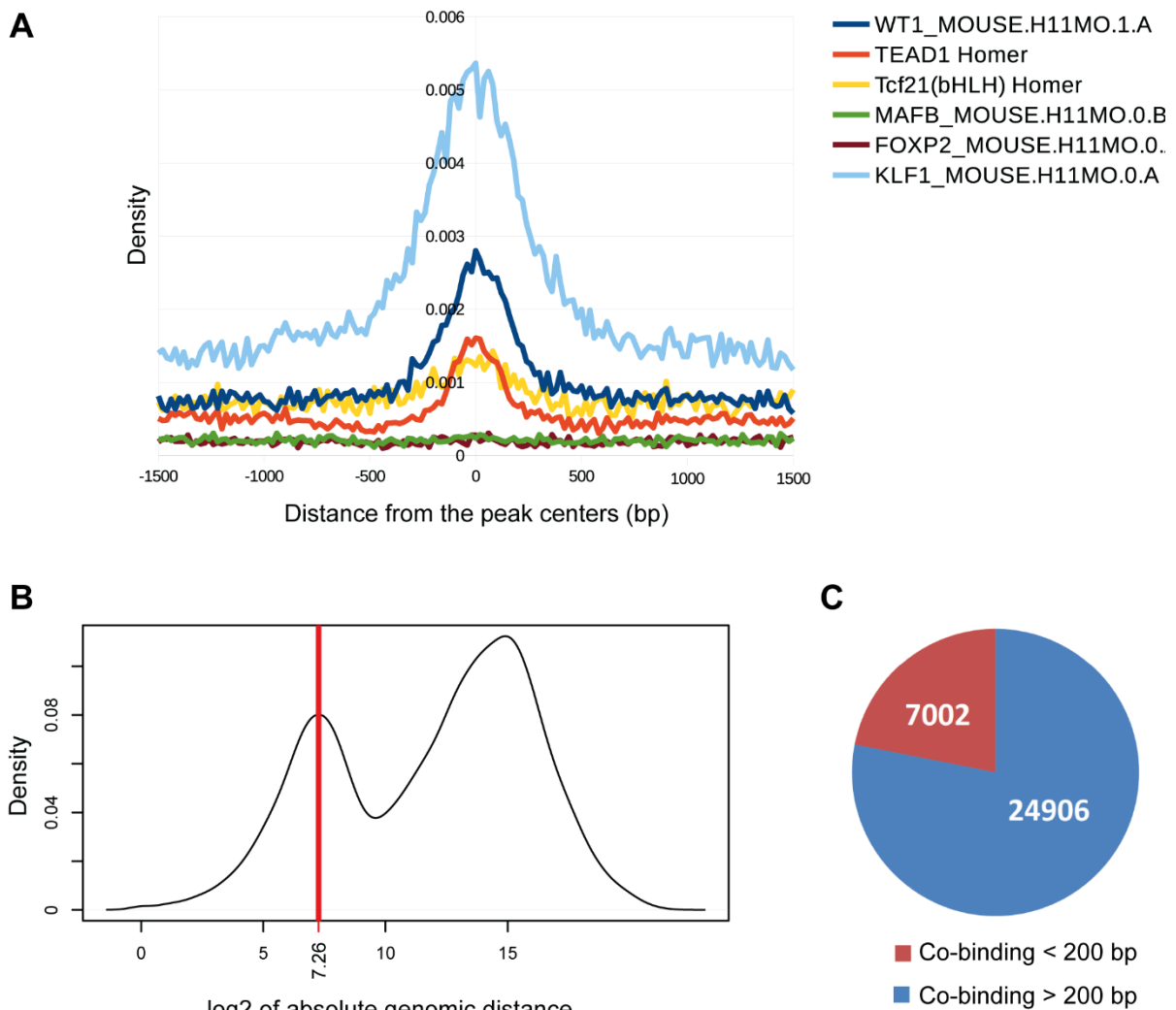


Figure 7.26: Tead1 and Wt1 co-binding assessment.

A- Motif density plots within Tead1 & Wt1 co-bound peaks show motifs enriched in Tead1-Wt1-bound regions. The x and y-axis depict the distance from the peak center and the density, respectively. B- Distance distribution density plot for adjacent Tead1 and Wt1 peaks. The y-axis shows the density while the x-axis depicts the log2 transformed of the absolute genomic distance in base pair.  $2^{7.26} = 153$  bp. C- Pie chart shows the number of co-bound regions by Wt1 and Tead1 divided into >200 pb and <200 bp distance.

In addition, Genome browser plots of exemplary target genes such as *NPHS1* and *2*, *Itga3* and *Actn4* confirmed the co-occurrence of Tead1 and Wt1 binding sites which further provided strong evidence for interaction of the TFs on a gene-regulatory level. (Figure 7.27)

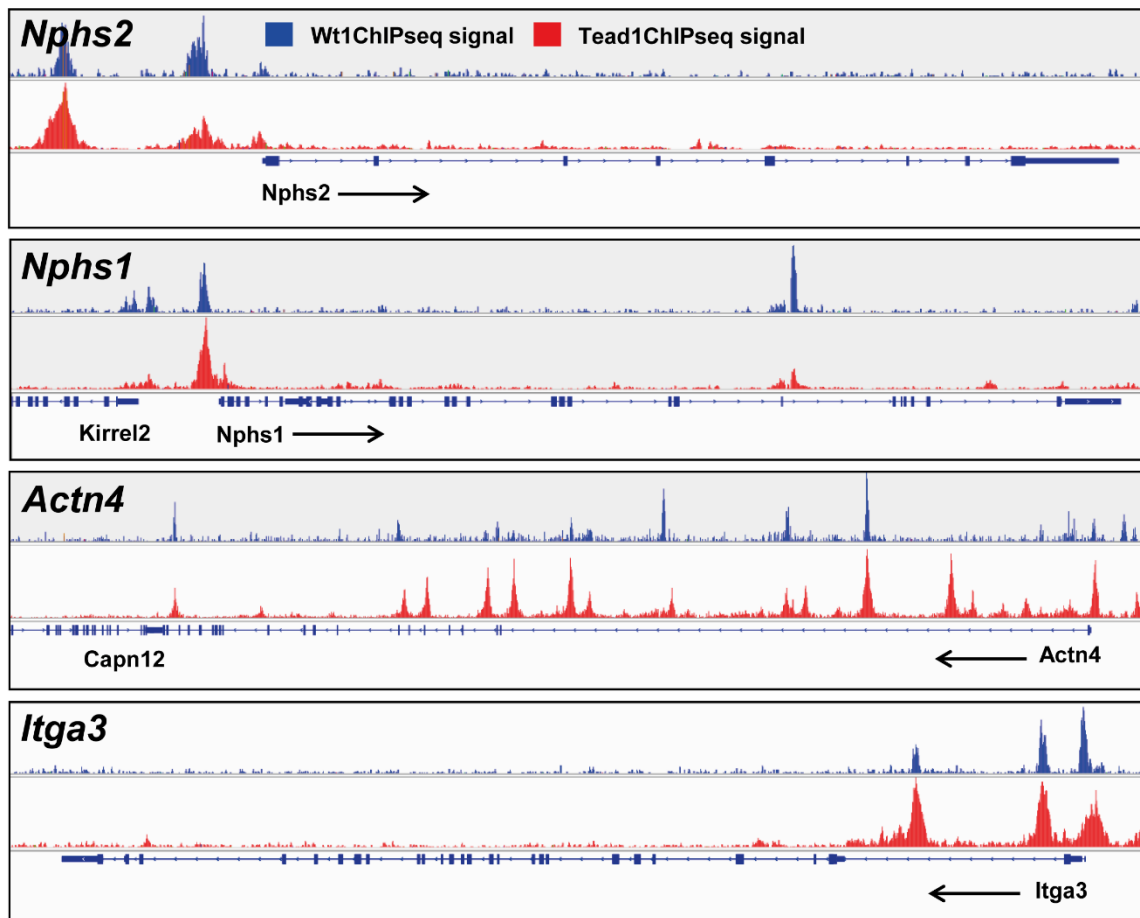


Figure 7.27: Genome browser plots showing Tead1 and Wt1 ChIPseq signals and exon/intron structure of target genes.

The upper (blue) track shows Wt1 ChIPseq signal while the lower (red) track shows Tead1 ChIPseq signal. Promoters, intronic and intergenic sites show co-occurrence of Tead1 & Wt1 ChIPseq signals. The exon and introns are marked by the bottom blue boxes and lines, respectively.

Functional annotation of the Tead1-Wt1 co-bound genes, moreover, re-approved Tead1 and Wt1-guided regulation of actin cytoskeleton homeostasis. (Figure 7.28) Interestingly, Wt1 target genes seem to be regulated more independently whereas Tead1 target genes show more co-dependence to both transcription factors. Altogether, the results of this part demonstrate that Tead1 and Wt1 interact on a gene-regulatory level by co-binding at key podocyte target genes. Functionally, genes involved in actin cytoskeleton regulation and cellular movement are overrepresented among the targets of this interaction.

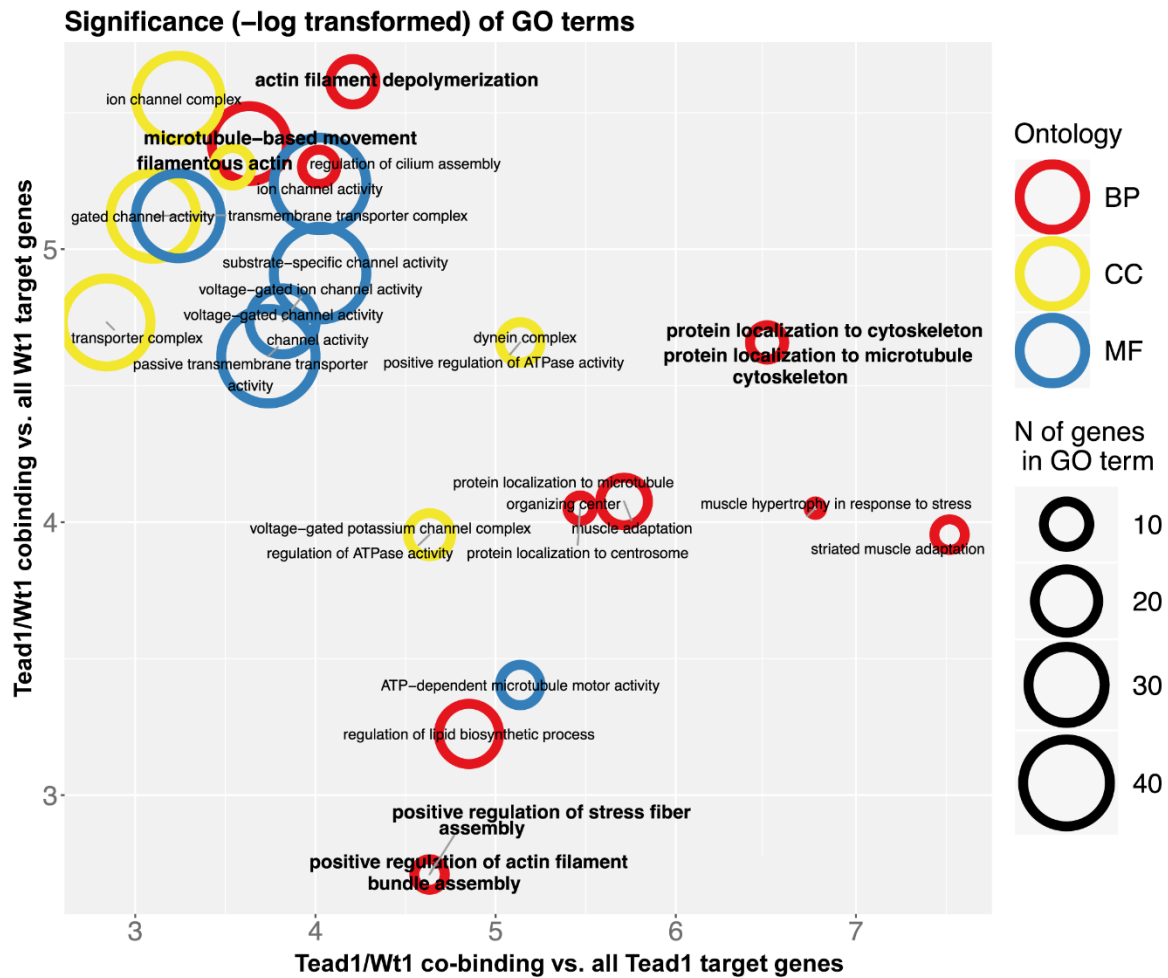


Figure 7.28: Functional annotation analysis of Tead1 and Wt1 co-binding on gene regulatory regions. Bubble plot shows the log transformed significance of GO terms overrepresented in the target genes of Tead1 & Wt1 co-bound peaks vs. Wt1 targets (y-axis), and vs. Tead1 targets (x-axis), respectively. Selected GO-terms are highlighted in bold. BP: biological process, CC: cellular component, MF: molecular function, and marked by three different colors. The size of the circles correlates with the number of the genes contributing to the GO term.

### 7.3 Part three: Single-cell RNA sequencing of isolated mouse glomeruli

#### 7.3.1 Single-cell RNA-sequencing identifies the relevant cell populations in purified glomeruli

Isolation of mouse glomeruli was performed using a standardized protocol. (Boerries et al., 2013) The yield and quality of the glomerular isolation was checked, and extra washing steps was carried out if non-glomerular structures were abundant in each sample. (Figure 7.29-A) Live fixed cells were further processed for single-cell RNA sequencing using the Drop-seq method. (Macosko et al., 2015) Each independent biological replicate consisted of the single cells derived from isolated mouse glomeruli from 8 mice. Using unique molecular identifiers (UMIs), a total of 14,722 cells were identified. The general study design is schematically shown in Figure 7.29-B.

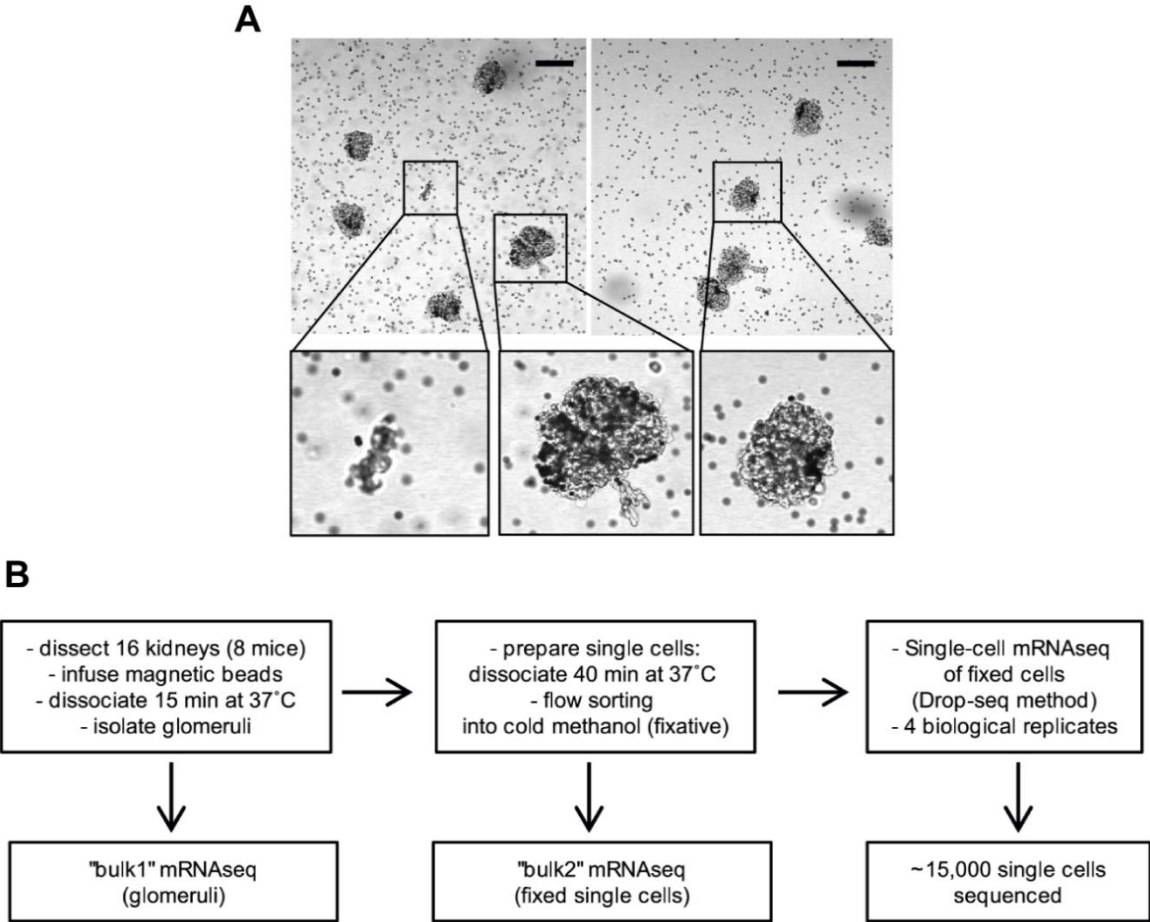


Figure 7.29: Single-cell RNA sequencing of isolated mouse glomeruli.

A- Brightfield microscopic images of isolated mouse glomeruli exhibiting high purity of glomerular isolation. Insets indicate a tubular fragment (left), a decapsulated glomerulus with protruding vasculature (middle) and an avascular, decapsulated glomerulus (right). Scale bar: 100  $\mu$ m. B- Schematic design showing the experimental workflow. Image adapted from (Karaiskos et al., 2018)

Employing a previously developed algorithm, cell-type marker genes were scored, and 1768 possible cell doublets were removed from further analysis. The number of cell doublets were normal given the fact that in Drop-seq experiments approximately 10% of identified cells are not singlet cells and this is an inherent phenomenon in the Drop-seq workflow. (Karaiskos et al., 2017) After the doublet removal, the data set consisted of 12,954 cells, with a median of 630 genes and 950 unique molecular identifiers per cell. (Figure 7.30-A)

Unsupervised clustering of the final single cells revealed five major cell clusters three of which were glomerular cell types: podocytes (80% of total singlet cells), endothelial cells (12%) and mesangial cells (2%). The other two cell types were tubular cells (6%) and immune cells (0.2%). (Figure 7.30-B) The results of the single-cell sequencing is offered on an interactive free webtool: <https://shiny.mdc-berlin.de/mgsca/>

All the biological replicates were shown to contribute equally to the identified cell types (data not shown here). Identification of the cell types were based on the expression of the cell-type specific marker genes. Therefore, and as expected, glomerular cells showed specific expression of their established marker genes such as *NPHS1* and 2 for podocytes, *Pecam* and *Flt1* for endothelial cells and *Ren1* and *Acta2* for mesangial cells. (Figure 7.30-C)

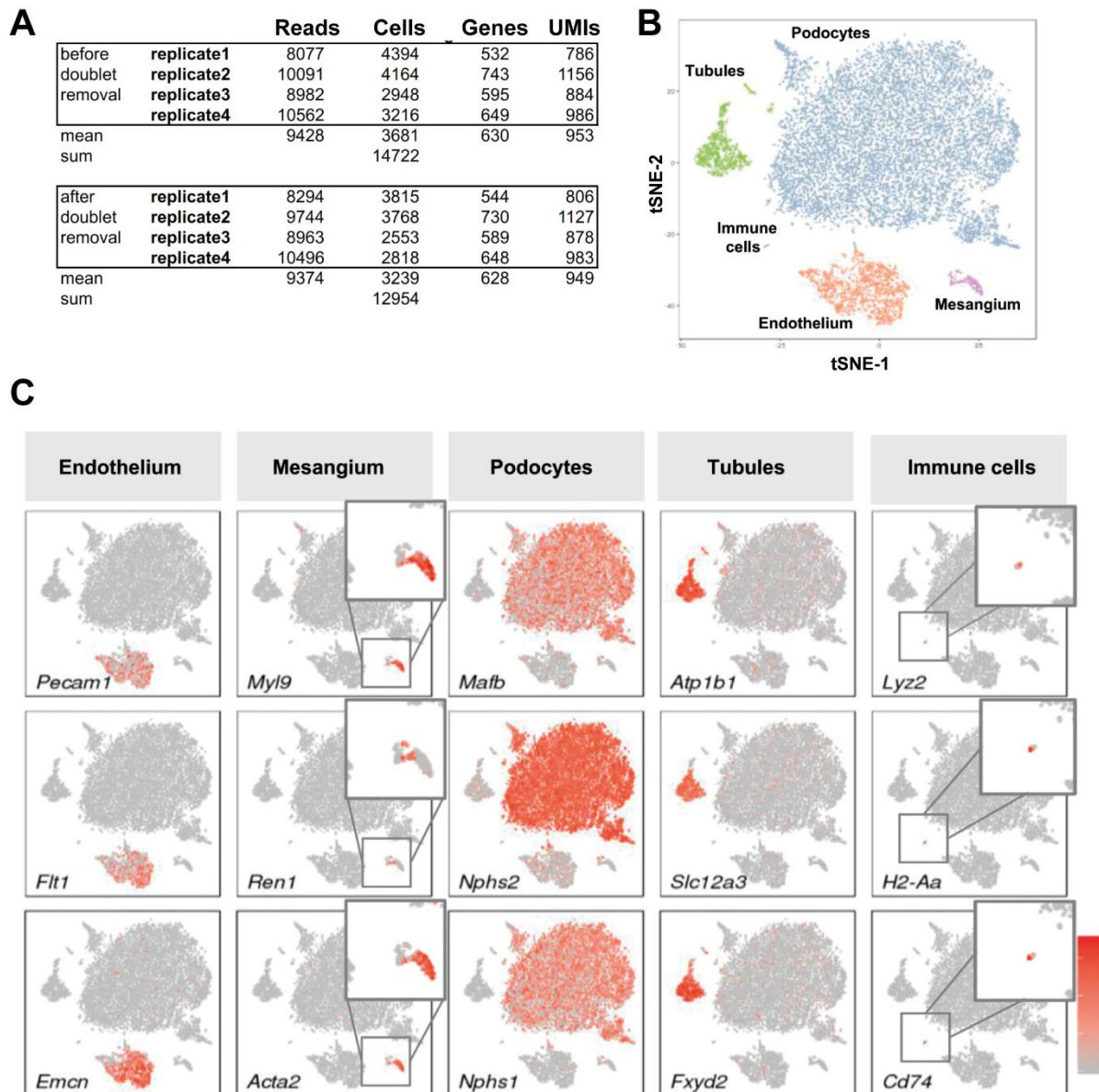


Figure 7.30: Single-cell RNA-sequencing of the purified mouse glomeruli identifies five known cell populations.

A- Median number of genes, transcripts (UMIs) and reads per cell in distinct replicates. The table enlists the number of cells and their relevant UMIs as well as the number of detected genes and transcripts per cell. Numbers are shown for data before and after doublet removal. B- tSNE plots (t-Distributed Stochastic Neighbor Embedding) show five distinct clusters corresponding to glomeruli (12% endothelium [n=1556], 2% mesangial cells [n=216], and 80% podocytes [n=10,325]) and non-glomerular structures (6% tubules [n=828] and 0.2% immune cells [n=29]) based on the top most variable marker genes per cluster. C- tSNE plots representing the expression of established marker genes colored based on the normalized expression levels (gray represents low and red represents high expression values). Image adapted from (Karaikos et al., 2018)

One general consideration in single cell RNA sequencing data interpretation is to compare the data to bulk mRNAseq of the same samples to check for the effects of the single-cell preparation. To this end, the single-cell RNAseq data was compared with the bulk polyA-



RNAseq libraries prepared from isolated mouse glomeruli before and after dissociation to single cells (named bulk1 and bulk2, respectively). (Figure 7.31-A) Despite of an expected correlation between the bulk mRNAseq with the single cell RNAseq datasets, the abundance of cell types was affected by the single cell dissociation. (Figure 7.31-B) The larger proportion of podocytes versus the endothelial cells is therefore due to the possible lysis of endothelial cell population through the tissue dissociation step.

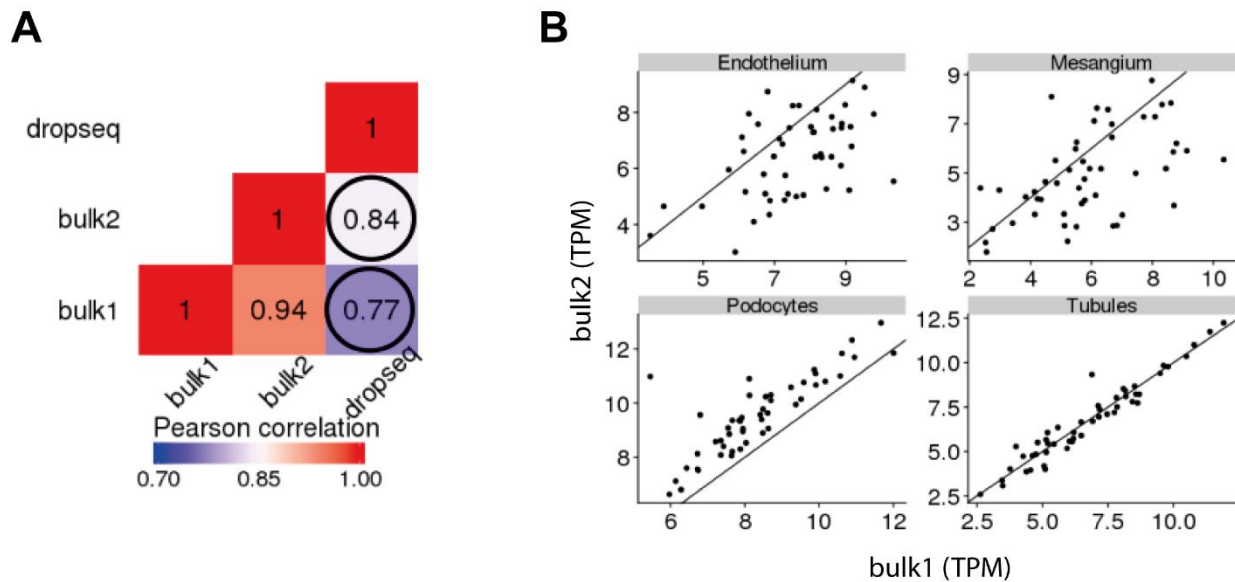


Figure 7.31: Comparison of single cell RNAseq data with bulk mRNAseq.

A- Pearson correlations test between Drop-seq single-cell RNAseq and bulk mRNAseq samples. Coverage for all datasets is the same. “bulk1” represents the RNAseq data from lysed glomeruli (before tissue dissociation to singlet cells) and “bulk2” represents the RNAseq data from lysed single cells of the glomeruli (after tissue dissociation to singlet cells by enzymatic digestion). High correlation coefficients are seen for both bulk samples, however, bulk2 correlation with the single-cell data is better as expected. B- Pairwise comparison of bulk1 and 2 samples for the 50 most variable genes per cell type identified in the single-cell RNAseq data. As shown, podocytes are overrepresented in the “bulk2” sample compared with “bulk1” which explains the bias imposed by the enzymatic digestion and single cell preparation workflow. In the same context, endothelial and mesangial cells exhibit a higher dispersion in an opposite direction and the tubular cells are seemingly not affected by the single cell preparation. Image adapted from (Karaiskos et al., 2018)

### 7.3.2 Single-cell transcriptomics reveal novel molecular markers specific to glomerular cell types.

Bulk mRNAseq studies often fail to identify very low and yet unique transcripts whose presence can only be detected in single cell RNAseq experiments. Since this study was the first single-cell transcriptomic analysis of the isolated mouse glomeruli, the next focus was directed to the identification of novel markers for the main three glomerular cell types. At first, a list of known marker genes was compiled by identification of highly variable genes between podocytes, endothelial cells and mesangial cells. A thorough literature review was conducted

to complete the list and then, novel markers were identified and re-approved on the protein level using immunostaining images of the Human Protein Atlas (Figure 7.32).

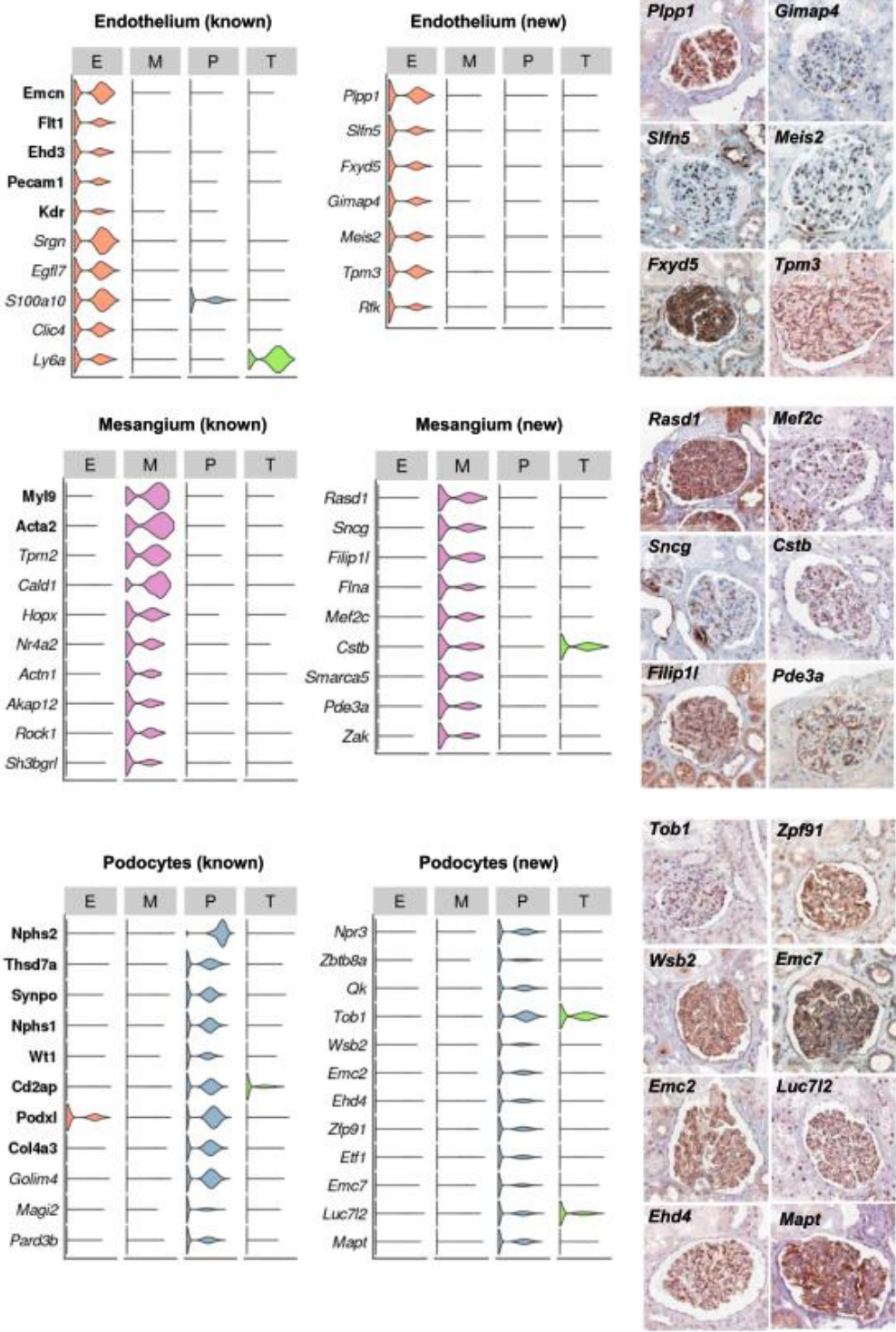


Figure 7.32: Identification of novel markers for three main glomerular cell types.

Violin plots show the distribution as well as the relative expression of highly variable genes in endothelial cells, mesangial cells and podocytes. The first and second columns denote established and novel markers, respectively. The Right panel represents the immunohistochemistry images of such markers from Human Protein Atlas (HPA) validating the novel marker prediction from our



single-cell RNAseq dataset. Image areas are shown in 500x500 pixels =200  $\mu\text{m}^2$ . Image adapted from (Karaiskos et al., 2018)

### **7.3.3 Sub-clustering reveals the presence of endothelial subpopulations.**

An advantage of single cell RNA sequencing is the identification of cell heterogeneity in each cell population. Thus, sub-clustering was performed for podocytes and endothelial cells as the two larger cell population within the glomerulus. Endothelial cells showed 5 distinct sub-clusters. (Figure 7.34-A, B) However, the sub-cluster 4 showed high expression values for podocyte-specific marker genes. Therefore, it was identified as a residual cell doublet cluster and it was eliminated from further analysis. The remained four sub-clusters exhibited an equal distribution among all four replicates. (Figure 7.34-C, D)

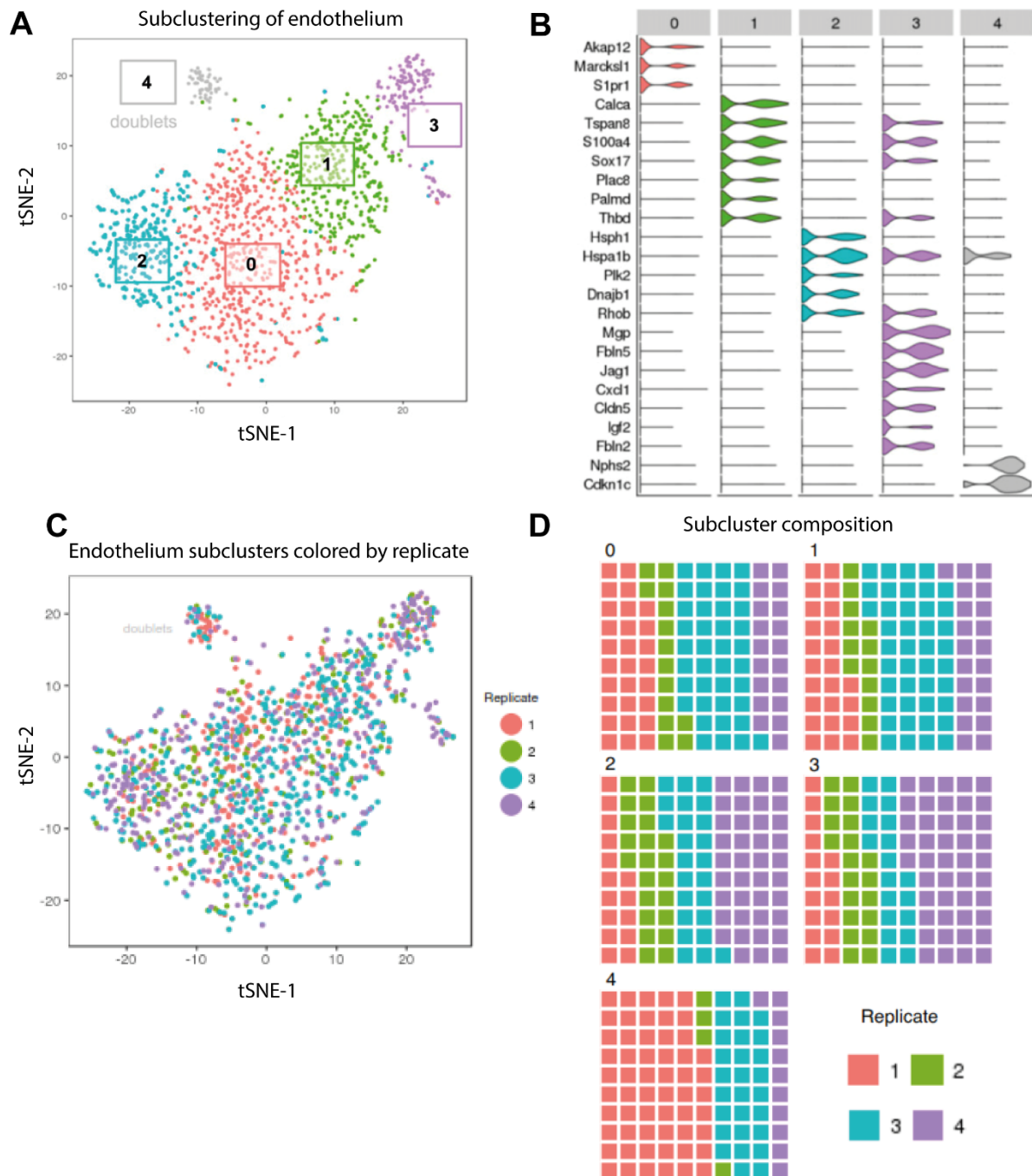


Figure 7.33: Subclustering of glomerular endothelium.

A- t-SNE representation of endothelial cell subclusters. Five subclusters are identified. Cluster 4 exhibits expression of podocyte-specific genes such as *Nphs2* and *Cdkn1c* and represents residual cell doublets. Cluster 4 is regressed out from further analysis. B- Violin plots show distribution and relative expression of highly variable genes within each subcluster. C- t-SNE plots show all four biological replicates contribute to all subclusters. D- Waffle plots show distribution of all four replicates in the endothelial cell subclusters. Each square depicts 1% of the total cell number per subcluster. Image adapted from (Karaiskos et al., 2018)

Functional annotation of the endothelial cell subclusters using pathway and gene set overdispersion analysis revealed four distinct cellular processes (cell adhesion, cell

maturation, stress response, and cell proliferation) which might imply different states of endothelial cells from homeostasis to activation. (Figure 7.34-A)

Interestingly, the Human Protein Atlas images of the kidney sections for some of the subcluster determining genes namely *S100a4*, *Thbd*, *Hspa1b*, and *Fbln2* showed a heterogenous staining pattern on the protein level. (Figure 7.34-B) However, it is not known if this heterogeneity stems from the individual cell localization within a healthy capillary tuft or it reflects localization in other parts of the kidney. Thus, it is the subject for further investigation.

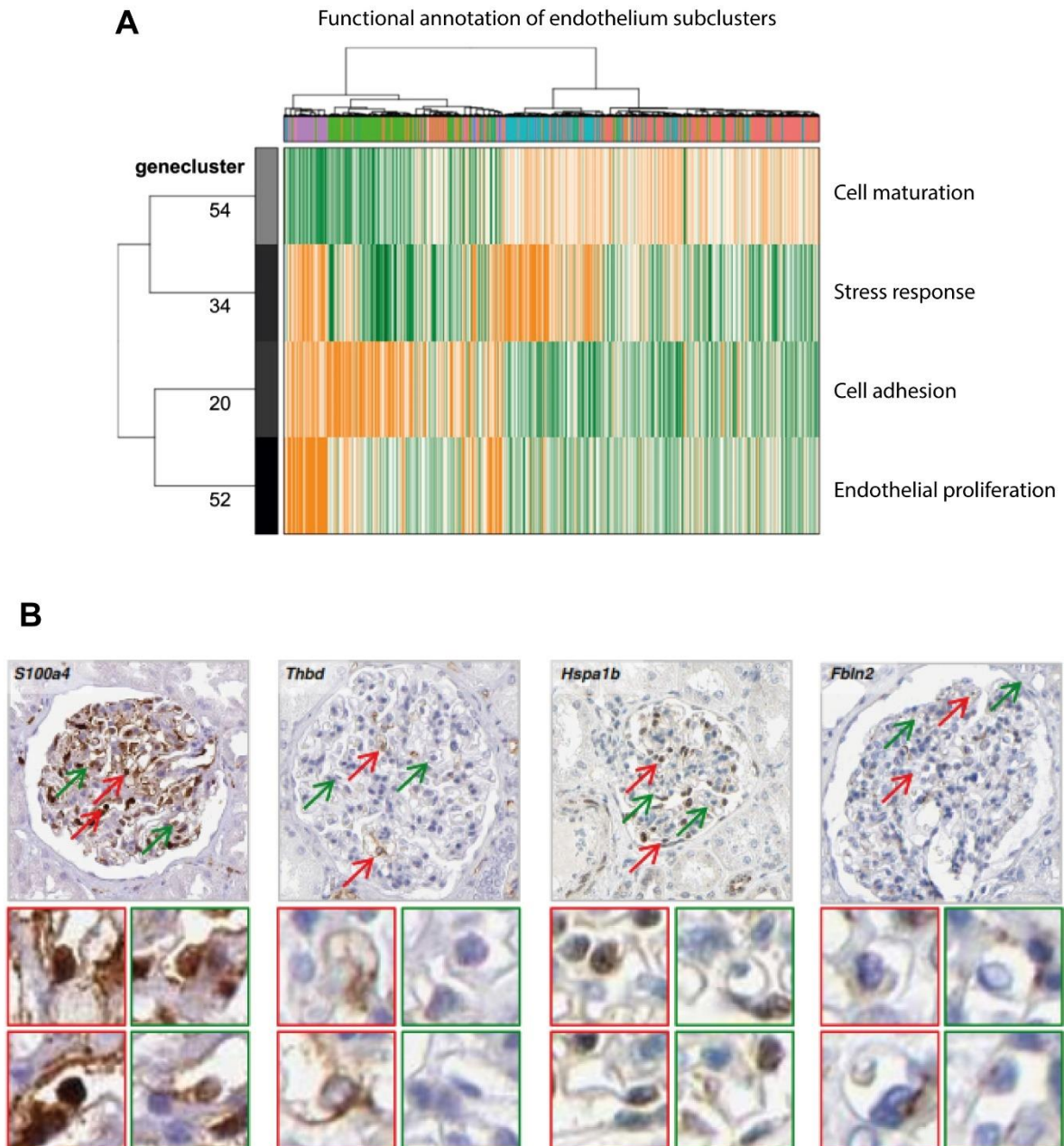


Figure 7.34: Endothelial subclusters are responsible for various cellular functions.

A- The heatmap depicts four distinct endothelial functions relevant to endothelial subclusters as identified by the pathway and overdispersion analysis. (the colored bar on the top represents endothelium subclusters (0: red; 1: green; 2: blue; 3: purple) B- The immunohistochemistry images of

selected subcluster markers (*S100a4*, *Thbd*, *Hspa1b*, and *Fbln2*) from Human Protein Atlas (HPA) validates endothelial cell heterogeneity in human glomeruli. Endothelial cells are identified by intracapillary nuclei. Red arrows and the corresponding insets depict strong *S100a4* expression and a positive expression for *Thbd*, *Hspa1* and *Fbln2* proteins. Green arrows, on the other hand, depict weak *S100a4* expression or no expression for *Thbd*, *Hspa1* and *Fbln2* proteins. Image areas are shown in 50x50 pixels =20  $\mu\text{m}^2$ . Image adapted from (Karaiskos et al., 2018)

#### **7.3.4 Sub-clustering reveals a limited heterogeneity of podocytes.**

Although sub-clustering in podocytes was based on a more subtle gene expression difference, it identified seven categories. (Figure 7.35-A, B) However, a marked stress response signature was found in cluster 4 which can be explained by the tissue dissociation procedure and its following gene expression modification. In line with this, an increased expression of stress response genes in bulk 2 dataset was detected compared to the bulk 1. Therefore, all the stress response genes were excluded from further analysis and re-clustering was performed which identified six subclusters. (data not shown here) The remained six subclusters exhibited an equal distribution among all four replicates. (Figure 7.35-C, D) From all six categories, subclusters 3 to 5 were identified robustly and marker gene analysis revealed some genes and transcripts from mouse-specific microRNAs and noncoding RNAs. Meanwhile, the other three clusters did not exhibit specific marker genes and/or transcripts. As the number of coding transcripts were not enough to draw a meaningful conclusion by functional analysis, pathway and gene set overdispersion analysis did not show conclusive results.

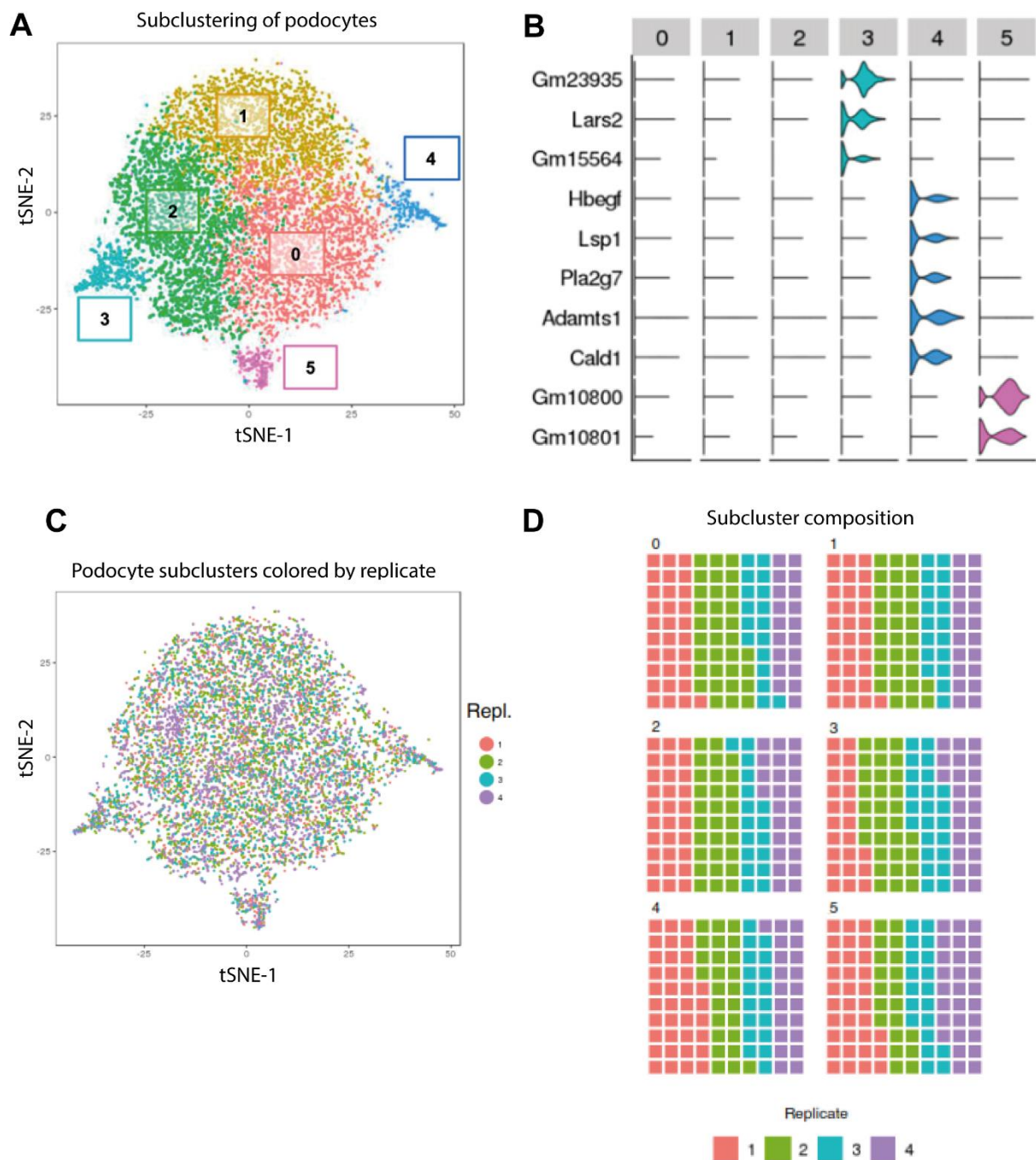


Figure 7.35: Subclustering of glomerular podocytes.

- A- tSNE representation of podocyte subclusters. Six subclusters are identified after exclusion of the stress response genes. B- Violin plots show distribution and relative expression of highly variable genes within each subcluster. C- tSNE plots show all four biological replicates contribute to all subclusters. Cells are color-coded per replicate. D- Waffle plots show distribution of all four replicates in the podocyte subclusters. Each square depicts 1% of the total cell number per subcluster. Image adapted from (Karaikos et al., 2018)

However, immunofluorescence staining of Lars2 and Cald1 on the isolated glomeruli from *Nphs2Cre x mTmG* mice showed heterogenous colocalization of these sub-cluster markers in



podocytes. (Figure 7.36, Figure 7.37) Both Lars2 and Cald1 have established role in podocytes. Lars2 is a mitochondrial Leucyl tRNA synthetase which is mutated in hereditary FSGS. (Cheong et al., 1999; Jansen et al., 1997)

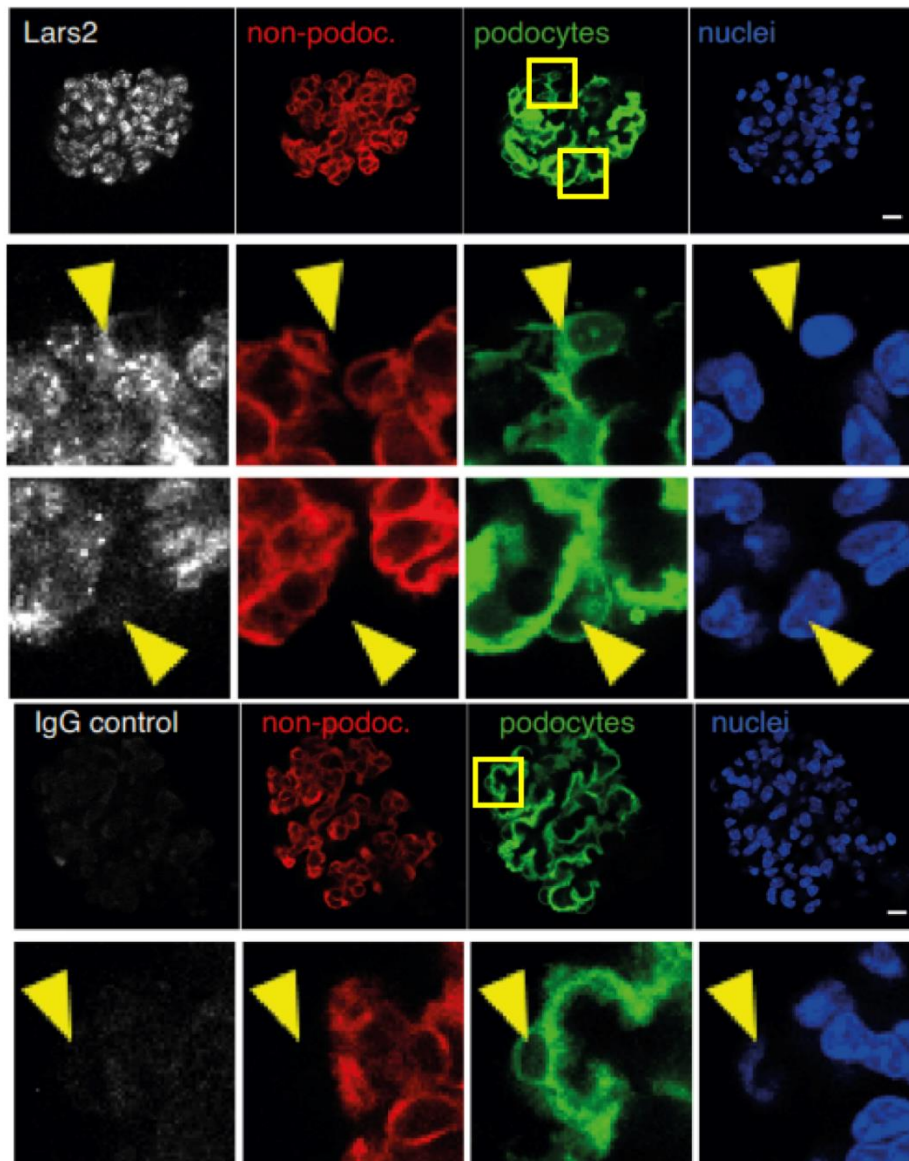


Figure 7.36: Laser scanning confocal microscopy of Lars2 staining in double-fluorescent reporter mice.

Matrigel-embedded glomeruli isolated from perfused kidneys of transgenic *Nphs2CrexmTmG* CD1 male mice are stained with Lars2 antibody or IgG control. Podocytes express membranous green fluorescent protein (GFP) in the presence of Cre while non-podocyte cells express membranous Tomato (Red). Yellow squares depict magnified areas of the podocytes. Yellow arrowheads point to the differential Lars2 signal in two different podocytes whereas IgG staining is expectedly negative.

Scale bar: 10  $\mu\text{m}$ . Magnified areas: 22x22  $\mu\text{m}^2$ . Image adapted from (Karaiskos et al., 2018)

Cald1 or Caldesmon 1 interacts with actin, myosin and calmodulin and it is crucial for non-muscle cell contraction. Cald1 has been shown to be involved in the development of diabetic nephropathy. (Jiang et al., 2016; Śnit et al., 2017; Wang et al., 2016) Taken together, podocyte

heterogeneity is highly probable in healthy mouse glomeruli. However, more data from other animal models as well as human samples is needed to validate this heterogeneity in kidneys.

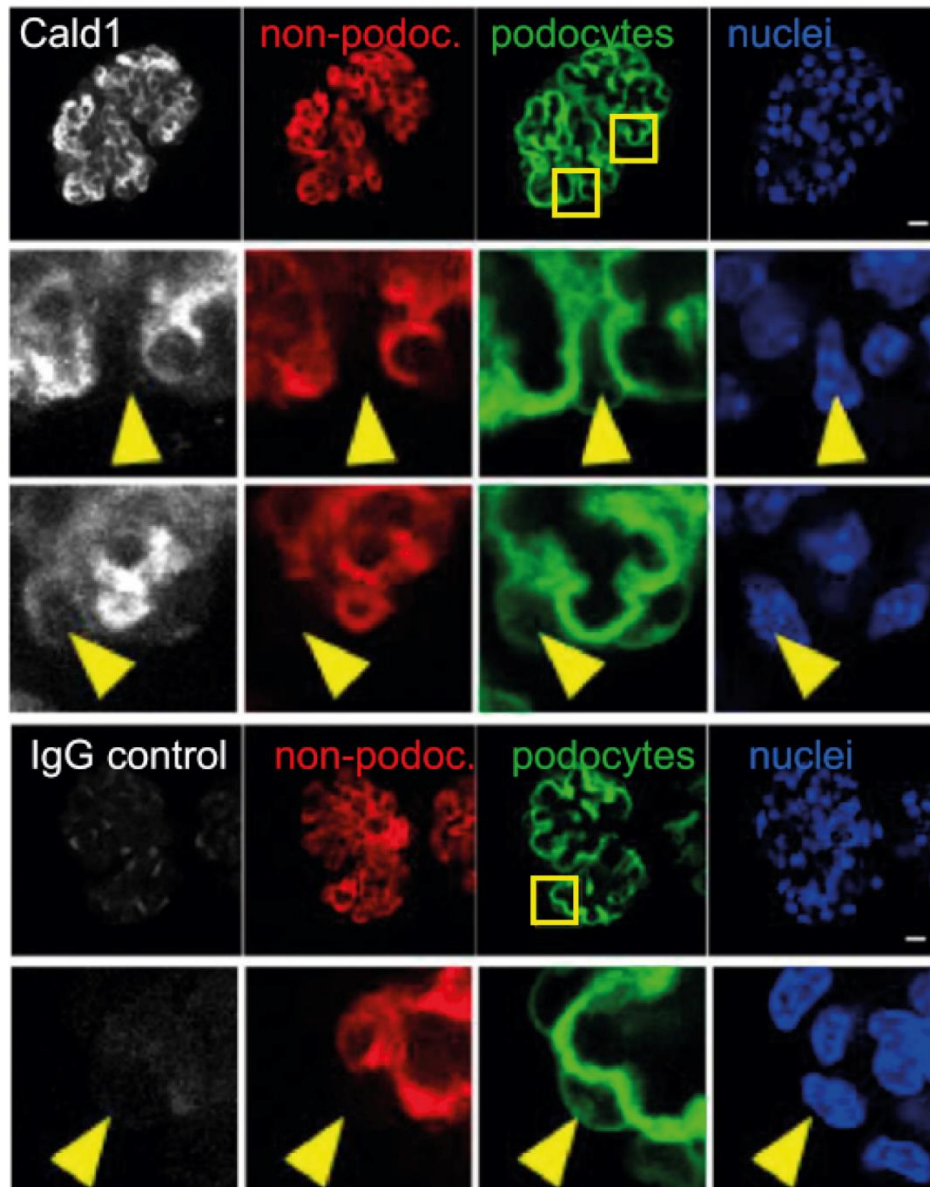


Figure 7.37: Laser scanning confocal microscopy of Cald1 staining in double-fluorescent reporter mice.

Matrigel-embedded glomeruli isolated from perfused kidneys of transgenic *Nphs2CrexmTmG* CD1 male mice are stained with Cald1 antibody or IgG control. Podocytes express membranous green fluorescent protein (GFP) in the presence of Cre while non-podocyte cells express membranous Tomato (Red). Yellow squares depict magnified areas of the podocytes. Yellow arrowheads point to the differential Cald1 signal in two different podocytes whereas IgG staining is expectedly negative. Scale bar: 10  $\mu\text{m}$ . Magnified areas: 22x22  $\mu\text{m}^2$ . Image adapted from (Karaiskos et al., 2018)

## 8 Discussion

### 8.1 Wt1 reprograms podocytes in the face of damage.

The identification of Wilm's tumor 1 (WT1) gene roots back to 1990 when it was found as a genetic predisposition resulting in Wilm's tumor. (Call et al., 1990; Gessler et al., 1990) Wt1 is a highly diverse protein and is encoded by ten exons. Thus far, 36 isoforms have been reported in mammals generated by alternative transcription and translation start sites, alternative splice sites and RNA editing strategies. (Hastie, 2017)

In the adult kidney, Wt1 expression is restricted to podocytes nuclei and there is a balance among its isoforms including the mostly studied ones i.e. +KTS and -KTS isoforms. (Ullmark et al., 2018) Noticeably, kidney disease phenotypes attributed to mutations of Wt1 can directly reflect the specific role of this protein during development and/or after differentiation. Often, developmental syndromes and malignancies which arise from mutations of Wt1 compromise the KTS isoforms and/or zinc fingers. On the other hand, mutations which result in glomerulosclerosis often happen in less important domains but show the key role of Wt1 in the maintenance of glomerular structure and function.

In this thesis, a mouse model of glomerulosclerosis is used in which exon 1 is deleted in one of the Wt1 alleles. Heterozygous deletion of Wt1 does not compromise the kidney development as evaluated by the morphological as well as functional analysis of the mice at the postnatal day 6. The shape and weight of the *Wt1<sup>het del</sup>* mice show no difference with that of the control mice. Moreover, the kidneys function normally and there is no trace of proteinuria in *Wt1<sup>het del</sup>* mice. 4-week old mice, however, show significant proteinuria and slight GBM thickening and effacement. This is the early phase of FSGS when sclerosis is not yet evident (Early FSGS). 12-week old mice, moreover, manifest an explicit sclerosis besides the proteinuria (Late FSGS). This data confirms the previous findings by Menke and his colleagues in 2003. They found that the early indications of nephropathy in *Wt1<sup>het del</sup>* mice is proteinuria and glomerulosclerosis occurs relatively late. (Menke et al., 2003)

As the *Wt1<sup>het del</sup>* mice show a gradual development of FSGS, it serves as a reliable model to perform a time-course analysis of Wt1-dependent gene regulation in the course of disease.

In these mice, Wt1 commands podocytes to adopt a differential transcriptomic signature during FSGS progression. Differential binding analysis of the Wt1 ChIPseq peaks across the genome is suggestive of a general reprogramming phenomenon directed by Wt1. There is solid evidence in the literature on the modulation of epigenetic landscape by Wt1 in different cell types during disease progression. One of which is the study performed by Rampal and his colleagues where they show differential expression of Wt1 in acute myeloid leukemia (AML) leading to changes in 5-hydroxymethylcytosine (5hmC) levels and the subsequent gene expression modification. (Rampal et al., 2014)



Another interesting aspect of Wt1 activity is a phenomenon termed as “chromatin flipflop”. This term was first suggested by Essafi and his colleagues when they refer to the reciprocal function of Wt1 in the heart versus kidneys through regulation of Wnt4. Wt1 is responsible for mesenchymal to epithelial transition (MET) in the kidneys whereas it does the reverse job in the epicardium (EMT). In both tissues, Wt1 induces global changes in chromatin accessibility by switching the CTCF boundaries. (Essafi et al., 2011)

Taken together, these pieces of evidence substantiate our finding on the ability of Wt1 to modify the chromatin landscape and reprogram podocytes to adopt an alternative transcriptomic signature during the progression of glomerulosclerosis. However, the mechanism by which Wt1 induces changes in chromatin accessibility and gene expression during FSGS needs to be further investigated.

## **8.2 Collagen Biology is one of the main functional targets of Wt1 during the development of FSGS.**

In this thesis, an elaborate expression profile of all collagen types is provided for the first time in the course of podocyte disease. Thus far, majority of the existing studies have focused on array data from patient and or mice samples. (Hodgin et al., 2010; Ju et al., 2009) Here, the differential expression analysis of the RNAseq data shows a significant down regulation of Col IV a3,4 and 5 transcripts in late FSGS whereas Col IV a1 and 2 transcripts have upregulated both in early and late FSGS. Moreover, STED images of the GBM from *Wt1<sup>het del</sup>* mice highlights the disrupted collagen IV synthesis by appearance of collagen humps along the basement membrane.

Collagens, especially type IV, are the indispensable units for the strength and stability of the GBM. (Chew and Lennon, 2018; Pöschl et al., 2004) Col IV a1,a1,a2 is the predominant form in developing glomeruli whereas Col IV a3,a4,a5 is found in mature GBM . (Abrahamson et al., 2009) Evidence from the literature suggests that perturbations in the Col IV isoforms is linked to different kidney diseases in patients as well as mice. Handfuls of the existing publications have focused on *Col IV* mutations in Alport syndrome where mutations in *Col4A3*, *Col4A4*, and *Col4A5* lead to a deficiency in shifting from ColIVa1,a1,a2 to ColIVa3,a4,a5. (Lennon et al., 2014; Noone and Licht, 2013) Gast and his colleagues suggest that Col IV mutations are one of the underlying causes of hereditary FSGS. (Gast et al., 2016) In a pilot study of a family with a history of glomerular disease, Lennon and her colleagues have shown concomitant Col IV a5 and MYO1E mutations exacerbates the kidney damage. (Lennon et al., 2015) In addition, Col IVa3 and 4 transcripts are reduced in a mouse model of nephrotic syndrome as a result of conditional *Lmx1b* deletion. (Morello et al., 2001) In patients with minimal change disease (MCD), dissected glomeruli show increased Col IV a1,a1,a2 expression. (Hodgin et al., 2010) These studies support the observations made in *Wt1<sup>het del</sup>* mice. Conclusively, alterations in Col IV subtypes is one of the key events in during the podocyte injury.

In this thesis, differential expression of Col IV is shown on the protein level. However, the antibody which was used in staining does not differentiate between the Col IV isoforms. Therefore, it might be worth investigating how the dynamics of Col IV isoforms fluctuate in the course of disease using targeted mass spectrophotometry of whole glomeruli lysates.

### **8.3 Ephrin Signaling pathway is a novel target of Wt1 during podocyte damage.**

In this thesis, integrated ChIPseq and RNAseq analysis of *Wt1*<sup>het del</sup> mice are suggestive of a marked repression for the “Ephrin Signaling” pathway both on the gene and the transcript level. Moreover, several players of the Eph/Ephrin signaling pathway have shown a significant differential expression including EphrinB1 and EphB1 which have been downregulated both in early and late FSGS.

In podocytes, EphrinB1 and its receptor EphB1 have the highest expression compared to the other Ephrins and Ephs. (Karaiskos et al., 2018) Therefore, it is valid to speculate that majority of the “Ephrin Signaling” commands are initiated by these two proteins. Thus, further experiments were focused on EphrinB1 and EphB1. Targeted mass spectrophotometry shows a marked reduction of EphrinB1 in late FSGS. Furthermore, co-staining of the kidneys with Ephb1 and EphrinB1 in *Wt1*<sup>het del</sup> mice demonstrates an explicit reduction of their signal which is more pronounced at sclerotic stage (12-week<sup>het del</sup> mice) compared to healthy animals. Remarkably, the reduction in EphrinB1 signal intensity is highly correlated with the extent to which sclerosis is progressed. These findings are in line with the existing literature as in human patients with active nephrotic syndrome, a clear reduction in EphrinB1 signal is observed in immunofluorescent images. Moreover, conditional deletion of EphrinB1 in podocytes leads to the development of proteinuria and foot processes effacement in mice. (Fukusumi et al., 2018) EphrinB1 localizes at the slit diaphragm and contributes to the maintenance of the barrier function. (Hashimoto et al., 2007) Fukusumi and his colleagues maintain that when the podocytes are offended by a primary cause, EphrinB1 is phosphorylated and promotes cell motility via a JNK-dependent mechanism. They claim this chain of events mechanistically explains the process of podocyte detachment during injury (Fukusumi et al., 2018)

The initial cellular cascades triggered by Eph/Ephrin signaling converge on cytoskeletal targets such as integrins and actin cytoskeleton modulators mainly Rho GTPases. (Coulthard et al., 2012; Lisabeth et al., 2013) Both cytoskeletal targets dictate how podocytes tolerate intra and/or extracellular offenses by modulating the general shape of foot processes as well as attachment/detachment balance to the GBM. Therefore, an Eph/Ephrin-promoted actin (de)polymerization disbalance might be another possible explanation for podocyte detachment and loss during FSGS progression. However, further investigation needs to be conducted as to when and how the Eph/Ephrin signaling joins the stage in the course of glomerulosclerosis.

## 8.4 Tead1 exerts the Hippo pathway-mediated gene regulation in podocytes.

The tissue distribution of TEAD TFs varies from one organ to another. This thesis has addressed the podocyte specific expression of TEADs for the first time. Tead1, 4 and 3 are expressed in the kidneys and Tead1 is expressed significantly higher in podocytes. This novel piece of information is complementary to the existing knowledge on the expression dynamics of the TEAD TFs in different cell types in the body. At the 2-cell stage, Tead2 is predominant among other TEADs. (Kaneko et al., 1997) During development, Tead2 is specifically expressed in some embryonic tissues such as testis, forelimb and hindlimb buds, cerebellum and tail bud. (Yasunami et al., 1995) In contrast, Tead1, 3, and 4 are the widespread forms in tissues such as heart, pancreas, lung and skeletal muscle during adult life. (Azakie et al., 2005; Stewart et al., 1996; Yasunami et al., 1996) Since Tead1 is the predominant form of TEAD TFs in podocytes, it serves as the main downstream effector of the Hippo pathway.

Immunofluorescent staining of the Tead1 shows that it is mainly localized in the nucleus of normal healthy podocytes. Regulation of TEADs is mediated through different mechanisms and subcellular localization is one of the mechanisms by which TEADs molecular function is controlled. Hyperosmotic pressure and cell detachment lead to cytoplasmic localization of TEADs which is mediated via p38 mitogen-activated protein kinase (p38 MAPK) activity. (Lin et al., 2017) Cellular stress induces modifications in the subcellular localization of TEADs through P38 MAPK. This mentioned, it might be highly interesting to investigate the fluctuations of Tead1 subcellular localization during podocyte injury.

The nuclear localization of Tead1 in healthy podocytes suggests active gene regulation via Tead1. *De novo* motif enrichment analysis of the Tead1ChIPseq data from isolated mouse glomeruli identifies the consensus binding region of 5'-CATTCCA/T-3' for Tead1. In TEAD(s), TEA is the DNA binding domain (DBD) which binds to the same consensus sequence known as MCAT element. (Farrance et al., 1992) Moreover, Tead1 is functionally involved in pivotal cellular processes in podocyte biology. Functions include but not limited to cellular adhesion and actin-based cellular organization. Likewise, Tead1 functions in non-podocyte cells have been addressed in a handful of other studies where the actin cytoskeleton organization and focal adhesion have recurrently appeared. (Liu et al., 2017; Stein et al., 2015)

Majority of Tead-mediated functions are believed to be mediated via enhancers. (Davidson et al., 1988; Stein et al., 2015) In line with this, analysis of Tead1 binding across the genomic features shows that Tead1 predominantly binds to intergenic and intronic sites in podocytes. Altogether, Tead1 orchestrates its gene-regulatory functions by chiefly binding to putative enhancers in wildtype mouse glomeruli. The main cellular processes that are governed by Tead1 in podocytes involve cell adhesion and actin cytoskeleton dynamics.

One of the key findings of gene regulation in podocytes is the cooperation possibility between Tead1 and Wt1 on gene regulatory regions. (Kann et al., 2015) Strikingly, the co-binding

analysis of the Tead1 and Wt1 on gene regulatory elements revealed a functional alliance between these transcription factors for regulation of key podocyte functions such as actin cytoskeleton assembly and cell adhesion. More than 70% of the total co-binding occurs at distant regulatory regions which further substantiates the importance of enhancer-dependent functions in podocyte homeostasis. Of note, TEA domains require cooperative binding to regulatory elements, and they are believed to bind cooperatively to tandem repeats. (Davidson et al., 1988) This property perfectly matches with what is found in the co-binding analysis. Majority of Tead1 target genes are likely to be co-dependent on Tead1 as well as Wt1 binding. Further investigation is needed as to which DNA sequences call for Tead1 and Wt1 co-binding and which of such sequences code for key podocyte genes.

## **8.5 The puzzle of gene regulation in podocytes**

A very interesting breakthrough in the gene regulation arena is the higher resolution datasets gained from single-cell omics studies such as single cell RNA sequencing, single cell epigenomics, etc. Such studies have facilitated understanding of the crosstalk between different kidney cell types and the gene regulation by transcription factors and other epigenetic regulators. (Lambert et al., 2018; Park et al., 2019) In this thesis, a single-cell RNAseq atlas of the mouse glomeruli is introduced to the kidney research community. Besides, a free online webtool is provided which can be queried based on a single gene or a set of gene names. (<https://shiny.mdc-berlin.de/mgsca/>) For the first time, an exhaustive resource of gene expression for individual glomerular cell types is published. Off note, earlier attempts in this direction consisted of very few cells and their focus was directed to one certain cell type. For example, single cell RNA sequencing of 20 mouse podocytes showed that majority of essential podocyte genes are linked to cytoskeleton. (Lu et al., 2017) Our dataset, however, is gained from an unbiased highly parallel single-cell profiling of nearly 13,000 cells and thus the readout is more solid comparing to the previous studies.

One of the key findings in this thesis is the identification of several novel markers for podocytes, endothelial cells and mesangial cell which were not found to date. One advantage of single-cell RNA sequencing technology is its ability to identify novel markers. During “bulk RNA sequencing”, the lower abundance transcripts are often masked by the higher abundance transcripts and there is always a fair chance that they are not detected although they might bear very important biological impacts. (McCarthy et al., 2017) This limitation is surpassed in our dataset and the identified novel markers are validated using the immunohistochemistry images obtained from the Human Protein Atlas.

Another key merit of the single cell RNA sequencing technology is its ability to decipher cell-to-cell variability within a sample. In this regard, Der and colleagues have addressed cell heterogeneity of the kidney and skin specimens of patients suffering from lupus nephritis to identify novel diagnostic markers. This group claims that the assessment of kidney injury in lupus nephritis patient can be facilitated by the utilization of accessible skin tissue. (Der et al.,

2017) Here, our dataset is examined for potential cell heterogeneity among podocytes and endothelial cells. Individual cell subpopulations are identified in podocytes and endothelial cell clusters. The endothelial cell clusters reflect different stages of endothelial cell activation and proliferation. Furthermore, the podocyte subpopulations are validated by immunofluorescent staining of the relevant subtype markers. Perhaps, cellular diversity is one of the key possibilities as to why certain populations of podocytes and endothelial cells are more susceptible to damage in response to external and internal stimuli. However, it is not valid to extrapolate the findings of podocytes and endothelial cell subpopulations to all the mouse strains as well as human. The former, our dataset is comprised of a certain mouse strain, sex and age. The latter, although a great proportion of the identified cells have a glomerular origin, there is a chance that the identified endothelial cells have an extraglomerular source. Despite all the discussed caveats, the single-cell transcriptome atlas provided in this thesis can serve as a valuable resource for further studies in the same direction.

## **8.6 Concluding remarks**

Efficacious management of chronic kidney disease requires informed classification of the underlying etiology. Be it diabetes, virus-associated, malignancies or idiopathic, podocyte damage is the first cause of proteinuria and the drop in GFR.

In the context of hereditary FSGS, handfuls of genes have been reported as causal which contribute to the pathogenesis of podocyte injury. Master podocyte transcription factors as well as chromatin modifiers constitute a large proportion of the causal mutations for podocyte damage. Deciphering how the transcriptional regulation circuit works in podocytes paves the ground for introducing novel therapeutic routes during the initial phases of the podocyte damage.

In this thesis, we have focused on different and yet interesting aspects of transcriptional regulation in podocytes. The complementary characteristic of our results points out to certain features of gene regulation in healthy as well as injured podocytes.

One of the key strengths of this thesis is that the relevance of disease progression to the observed cellular phenotypes is discussed for the first time. The dependence of EphrinB1 reduction in the course of podocyte damage is a clear example of how time-course investigation into disease processes could offer new avenues in the management of disease phenotypes. Additionally, we have shown several functional perturbations in podocytes during the progression of FSGS one of which is the “Collagen Biology” which is extensively discussed. However, only one genetically modified mouse model has been employed in this thesis as the model for hereditary FSGS. Expectedly, other FSGS mouse models elicit several mutual cellular functions as well as some novel pathways contributing in different stages of the disease. It is intriguing to utilize the data obtained from different FSGS models as an input for a network-based analysis of key mechanisms underlying podocyte damage.

Another key finding in this thesis is the functional analysis of co-binding for two podocyte-specific master TFs, Wt1 and Tead1. A very tantalizing next step in this direction would be to investigate the co-binding in podocyte disease setting.

Last but not the least, we have employed the power of single-cell transcriptome profiling to introduce novel markers for podocytes, endothelial cells as well as mesangial cells. What is more, the possibility of cell heterogeneity is investigated for endothelial cells and podocytes. Future studies are needed to unravel whether our claimed subcellular populations are justified in other mouse strains as well as humans.

## 9 Bibliography

Abrahamson, D.R., Hudson, B.G., Stroganova, L., Borza, D.-B., and St John, P.L. (2009). Cellular origins of type IV collagen networks in developing glomeruli. *J. Am. Soc. Nephrol. JASN* 20, 1471–1479.

Andrews, P.M. (1981). Investigations of cytoplasmic contractile and cytoskeletal elements in the kidney glomerulus. *Kidney Int.* 20, 549–562.

Azakie, A., Lamont, L., Fineman, J.R., and He, Y. (2005). Divergent transcriptional enhancer factor-1 regulates the cardiac troponin T promoter. *Am. J. Physiol. Cell Physiol.* 289, C1522–1534.

Baird, P.N., Santos, A., Groves, N., Jadresic, L., and Cowell, J.K. (1992). Constitutional mutations in the WT1 gene in patients with Denys-Drash syndrome. *Hum. Mol. Genet.* 1, 301–305.

Bass, A.J., Watanabe, H., Mermel, C.H., Yu, S., Perner, S., Verhaak, R.G., Kim, S.Y., Wardwell, L., Tamayo, P., Gat-Viks, I., et al. (2009). SOX2 is an amplified lineage-survival oncogene in lung and esophageal squamous cell carcinomas. *Nat. Genet.* 41, 1238–1242.

Beck, L., Bomback, A.S., Choi, M.J., Holzman, L.B., Langford, C., Mariani, L.H., Somers, M.J., Trachtman, H., and Waldman, M. (2013). KDOQI US commentary on the 2012 KDIGO clinical practice guideline for glomerulonephritis. *Am. J. Kidney Dis. Off. J. Natl. Kidney Found.* 62, 403–441.

Boerries, M., Grahammer, F., Eiselein, S., Buck, M., Meyer, C., Goedel, M., Bechtel, W., Zschiedrich, S., Pfeifer, D., Laloë, D., et al. (2013). Molecular fingerprinting of the podocyte reveals novel gene and protein regulatory networks. *Kidney Int.* 83, 1052–1064.

Boyer, O., Woerner, S., Yang, F., Oakeley, E.J., Linghu, B., Gribouval, O., Tête, M.-J., Duca, J.S., Klickstein, L., Damask, A.J., et al. (2013). LMX1B mutations cause hereditary FSGS without extrarenal involvement. *J. Am. Soc. Nephrol. JASN* 24, 1216–1222.

Brinkkoetter, P.T., Ising, C., and Benzing, T. (2013). The role of the podocyte in albumin filtration. *Nat. Rev. Nephrol.* 9, 328–336.

Brunskill, E.W., Park, J.-S., Chung, E., Chen, F., Magella, B., and Potter, S.S. (2014). Single cell dissection of early kidney development: multilineage priming. *Dev. Camb. Engl.* 141, 3093–3101.

Call, K.M., Glaser, T., Ito, C.Y., Buckler, A.J., Pelletier, J., Haber, D.A., Rose, E.A., Kral, A., Yeger, H., and Lewis, W.H. (1990). Isolation and characterization of a zinc finger polypeptide gene at the human chromosome 11 Wilms' tumor locus. *Cell* 60, 509–520.

Chen, L., Lee, J.W., Chou, C.-L., Nair, A.V., Battistone, M.A., Păunescu, T.G., Merkulova, M., Breton, S., Verlander, J.W., Wall, S.M., et al. (2017). Transcriptomes of major renal collecting duct cell types in mouse identified by single-cell RNA-seq. *Proc. Natl. Acad. Sci. U. S. A.* 114, E9989–E9998.

- Chen, X., Zaro, J.L., and Shen, W.-C. (2013). Fusion protein linkers: property, design and functionality. *Adv. Drug Deliv. Rev.* *65*, 1357–1369.
- Cheong, H.I., Chae, J.H., Kim, J.S., Park, H.W., Ha, I.S., Hwang, Y.S., Lee, H.S., and Choi, Y. (1999). Hereditary glomerulopathy associated with a mitochondrial tRNA(Leu) gene mutation. *Pediatr. Nephrol. Berl. Ger.* *13*, 477–480.
- Chew, C., and Lennon, R. (2018). Basement Membrane Defects in Genetic Kidney Diseases. *Front. Pediatr.* *6*, 11.
- Coulthard, M.G., Morgan, M., Woodruff, T.M., Arumugam, T.V., Taylor, S.M., Carpenter, T.C., Lackmann, M., and Boyd, A.W. (2012). Eph/Ephrin signaling in injury and inflammation. *Am. J. Pathol.* *181*, 1493–1503.
- Davidson, I., Xiao, J.H., Rosales, R., Staub, A., and Chambon, P. (1988). The HeLa cell protein TEF-1 binds specifically and cooperatively to two SV40 enhancer motifs of unrelated sequence. *Cell* *54*, 931–942.
- Der, E., Ranabothu, S., Suryawanshi, H., Akat, K.M., Clancy, R., Morozov, P., Kustagi, M., Czuppa, M., Izmirly, P., Belmont, H.M., et al. (2017). Single cell RNA sequencing to dissect the molecular heterogeneity in lupus nephritis. *JCI Insight* *2*.
- Dreyer, S.D., Zhou, G., Baldini, A., Winterpacht, A., Zabel, B., Cole, W., Johnson, R.L., and Lee, B. (1998). Mutations in LMX1B cause abnormal skeletal patterning and renal dysplasia in nail patella syndrome. *Nat. Genet.* *19*, 47–50.
- Essafi, A., Webb, A., Berry, R.L., Slight, J., Burn, S.F., Spraggon, L., Velecela, V., Martinez-Estrada, O.M., Wiltshire, J.H., Roberts, S.G.E., et al. (2011). A wt1-controlled chromatin switching mechanism underpins tissue-specific wnt4 activation and repression. *Dev. Cell* *21*, 559–574.
- Farrance, I.K., Mar, J.H., and Ordahl, C.P. (1992). M-CAT binding factor is related to the SV40 enhancer binding factor, TEF-1. *J. Biol. Chem.* *267*, 17234–17240.
- Fogo, A.B. (2003). Animal models of FSGS: lessons for pathogenesis and treatment. *Semin. Nephrol.* *23*, 161–171.
- Fogo, A.B. (2015). Causes and pathogenesis of focal segmental glomerulosclerosis. *Nat. Rev. Nephrol.* *11*, 76–87.
- Fukasawa, H., Bornheimer, S., Kudlicka, K., and Farquhar, M.G. (2009). Slit Diaphragms Contain Tight Junction Proteins. *J. Am. Soc. Nephrol.* *20*, 1491–1503.
- Fukusumi, Y., Zhang, Y., Yamagishi, R., Oda, K., Watanabe, T., Matsui, K., and Kawachi, H. (2018). Nephtrin-Binding Ephrin-B1 at the Slit Diaphragm Controls Podocyte Function through the JNK Pathway. *J. Am. Soc. Nephrol. JASN* *29*, 1462–1474.



- Gaidatzis, D., Burger, L., Florescu, M., and Stadler, M.B. (2015). Analysis of intronic and exonic reads in RNA-seq data characterizes transcriptional and post-transcriptional regulation. *Nat. Biotechnol.* *33*, 722–729.
- Gast, C., Pengelly, R.J., Lyon, M., Bunyan, D.J., Seaby, E.G., Graham, N., Venkat-Raman, G., and Ennis, S. (2016). Collagen (COL4A) mutations are the most frequent mutations underlying adult focal segmental glomerulosclerosis. *Nephrol. Dial. Transplant. Off. Publ. Eur. Dial. Transpl. Assoc. - Eur. Ren. Assoc.* *31*, 961–970.
- Gebeshuber, C.A., Kornauth, C., Dong, L., Sierig, R., Seibler, J., Reiss, M., Tauber, S., Bilban, M., Wang, S., Kain, R., et al. (2013). Focal segmental glomerulosclerosis is induced by microRNA-193a and its downregulation of WT1. *Nat. Med.* *19*, 481–487.
- Gessler, M., Poustka, A., Cavenee, W., Neve, R.L., Orkin, S.H., and Bruns, G.A. (1990). Homozygous deletion in Wilms tumours of a zinc-finger gene identified by chromosome jumping. *Nature* *343*, 774–778.
- Gibault, F., Sturbaut, M., Bailly, F., Melnyk, P., and Cotellet, P. (2018). Targeting Transcriptional Enhanced Associate Domains (TEADs). *J. Med. Chem.* *61*, 5057–5072.
- Giles, R.H., Ajzenberg, H., and Jackson, P.K. (2014). 3D spheroid model of mIMCD3 cells for studying ciliopathies and renal epithelial disorders. *Nat. Protoc.* *9*, 2725–2731.
- Graf, T., and Enver, T. (2009). Forcing cells to change lineages. *Nature* *462*, 587–594.
- Guo, J.-K., Menke, A.L., Gubler, M.-C., Clarke, A.R., Harrison, D., Hammes, A., Hastie, N.D., and Schedl, A. (2002). WT1 is a key regulator of podocyte function: reduced expression levels cause crescentic glomerulonephritis and mesangial sclerosis. *Hum. Mol. Genet.* *11*, 651–659.
- Haraldsson, B., Nyström, J., and Deen, W.M. (2008). Properties of the glomerular barrier and mechanisms of proteinuria. *Physiol. Rev.* *88*, 451–487.
- Hashimoto, T., Karasawa, T., Saito, A., Miyauchi, N., Han, G.D., Hayasaka, K., Shimizu, F., and Kawachi, H. (2007). Ephrin-B1 localizes at the slit diaphragm of the glomerular podocyte. *Kidney Int.* *72*, 954–964.
- Hastie, N.D. (2017). Wilms' tumour 1 (WT1) in development, homeostasis and disease. *Dev. Camb. Engl.* *144*, 2862–2872.
- Hill, N.R., Fatoba, S.T., Oke, J.L., Hirst, J.A., O'Callaghan, C.A., Lasserson, D.S., and Hobbs, F.D.R. (2016). Global Prevalence of Chronic Kidney Disease - A Systematic Review and Meta-Analysis. *PLoS One* *11*, e0158765.
- Hishikawa, A., Hayashi, K., and Itoh, H. (2018). Transcription Factors as Therapeutic Targets in Chronic Kidney Disease. *Mol. J. Synth. Chem. Nat. Prod. Chem.* *23*.
- Hodgin, J.B., Borczuk, A.C., Nasr, S.H., Markowitz, G.S., Nair, V., Martini, S., Eichinger, F., Vining, C., Berthier, C.C., Kretzler, M., et al. (2010). A Molecular Profile of Focal Segmental

Glomerulosclerosis from Formalin-Fixed, Paraffin-Embedded Tissue. *Am. J. Pathol.* *177*, 1674–1686.

Iijima, K., Someya, T., Ito, S., Nozu, K., Nakanishi, K., Matsuoka, K., Ohashi, H., Nagata, M., Kamei, K., and Sasaki, S. (2012). Focal segmental glomerulosclerosis in patients with complete deletion of one WT1 allele. *Pediatrics* *129*, e1621-1625.

Jansen, J.J., Maassen, J.A., van der Woude, F.J., Lemmink, H.A., van den Ouweland, J.M., t' Hart, L.M., Smeets, H.J., Bruijn, J.A., and Lemkes, H.H. (1997). Mutation in mitochondrial tRNA(Leu(UUR)) gene associated with progressive kidney disease. *J. Am. Soc. Nephrol. JASN* *8*, 1118–1124.

Jess, D.U. (2019). High-resolution Imaging of Cleared and Expanded Kidney Tissue Samples.

Jiang, S., and Mortazavi, A. (2018). Integrating ChIP-seq with other functional genomics data. *Brief. Funct. Genomics* *17*, 104–115.

Jiang, L., Hindmarch, C.C.T., Rogers, M., Campbell, C., Waterfall, C., Coghill, J., Mathieson, P.W., and Welsh, G.I. (2016). RNA sequencing analysis of human podocytes reveals glucocorticoid regulated gene networks targeting non-immune pathways. *Sci. Rep.* *6*, 35671.

Ju, W., Eichinger, F., Bitzer, M., Oh, J., McWeeney, S., Berthier, C.C., Shedden, K., Cohen, C.D., Henger, A., Krick, S., et al. (2009). Renal Gene and Protein Expression Signatures for Prediction of Kidney Disease Progression. *Am. J. Pathol.* *174*, 2073–2085.

Kaneko, K.J., Cullinan, E.B., Latham, K.E., and DePamphilis, M.L. (1997). Transcription factor mTEAD-2 is selectively expressed at the beginning of zygotic gene expression in the mouse. *Dev. Camb. Engl.* *124*, 1963–1973.

Kann, M., Ettou, S., Jung, Y.L., Lenz, M.O., Taglienti, M.E., Park, P.J., Schermer, B., Benzing, T., and Kreidberg, J.A. (2015). Genome-Wide Analysis of Wilms' Tumor 1-Controlled Gene Expression in Podocytes Reveals Key Regulatory Mechanisms. *J. Am. Soc. Nephrol. JASN* *26*, 2097–2104.

Karaiskos, N., Wahle, P., Alles, J., Boltengagen, A., Ayoub, S., Kipar, C., Kocks, C., Rajewsky, N., and Zinzen, R.P. (2017). The *Drosophila* embryo at single-cell transcriptome resolution. *Science* *358*, 194–199.

Karaiskos, N., Rahmatollahi, M., Boltengagen, A., Liu, H., Hoehne, M., Rinschen, M., Schermer, B., Benzing, T., Rajewsky, N., Kocks, C., et al. (2018). A Single-Cell Transcriptome Atlas of the Mouse Glomerulus. *J. Am. Soc. Nephrol. JASN* *29*, 2060–2068.

Kato, M., Hata, N., Banerjee, N., Futcher, B., and Zhang, M.Q. (2004). Identifying combinatorial regulation of transcription factors and binding motifs. *Genome Biol.* *5*, R56.

Klamt, B., Koziell, A., Poulat, F., Wieacker, P., Scambler, P., Berta, P., and Gessler, M. (1998). Frasier syndrome is caused by defective alternative splicing of WT1 leading to an altered ratio of WT1 +/-KTS splice isoforms. *Hum. Mol. Genet.* *7*, 709–714.

- Kreidberg, J.A., Sariola, H., Loring, J.M., Maeda, M., Pelletier, J., Housman, D., and Jaenisch, R. (1993). WT-1 is required for early kidney development. *Cell* 74, 679–691.
- Kundaje, A., Meuleman, W., Ernst, J., Bilenky, M., Yen, A., Kheradpour, P., Zhang, Z., Heravi-Moussavi, A., Liu, Y., Amin, V., et al. (2015). Integrative analysis of 111 reference human epigenomes. *Nature* 518, 317–330.
- Lafayette, R.A. (2019). Increasing Options for First-Line Therapy in Primary FSGS? *Kidney Int. Rep.* 4, 8–10.
- Lambert, S.A., Jolma, A., Campitelli, L.F., Das, P.K., Yin, Y., Albu, M., Chen, X., Taipale, J., Hughes, T.R., and Weirauch, M.T. (2018). The Human Transcription Factors. *Cell* 172, 650–665.
- Landt, S.G., Marinov, G.K., Kundaje, A., Kheradpour, P., Pauli, F., Batzoglou, S., Bernstein, B.E., Bickel, P., Brown, J.B., Cayting, P., et al. (2012). ChIP-seq guidelines and practices of the ENCODE and modENCODE consortia. *Genome Res.* 22, 1813–1831.
- Lennon, R., Randles, M.J., and Humphries, M.J. (2014). The importance of podocyte adhesion for a healthy glomerulus. *Front. Endocrinol.* 5, 160.
- Lennon, R., Stuart, H.M., Bierzynska, A., Randles, M.J., Kerr, B., Hillman, K.A., Batra, G., Campbell, J., Storey, H., Flinter, F.A., et al. (2015). Coinheritance of COL4A5 and MYO1E mutations accentuate the severity of kidney disease. *Pediatr. Nephrol. Berl. Ger.* 30, 1459–1465.
- Levin, A., Tonelli, M., Bonventre, J., Coresh, J., Donner, J.-A., Fogo, A.B., Fox, C.S., Gansevoort, R.T., Heerspink, H.J.L., Jardine, M., et al. (2017). Global kidney health 2017 and beyond: a roadmap for closing gaps in care, research, and policy. *Lancet Lond. Engl.* 390, 1888–1917.
- Lin, K.C., Park, H.W., and Guan, K.-L. (2017). Regulation of the Hippo pathway transcription factor TEAD. *Trends Biochem. Sci.* 42, 862–872.
- Lisabeth, E.M., Falivelli, G., and Pasquale, E.B. (2013). Eph Receptor Signaling and Ephrins. *Cold Spring Harb. Perspect. Biol.* 5.
- Liu, R., Lee, J., Kim, B.S., Wang, Q., Buxton, S.K., Balasubramanyam, N., Kim, J.J., Dong, J., Zhang, A., Li, S., et al. (2017). Tead1 is required for maintaining adult cardiomyocyte function, and its loss results in lethal dilated cardiomyopathy. *JCI Insight* 2.
- Lu, Y., Ye, Y., Bao, W., Yang, Q., Wang, J., Liu, Z., and Shi, S. (2017). Genome-wide identification of genes essential for podocyte cytoskeletons based on single-cell RNA sequencing. *Kidney Int.* 92, 1119–1129.
- Ma, S., Meng, Z., Chen, R., and Guan, K.-L. (2019). The Hippo Pathway: Biology and Pathophysiology. *Annu. Rev. Biochem.* 88, 577–604.
- Macosko, E.Z., Basu, A., Satija, R., Nemes, J., Shekhar, K., Goldman, M., Tirosh, I., Bialas, A.R., Kamitaki, N., Martersteck, E.M., et al. (2015). Highly parallel genome-wide expression profiling of individual cells using nanoliter droplets. *Cell* 161, 1202–1214.

- Magico, A.C., and Bell, J.B. (2011). Identification of a classical bipartite nuclear localization signal in the *Drosophila* TEA/ATTS protein scalloped. *PLoS One* 6, e21431.
- Marcotte, E.M., Pellegrini, M., Ng, H.L., Rice, D.W., Yeates, T.O., and Eisenberg, D. (1999). Detecting protein function and protein-protein interactions from genome sequences. *Science* 285, 751–753.
- Mason, R.J., and Vondriska, T.M. (2019). Chromatin Is the Same in a Relative Way (But You're Older). *Circ. Res.* 125, 209–211.
- Mathelier, A., Shi, W., and Wasserman, W.W. (2015). Identification of altered cis-regulatory elements in human disease. *Trends Genet. TIG* 31, 67–76.
- Mathieson, P.W. (2010). Podocyte actin in health, disease and treatment. *Nephrol. Dial. Transplant. Off. Publ. Eur. Dial. Transpl. Assoc. - Eur. Ren. Assoc.* 25, 1772–1773.
- McCarthy, D.J., Campbell, K.R., Lun, A.T.L., and Wills, Q.F. (2017). Scater: pre-processing, quality control, normalization and visualization of single-cell RNA-seq data in R. *Bioinforma. Oxf. Engl.* 33, 1179–1186.
- Menke, A.L., Ijpenberg, A., Fleming, S., Ross, A., Medine, C.N., Patek, C.E., Spraggon, L., Hughes, J., Clarke, A.R., and Hastie, N.D. (2003). The wt1-heterozygous mouse; a model to study the development of glomerular sclerosis. *J. Pathol.* 200, 667–674.
- Morello, R., Zhou, G., Dreyer, S.D., Harvey, S.J., Ninomiya, Y., Thorner, P.S., Miner, J.H., Cole, W., Winterpacht, A., Zabel, B., et al. (2001). Regulation of glomerular basement membrane collagen expression by LMX1B contributes to renal disease in nail patella syndrome. *Nat. Genet.* 27, 205–208.
- Morrison, A.A., Viney, R.L., Saleem, M.A., and Lodomery, M.R. (2008). New insights into the function of the Wilms tumor suppressor gene WT1 in podocytes. *Am. J. Physiol. Renal Physiol.* 295, F12-17.
- Mueller, R.F. (1994). The Denys-Drash syndrome. *J. Med. Genet.* 31, 471–477.
- Müller, R.-U., and Schermer, B. (2019). Hippo signaling—a central player in cystic kidney disease? *Pediatr. Nephrol. Berl. Ger.*
- Mundel, P., and Kriz, W. (1995). Structure and function of podocytes: an update. *Anat. Embryol. (Berl.)* 192, 385–397.
- Noone, D., and Licht, C. (2013). An update on the pathomechanisms and future therapies of Alport syndrome. *Pediatr. Nephrol. Berl. Ger.* 28, 1025–1036.
- Park, J., Shrestha, R., Qiu, C., Kondo, A., Huang, S., Werth, M., Li, M., Barasch, J., and Suszták, K. (2018). Single-cell transcriptomics of the mouse kidney reveals potential cellular targets of kidney disease. *Science* 360, 758–763.

- Park, J., Liu, C.L., Kim, J., and Susztak, K. (2019). Understanding the kidney one cell at a time. *Kidney Int.* *96*, 862–870.
- Pavenstädt, H., Kriz, W., and Kretzler, M. (2003). Cell biology of the glomerular podocyte. *Physiol. Rev.* *83*, 253–307.
- Peev, V., Hahm, E., and Reiser, J. (2017). Unwinding focal segmental glomerulosclerosis. *F1000Research* *6*, 466.
- Pelletier, J., Bruening, W., Li, F.P., Haber, D.A., Glaser, T., and Housman, D.E. (1991). WT1 mutations contribute to abnormal genital system development and hereditary Wilms' tumour. *Nature* *353*, 431–434.
- Perico, L., Conti, S., Benigni, A., and Remuzzi, G. (2016). Podocyte-actin dynamics in health and disease. *Nat. Rev. Nephrol.* *12*, 692–710.
- Pöschl, E., Schlötzer-Schrehardt, U., Brachvogel, B., Saito, K., Ninomiya, Y., and Mayer, U. (2004). Collagen IV is essential for basement membrane stability but dispensable for initiation of its assembly during early development. *Dev. Camb. Engl.* *131*, 1619–1628.
- Rampal, R., Alkalin, A., Madzo, J., Vasanthakumar, A., Pronier, E., Patel, J., Li, Y., Ahn, J., Abdel-Wahab, O., Shih, A., et al. (2014). DNA hydroxymethylation profiling reveals that WT1 mutations result in loss of TET2 function in acute myeloid leukemia. *Cell Rep.* *9*, 1841–1855.
- Ran, F.A., Hsu, P.D., Wright, J., Agarwala, V., Scott, D.A., and Zhang, F. (2013). Genome engineering using the CRISPR-Cas9 system. *Nat. Protoc.* *8*, 2281–2308.
- Reiser, J., Kriz, W., Kretzler, M., and Mundel, P. (2000). The glomerular slit diaphragm is a modified adherens junction. *J. Am. Soc. Nephrol. JASN* *11*, 1–8.
- Richardson, C.D., Ray, G.J., DeWitt, M.A., Curie, G.L., and Corn, J.E. (2016). Enhancing homology-directed genome editing by catalytically active and inactive CRISPR-Cas9 using asymmetric donor DNA. *Nat. Biotechnol.* *34*, 339–344.
- Rinschen, M.M., Grahammer, F., Hoppe, A.-K., Kohli, P., Hagmann, H., Kretz, O., Bertsch, S., Höhne, M., Göbel, H., Bartram, M.P., et al. (2017). YAP-mediated mechanotransduction determines the podocyte's response to damage. *Sci. Signal.* *10*.
- Rosenberg, A.Z., and Kopp, J.B. (2017). Focal Segmental Glomerulosclerosis. *Clin. J. Am. Soc. Nephrol. CJASN* *12*, 502–517.
- Ruf, R.G., Schultheiss, M., Lichtenberger, A., Karle, S.M., Zalewski, I., Mucha, B., Everding, A.S., Neuhaus, T., Patzer, L., Plank, C., et al. (2004). Prevalence of WT1 mutations in a large cohort of patients with steroid-resistant and steroid-sensitive nephrotic syndrome. *Kidney Int.* *66*, 564–570.
- Salari, K., Spulak, M.E., Cuff, J., Forster, A.D., Giacomini, C.P., Huang, S., Ko, M.E., Lin, A.Y., van de Rijn, M., and Pollack, J.R. (2012). CDX2 is an amplified lineage-survival oncogene in colorectal cancer. *Proc. Natl. Acad. Sci. U. S. A.* *109*, E3196-3205.

- Schumacher, V.A., Schlötzer-Schrehardt, U., Karumanchi, S.A., Shi, X., Zaia, J., Jeruschke, S., Zhang, D., Pavenstädt, H., Pavenstaedt, H., Drenckhan, A., et al. (2011). WT1-dependent sulfatase expression maintains the normal glomerular filtration barrier. *J. Am. Soc. Nephrol.* *JASN* *22*, 1286–1296.
- Sever, S., and Schiffer, M. (2018). Actin dynamics at focal adhesions: a common endpoint and putative therapeutic target for proteinuric kidney diseases. *Kidney Int.* *93*, 1298–1307.
- Shema, E., Bernstein, B.E., and Buenrostro, J.D. (2019). Single-cell and single-molecule epigenomics to uncover genome regulation at unprecedented resolution. *Nat. Genet.* *51*, 19–25.
- Śnit, M., Nabrdalik, K., Długaszek, M., Gumprecht, J., Trautsolt, W., Górczyńska-Kosiorz, S., and Grzeszczak, W. (2017). Association of rs 3807337 polymorphism of CALD1 gene with diabetic nephropathy occurrence in type 1 diabetes - preliminary results of a family-based study. *Endokrynol. Pol.* *68*, 13–17.
- Soufi, A., Garcia, M.F., Jaroszewicz, A., Osman, N., Pellegrini, M., and Zaret, K.S. (2015). Pioneer transcription factors target partial DNA motifs on nucleosomes to initiate reprogramming. *Cell* *161*, 555–568.
- Stein, C., Bardet, A.F., Roma, G., Bergling, S., Clay, I., Ruchti, A., Agarinis, C., Schmelzle, T., Bouwmeester, T., Schübeler, D., et al. (2015). YAP1 Exerts Its Transcriptional Control via TEAD-Mediated Activation of Enhancers. *PLoS Genet.* *11*, e1005465.
- Stewart, A.F., Richard, C.W., Suzow, J., Stephan, D., Weremowicz, S., Morton, C.C., and Adra, C.N. (1996). Cloning of human RTEF-1, a transcriptional enhancer factor-1-related gene preferentially expressed in skeletal muscle: evidence for an ancient multigene family. *Genomics* *37*, 68–76.
- Svensson, V., Vento-Tormo, R., and Teichmann, S.A. (2018). Exponential scaling of single-cell RNA-seq in the past decade. *Nat. Protoc.* *13*, 599–604.
- Taketo, M., Schroeder, A.C., Mobraaten, L.E., Gunning, K.B., Hanten, G., Fox, R.R., Roderick, T.H., Stewart, C.L., Lilly, F., and Hansen, C.T. (1991). FVB/N: an inbred mouse strain preferable for transgenic analyses. *Proc. Natl. Acad. Sci. U. S. A.* *88*, 2065–2069.
- Tang, F., Barbacioru, C., Wang, Y., Nordman, E., Lee, C., Xu, N., Wang, X., Bodeau, J., Tuch, B.B., Siddiqui, A., et al. (2009). mRNA-Seq whole-transcriptome analysis of a single cell. *Nat. Methods* *6*, 377–382.
- Tarca, A.L., Draghici, S., Khatri, P., Hassan, S.S., Mittal, P., Kim, J., Kim, C.J., Kusanovic, J.P., and Romero, R. (2009). A novel signaling pathway impact analysis. *Bioinformatics* *25*, 75–82.
- Tome-Garcia, J., Erfani, P., Nudelman, G., Tsankov, A.M., Katsyv, I., Tejero, R., Bin Zhang, null, Walsh, M., Friedel, R.H., Zaslavsky, E., et al. (2018). Analysis of chromatin accessibility uncovers TEAD1 as a regulator of migration in human glioblastoma. *Nat. Commun.* *9*, 4020.

- Totaro, A., Panciera, T., and Piccolo, S. (2018). YAP/TAZ upstream signals and downstream responses. *Nat. Cell Biol.* *20*, 888–899.
- Totaro, A., Zhuang, Q., Panciera, T., Battilana, G., Azzolin, L., Brumana, G., Gandin, A., Brusatin, G., Cordenonsi, M., and Piccolo, S. (2019). Cell phenotypic plasticity requires autophagic flux driven by YAP/TAZ mechanotransduction. *Proc. Natl. Acad. Sci. U. S. A.* *116*, 17848–17857.
- Tröder, S.E., Ebert, L.K., Butt, L., Assenmacher, S., Schermer, B., and Zevnik, B. (2018). An optimized electroporation approach for efficient CRISPR/Cas9 genome editing in murine zygotes. *PLoS ONE* *13*.
- Truett, G.E., Heeger, P., Mynatt, R.L., Truett, A.A., Walker, J.A., and Warman, M.L. (2000). Preparation of PCR-quality mouse genomic DNA with hot sodium hydroxide and tris (HotSHOT). *BioTechniques* *29*, 52, 54.
- Tsankov, A.M., Brown, C.R., Yu, M.C., Win, M.Z., Silver, P.A., and Casolari, J.M. (2006). Communication between levels of transcriptional control improves robustness and adaptivity. *Mol. Syst. Biol.* *2*, 65.
- Ullmark, T., Montano, G., and Gullberg, U. (2018). DNA and RNA binding by the Wilms' tumour gene 1 (WT1) protein +KTS and -KTS isoforms-From initial observations to recent global genomic analyses. *Eur. J. Haematol.* *100*, 229–240.
- Unnersjö-Jess, D., Scott, L., Sevilla, S.Z., Patrakka, J., Blom, H., and Brismar, H. (2018). Confocal super-resolution imaging of the glomerular filtration barrier enabled by tissue expansion. *Kidney Int.* *93*, 1008–1013.
- Wang, M., Chun, J., Genovese, G., Knob, A.U., Benjamin, A., Wilkins, M.S., Friedman, D.J., Appel, G.B., Lifton, R.P., Mane, S., et al. (2019). Contributions of Rare Gene Variants to Familial and Sporadic FSGS. *J. Am. Soc. Nephrol. JASN* *30*, 1625–1640.
- Wang, Z., Wang, Z., Zhou, Z., and Ren, Y. (2016). Crucial genes associated with diabetic nephropathy explored by microarray analysis. *BMC Nephrol.* *17*, 128.
- Weiss, A.-C., and Kispert, A. (2016). Eph/ephrin signaling in the kidney and lower urinary tract. *Pediatr. Nephrol. Berl. Ger.* *31*, 359–371.
- Wiggins, R.C. (2007). The spectrum of podocytopathies: a unifying view of glomerular diseases. *Kidney Int.* *71*, 1205–1214.
- Wittkopp, P.J., and Kalay, G. (2011). Cis-regulatory elements: molecular mechanisms and evolutionary processes underlying divergence. *Nat. Rev. Genet.* *13*, 59–69.
- Wong, J.S., Meliambro, K., Ray, J., and Campbell, K.N. (2016). Hippo signaling in the kidney: the good and the bad. *Am. J. Physiol. - Ren. Physiol.* *311*, F241–F248.
- Wyvekens, N., Tsai, S.Q., and Joung, J.K. (2015). Genome Editing in Human Cells Using CRISPR/Cas Nucleases. *Curr. Protoc. Mol. Biol.* *112*, 31.3.1-18.

Yasunami, M., Suzuki, K., Houtani, T., Sugimoto, T., and Ohkubo, H. (1995). Molecular characterization of cDNA encoding a novel protein related to transcriptional enhancer factor-1 from neural precursor cells. *J. Biol. Chem.* 270, 18649–18654.

Yasunami, M., Suzuki, K., and Ohkubo, H. (1996). A novel family of TEA domain-containing transcription factors with distinct spatiotemporal expression patterns. *Biochem. Biophys. Res. Commun.* 228, 365–370.

Yu, S.M.-W., Nissaisorakarn, P., Husain, I., and Jim, B. (2018). Proteinuric Kidney Diseases: A Podocyte's Slit Diaphragm and Cytoskeleton Approach. *Front. Med.* 5, 221.

Zhou, H., Cheruvanky, A., Hu, X., Matsumoto, T., Hiramatsu, N., Cho, M.E., Berger, A., Leelahavanichkul, A., Doi, K., Chawla, L.S., et al. (2008). Urinary exosomal transcription factors, a new class of biomarkers for renal disease. *Kidney Int.* 74, 613–621.



## 10 Publications

### 10.1 Publication in academic journals

- 1- Karaiskos, N., Rahmatollahi, M., Boltengagen, A., Liu, H., Hoehne, M., Rinschen, M., Schermer, B., Benzing, T., Rajewsky, N., Kocks, C., et al. (2018). A Single-Cell Transcriptome Atlas of the Mouse Glomerulus. *J. Am. Soc. Nephrol. JASN* 29, 2060–2068.
- 2- Höhne, M., Frese, C.K., Grahammer, F., Dafinger, C., Ciarimboli, G., Butt, L., Binz, J., Hackl, M.J., Rahmatollahi, M., Kann, M., et al. (2018). Single-nephron proteomes connect morphology and function in proteinuric kidney disease. *Kidney Int.* 93, 1308–1319.

### 10.2 Publication in international academic conferences

- 1- Rahmatollahi, M., Padvitski, T., Schermer, B., Benzig, T., Beyer, A., Kann, M. (2018). The Hippo Effector Tead1 Interacts with Wt1 on a Gene-regulatory Level by Co-binding at Putative Podocyte Enhancers. American Society of Nephrology (*poster presentation*)
- 2- Karaiskos, N., Rahmatollahi, M., Boltengagen, A., Liu, H., Hoehne, M., Rinschen, M., Schermer, B., Benzing, T., Rajewsky, N., Kocks, C., et al. (2018). Single-cell Transcriptomics of Wildtype Mouse Glomeruli. Deutsche Gesellschaft für Nephrologie. (*poster presentation*)
- 3- Karaiskos, N., Rahmatollahi, M., Boltengagen, A., Liu, H., Hoehne, M., Rinschen, M., Schermer, B., Benzing, T., Rajewsky, N., Kocks, C., et al. (2018). Single-cell Transcriptomics of Wildtype Mouse Glomeruli. Podocyte Conference (*poster presentation*)
- 4- Rahmatollahi, M., Kann, M., Lenz, M., Schermer, B., Benzig, T. (2016). Gene regulatory reprogramming by WT1 in murine podocytes affected by hereditary FSGS. American Society of Nephrology (*poster presentation*)
- 5- Rahmatollahi, M., Kann, M., Lenz, M., Schermer, B., Benzig, T. (2016). Transkriptionelle Reprogrammierung durch WT1 in einem genetischen FSGS-Modell. Deutsche Gesellschaft für Nephrologie. (*oral presentation held by Kann M.*)

## 11 Acknowledgment

I have learned invaluable lessons during my PhD journey that for sure will be fairly employed throughout my life. I need to thank a lot of people; each helped me to complete my mission in these years. First, I am deeply thankful to Professor Thomas Benzing and Professor Bernhard Schermer who gave me the chance to do my PhD thesis in their lab. In addition, I am thankful to Professor Andreas Beyer and his constructive inputs during my PhD. I am also thankful to Dr. Martin Kann who taught me the ropes of chromatin biology. Without our fruitful discussions, I could not accomplish this much for sure.

I should also thank my dear colleagues in Nephrolab, all of them facilitated my growing process through these years. I am especially thankful to Dr. Claudia Dafinger for her thorough support in my mouse experiments. I am deeply thankful to Dr. Martin Hoehne for his support and his brilliant solutions in image processing. Every lab should be proud to have you Martin! I am also thankful to Dr. Linus Butt and Dr. David Unnersjö Jess for their extraordinary cooperation and support in the IF staining of GBM components. I am thankful to Lena for her support in my CRISPR/Cas9 experiments. In addition, I am truly thankful to Ms. Stefanie Keller, Ms. Martyna Bruetting, Ms. Ruth Herzog and Ms. Serena Torres for their support and help in some of my experiments. Besides the Nephrolab, I am thankful to Dr. Christian Cocks and Dr. Nikolaus Karaiskos for our great collaboration during the single cell RNAseq project. Finally, I am deeply thankful to Dr. Juergen Klar and his team for a great internship experience in kidney research industry. I should also thank Dr. Marion Rozowski and her diligent support in our graduate program.

I owe a debt of gratitude to a number of people whose scientific and mental support was just priceless for me. Mahsa and Gisela! We had fun together, we supported each other, and we learned together. Is the meaning of life other than this?

Angela and Matthias! I would not grow as much as I did if I had not known you! Thank you for being there for me!

Akos! Thanks a lot for the coffee breaks and the loud brainstorming moments!

Christian! I cannot thank you enough for the things I have learned from you. Everyone should wish to have a colleague like you!

Tim! You were my younger bro through these years! Our teamwork makes me proud cause it is a vivid example of how two different minds can fulfill a project!

There are 6 people without whom my life would be just meaningless! Not only I am thankful for their support during my PhD, but also, I'm blessed because I have known them in this universe! Mom and Dad! What I am today is just because I was loved by you. Nothing compares to your love for me. I am so blessed that I was raised by you!

Hamed! I'm filled with joy with your growth and success. Keep it up and thanks for stepping into our world!

Sami! My alter ego! And Reza! My second octopus! Life would be bitter if I had not found you!

The last but not the least: Amin! I am so proud to have you in my life. My life is filled with joy and motivation to grow, and the reason is you! I cannot thank the universe enough for it gifted you to me. We were so meant to be together my soulmate! I love you!

## 12 Erklärung

Ich versichere, dass ich die von mir vorgelegte Dissertation selbständig angefertigt, die benutzten Quellen und Hilfsmittel vollständig angegeben und die Stellen der Arbeit – einschließlich Tabellen, Karten und Abbildungen –, die anderen Werken im Wortlaut oder dem Sinn nach entnommen sind, in jedem Einzelfall als Entlehnung kenntlich gemacht habe; dass diese Dissertation noch keiner anderen Fakultät oder Universität zur Prüfung vorgelegen hat; dass sie – abgesehen von unten angegebenen Teilpublikationen – noch nicht veröffentlicht worden ist, sowie, dass ich eine solche Veröffentlichung vor Abschluss des Promotionsverfahrens nicht vornehmen werde. Die Bestimmungen der Promotionsordnung sind mir bekannt. Die von mir vorgelegte Dissertation ist von Prof. Andreas Beyer und Prof. Thomas Benzing betreut worden.

### Teilpublikationen:

- 1- Karaiskos, N.\*, Rahmatollahi, M.\*, Boltengagen, A., Liu, H., Hoehne, M., Rinschen, M., Schermer, B., Benzing, T., Rajewsky, N., Kocks, C., et al. (2018). A Single-Cell Transcriptome Atlas of the Mouse Glomerulus. *J. Am. Soc. Nephrol. JASN* 29, 2060–2068. *Shared first authorship*
- 2- Höhne, M., Frese, C.K., Grahammer, F., Dafinger, C., Ciarimboli, G., Butt, L., Binz, J., Hackl, M.J., Rahmatollahi, M., Kann, M., et al. (2018). Single-nephron proteomes connect morphology and function in proteinuric kidney disease. *Kidney Int.* 93, 1308–1319.

Köln, 15.01.2020

-----  
Ort, Datum



-----  
Mahdieh Rahmatollahi

## 13 Curriculum Vitae

### PERSÖNLICHE DATEN

---

Nachname:: Rahmatollahi  
Vorname: Mahdih  
Geburtsdatum: 27.07.1985  
Geburtsort: Teheran, Iran  
Nationalität: Persisch  
E-mail: mahdih.rahmatollahi@yahoo.com

### AKADEMISCHE AUSBILDUNG

---

Juli 2015 – März 2020

**Promotion in Genomics**

Innere Medizin II - Nephrologie, Rheumatologie, Diabetologie und Allgemeine Innere Medizin, Köln, Deutschland

Thema: *Transcriptional Regulation in Podocytes*

Betreuer: Prof. B. Schermer, Prof. A. Beyer

Oktober 2008 – Februar 2012

**M.Sc. in General Toxicology**

Pharmacologie und experimentelle Medizin  
Tehran University of Medical Sciences, Teheran, Iran

Thema: *PPAR- $\alpha$  receptor; potential targets against Doxorubicin-induced cardiotoxicity.*

Betreuer: Prof. A. Dehpour, Dr. A. Mani

Oktober 2003 – Juni 2008

**B.Sc. in Animal Biology**

Fakultät für Naturwissenschaften und Mathematik,  
University of Teheran, Teheran, Iran

### SCHULISCHE AUSBILDUNG

---

Oktober 2002 – Juni 2003

**Pre-university studies in Experimental Sciences**

Hejab Pre-university Center, Teheran, Iran

Oktober 1999 – Juni 2002

**Highschool studies in Experimental Sciences**

Mehrnam Highschool, Teheran, Iran

